

Peter Manser

Verification of Intensity Modulated
Radiotherapy with an Amorphous
Silicon Portal Imaging Device

Diss ETH No. 15334

Diss. ETH No. 15334

Verification of Intensity Modulated Radiotherapy with an Amorphous Silicon Portal Imaging Device

A thesis submitted to the

SWISS FEDERAL INSTITUTE OF TECHNOLOGY ZURICH

for the degree of

Doctor of the Natural Sciences

Presented by

Peter Manser

Dipl. Phys. ETH

Born on September 28, 1971

Citizen of Appenzell, Switzerland

Accepted on the recommendation of

Prof. Dr. Peter Niederer, examiner

Prof. Dr. Peter Rügsegger, co-examiner

Dr. Roberto Mini, co-examiner

2003

Contents

Contents	III
Abstract.....	V
Zusammenfassung.....	VII
Introduction	1
1.1 CANCER.....	1
1.2 RADIOTHERAPY USING HIGH-ENERGY PHOTONS.....	1
1.3 CONFORMAL RADIOTHERAPY	3
1.4 INTENSITY MODULATED RADIOTHERAPY.....	5
1.5 IMRT IN CLINICAL PRACTICE.....	8
1.6 VERIFICATION OF IMRT	8
1.7 VERIFICATION USING AN ELECTRONIC PORTAL IMAGING DEVICE	9
1.8 AIMS OF THIS STUDY	12
The PortalVision™ aS500 EPID	15
2.1 OVERVIEW	15
2.2 GENERAL DESCRIPTION OF THE PORTAL VISION™ AS500	15
2.3 HYDROGENATED AMORPHOUS SILICON	16
2.4 PHOTODIODE AND THIN-FILM TRANSISTOR	17
2.5 INDIRECT DETECTION OF HIGH-ENERGY PHOTONS	19
2.6 LINEARITY OF THE SIGNAL	20
2.7 STABILITY OF THE SIGNAL.....	24
2.8 IMPACT OF DETECTOR COMPONENTS	26
Physical Characteristics of the EPID	31
3.1 OVERVIEW	31
3.2 QUANTUM ACCOUNTING DIAGRAM ANALYSIS	31
3.3 SIGNAL FORMING STAGES	32
3.4 MONTE CARLO SIMULATIONS.....	34
3.5 ENERGY DEPOSITION IN THE PHOSPHOR LAYER.....	35
3.6 SPREAD OF HIGH-ENERGY PARTICLES.....	47
3.7 PRODUCTION OF OPTICAL PHOTONS.....	51
3.8 TRANSPORT OF OPTICAL PHOTONS.....	53
3.9 COLLECTION AND DETECTION OF OPTICAL PHOTONS	56
3.10 QAD AND DQE OF THE PORTAL VISION™ AS500.....	56

Calculation of Portal Dose Images	59
4.1 OVERVIEW	59
4.2 MULTIPLE SOURCE MODEL.....	59
4.3 MONTE CARLO SIMULATION OF DMLC DELIVERY	61
4.4 PORTAL DOSE IMAGE CALCULATION	62
4.5 PDIs FOR REAL TREATMENTS USING THE MSM AND DOSXYZ.....	67
Measurement of Portal Dose Images.....	69
5.1 OVERVIEW	69
5.2 FIELD SIZE DEPENDENCE.....	69
5.3 DOSE CALIBRATION OF THE EPID	73
5.4 ACQUISITION OF A PDI FOR DYNAMICALLY APPLIED FIELDS	79
5.5 DYNAMIC SLIT BEAM DELIVERIES	81
5.6 SPECTRAL CHANGES CAUSED BY DMLC	84
5.7 IMPACT OF SPECTRAL CHANGES ON EPID DOSIMETRY	87
5.8 PDIs OF CLINICALLY RELEVANT TEST FIELDS.....	90
Verification of IMRT	95
6.1 OVERVIEW	95
6.2 GAMMA-EVALUATION METHOD.....	95
6.3 OVERVIEW OF THE CASES STUDIED.....	98
6.4 PYRAMID.....	98
6.5 HEAD AND NECK CARCINOMA.....	99
6.6 BRONCHUS CARCINOMA	101
6.7 FIRST IMRT TREATMENT	102
Discussion.....	111
7.1 IMRT IMPLEMENTATION AND VERIFICATION	111
7.2 DOSIMETRIC IMRT VERIFICATION USING AN A-Si:H EPID.....	111
7.3 SIGNAL FORMATION STUDY USING MONTE CARLO SIMULATIONS.....	112
7.4 ENERGY RESPONSE STUDY USING MONTE CARLO SIMULATIONS	113
7.5 MONTE CARLO SIMULATIONS FOR PORTAL DOSE CALCULATIONS.....	113
7.6 THE GAMMA-EVALUATION METHOD	114
7.7 VERIFICATION OF IMRT IN CLINICAL ROUTINE	115
7.8 FUTURE DETECTOR DESIGN FOR HIGH-PRECISION DOSIMETRY	116
7.9 FUTURE: ESTIMATION OF DOSE DELIVERED TO THE PATIENT.....	116
References	117
Acknowledgements.....	127
Curriculum Vitae	129

Abstract

Intensity modulated radiotherapy (IMRT) permits to deliver dose distributions conformally to the tumor while simultaneously the dose to organs-at-risk is minimized. Based on inverse treatment planning systems, non-uniform beam intensities are optimized. IMRT represents one of the most significant advances in conformal radiotherapy. The implementation of IMRT into clinical practice depends, however, critically on its verification: due to the complexity of IMRT compared with conventional radiotherapy techniques, the quality assurance is of utmost importance.

In this work, an amorphous silicon (a-Si:H) based electronic portal imaging device (EPID) is employed to establish the verification of IMRT. For this purpose, the dosimetric pre-treatment verification (before actually treating the patient) as well as the treatment verification (*in vivo* dosimetry) are investigated.

Prerequisite for dosimetric applications of the EPID is the accurate knowledge of its physical characteristics. In this thesis, the signal formation is subdivided into eight signal forming stages and the performance of the EPID is analyzed by the quantum accounting diagram (QAD) analysis. In order to calculate the energy deposition in the phosphor layer of the detector, Monte Carlo (MC) simulations are performed. Energy response studies are carried out and the influence of different detector components and interaction types are investigated to provide an accurate description of the EPID.

For dosimetric verification purposes, a pre-calculated portal dose image (PDI) is required. However, due to the large airgap between the portal plane and the patient, current treatment planning systems are unable to calculate a PDI. In this thesis, the MC method is applied for portal dose predictions of static and dynamic beam deliveries. A multiple source model (MSM) is used to describe the photon beam for 6 and 15 MV of a Varian Clinac 2300 C/D. In order to calculate portal dose distributions for dynamically applied fields, a multileaf collimator (MLC) is implemented into the beam model. Excellent agreement to measured data using film dosimetry is achieved.

The actual verification consists in the comparison between a pre-calculated PDI and a measured PDI. In this work, the a-Si:H based PortalVisionTM aS500 is employed for the measurement of portal dose distributions. The linear dose response relationship as well as the well established stability of the signal are making this EPID a promising candidate for dosimetric purposes. However, as

shown in this thesis, care has to be taken due to the impact of spectral changes on EPID dosimetry, particularly for the treatment verification. After the calibration to dose, the PortalVisionTM aS500 measured PDIs reveal good agreement to those measured by film or an ionization chamber.

In order to quantify the verification process, a special metric (gamma-evaluation method) is applied considering simultaneously the differences in dose and the differences in space. This concept is evaluated for different clinical situations. It turns out, that the gamma-evaluation method is a suitable method for the verification of IMRT by the use of an EPID.

In conclusion, the a-Si:H EPID plus MC methods have been successfully used for the dosimetric verification of IMRT for pre-treatment and treatment situations.

Zusammenfassung

Die Intensitätsmodulierte Radiotherapie (IMRT) ermöglicht eine konforme Bestrahlung des Tumors bei gleichzeitiger Schonung des gesunden Gewebes. Die inhomogenen Intensitäten werden mit Hilfe inverser Therapieplanungstechniken berechnet und optimiert. Aufgrund der Komplexität der IMRT kommt der Qualitätssicherung grösste Bedeutung zu. Die Einführung der IMRT in die klinische Routine ist daher stark von der Verifikation abhängig.

In der vorliegenden Arbeit wird ein auf amorphem Silizium (a-Si:H) basierendes Portalbildsystem (EPID) zur dosimetrischen Verifikation der IMRT eingesetzt werden, sowohl vor der Bestrahlung des Patienten (Verifikation der Therapieplanung) als auch der Bestrahlung selber (*in vivo* Dosimetrie). Der Einsatz eines EPIDs stellt die dosimetrische Verifikation auf eine neue Basis, da es damit erstmals möglich ist, in Echtzeit die zweidimensionale Dosisverteilung zu kontrollieren.

Eine Voraussetzung für den dosimetrischen Einsatz des EPIDs ist die Kenntnis der physikalischen Eigenschaften dieses Systems. Dazu wird die Signalerzeugung in acht Schritte zerlegt und mittels der ‚Quantum accounting diagram‘ (QAD) Technik analysiert. Mit Hilfe von Monte Carlo (MC) Simulationen wird so dann die Energiedeposition in der Phosphorschicht berechnet. Eine genaue Beschreibung des EPIDs erfolgt durch die Untersuchung der Energieantwort und des Einflusses verschiedener Detektorkomponenten und Wechselwirkungsmechanismen.

Zur dosimetrischen Verifikation müsste ein vom Therapieplanungssystem berechnetes portales Dosisbild (PDI) mit einem gemessenen Dosisbild verglichen werden. Leider sind die heutigen Therapieplanungssysteme nicht in der Lage ein PDI zu berechnen. Daher musste ein Verfahren zur Berechnung der PDI für statische und dynamische Bestrahlungen entwickelt werden. Das auf MC Methoden beruhende Verfahren benutzt ein ‚Multiple Source Model‘ (MSM), welches einen Photonenstrahl für 6 und 15 MV eines Varian Clinac 2300 C/D zu beschreiben vermag. Die Berechnung der portalen Dosisverteilung für dynamisch applizierte Felder benötigt zudem die Implementierung eines Multileaf Kollimators (MLC). Die Messung der portalen Dosisverteilungen erfolgte mit dem in dieser Arbeit analysierten EPID System von Varian Medical Systems, dem PortalVisionTM aS500. Die lineare Dosisantwort und die gute Stabilität des Detektorsignals machen dieses System zu einem vielversprechenden Kandidaten

für dosimetrische Aspekte. Allerdings birgt die fehlende Wasseräquivalenz gewisse Probleme, wie etwa der Einfluss spektraler Änderungen auf die EPID Dosimetrie. Zur Kontrolle dieses Verfahrens wurden Testbilder und reale Fälle berechnet und mit Filmedosimetrie sowie Ionisationskammermessungen verglichen. Die Resultate waren sehr zufrieden stellend.

Eine weitere Aufgabe stellte sich in der Quantifizierung der Verifikation: Die Abweichungen zwischen berechneten und gemessenen PDI müssen bewertet werden. Dazu wurde das Gamma-Evaluationsverfahren eingesetzt. Diese Metrik berücksichtigt gleichzeitig die dosimetrischen wie auch die räumlichen Differenzen zwischen zwei Dosisverteilungen. Dieses Konzept wurde für verschiedene, klinische Situationen überprüft. Es zeigt sich, dass diese Gamma-Evaluations-methode ein geeignetes Instrument für die Verifikation von IMRT darstellt.

In der vorliegenden Arbeit wurde gezeigt, dass das a-Si:H EPID und MC Methoden erfolgreich für die dosimetrische Verifikation von IMRT eingesetzt werden können.

1

Introduction

1.1 CANCER

At present, in Europe, one of three people will suffer from cancer during their lifetimes while one of four will die of this disease (Levi *et al.* 1998). For the treatment of cancer, radiotherapy is one of the major methods for more than 50% of the patients. Surgery and chemotherapy are other modalities to treat malignant tumors (van Dyk 1999).

As reported by Amaldi (1999), 45% of all cancer patients are cured at present. Most of them (90%) are cured due to a locally confined (not metastasized) primary tumor. Radiotherapy alone and in combination with surgery succeeds in 12% and 6% of the cases, respectively. Hence, radiotherapy contributes to almost every second curative treatment of the primary tumor. However, for 55% of all patients no curative treatment is available. More precisely, 18% of all patients can not be cured although the tumor is locally confined at the time of diagnosis. This means that an improved control of primary tumors could boost the percentage of the cured patients from 45% to about 65%, so that two of three patients could be cured.

Recent developments in radiotherapy focus on these 18%. At present, intensity modulated radiotherapy (IMRT) using high-energy photons is commonly seen as one of the most promising technologies.

1.2 RADIOTHERAPY USING HIGH-ENERGY PHOTONS

Historically, the beneficial use of ionizing radiation for the treatment of cancer was found immediately after the discovery of X-rays by Röntgen. Already in 1897, Freund applied X-rays for the treatment of malignant skin diseases (CERN 1996), whereas the first curative treatment was reported in 1899 (Perez *et al.* 1998). However, it was not until computed tomography (CT) in

1972 became available that accurate localization of the tumor and the normal tissues was accessible. Anyway, the increase in power and reliability of computers had a revolutionary impact in all the fields of medical physics.

The radiation effect on biological tissues is a result of the energy deposited in the cells. Energy deposition is carried out by ionization and excitation of the material's atoms and molecules. Physically, the energy deposition is described by dose which is defined as the energy absorbed by the medium per unit mass (unit: $1\text{Gy} = 1\text{J/kg}$). Of great importance is the fact that radiation does not distinguish between malignant cells and normal tissue. The tumor control probability (TCP) describes the relationship between the probability that the tumor is eradicated and the dose delivered to the tumor. Likewise, the relationship between normal tissue complication and dose delivery is referred to as the normal tissue complication probability (NTCP). The sigmoidal relationship is a common feature for both TCP and NTCP.



Figure 1.1 During the irradiation, the patient is lying on the couch under the treatment machine (gantry). High-energy photons are generated by bremsstrahlung within a target. In order to irradiate the tumor from different beam directions, the gantry can be rotated.

The aim of using radiotherapy as a cancer treatment modality can be curative or palliative. Cure is only achieved if every malignant cell is destroyed. For this purpose, radiotherapy aims to deliver sufficiently high doses to diseased tissue leading to tumor control and to deliver as low dose as possible to normal tissues resulting in small side effects. Due to improved cure rates, radiotherapy is given in fractions, where a typical total dose of 60 Gy is subdivided into 30 fractions of 2 Gy each.

During treatment, as shown in Figure 1.1, the patient lies on a couch under the treatment machine (gantry). Usually, radiotherapy utilizes several high-energy photon beams from different directions to eradicate deep-seated tumors within the human body. Over the course of the 1970's, medical linear accelerators (linacs) superseded the betatrons and the ^{60}Co units. Linacs accelerate electrons to about 4 to 25 MeV using microwave RF fields and produce megavoltage (MV) photons by bremsstrahlung. To obtain a homogeneous energy fluence, a flattening filter is needed to correct for the prominent forward direction of the bremsstrahlung's photons. Due to possible fluctuations of the linac, a dose monitor system is required to ensure constant output. This so-called monitor chamber consists of two ionization chambers which check the monitor units (MU) delivered by the machine. Usually, the system is calibrated such that 1 MU corresponds to a dose of 1 cGy delivered in a water phantom under reference conditions ($10 \times 10 \text{ cm}^2$ field, 10 cm water depth with a source-to-surface distance $SDD=90 \text{ cm}$).

1.3 CONFORMAL RADIOTHERAPY

In order to tailor the high-dose region to the target volume and simultaneously spare the organs-at-risk (OAR), conformal radiotherapy (CFRT) demands for collimated photon beams. Linacs usually feature a multileaf collimator (MLC) to shape radiation fields under computer control. The MLC consists of a series of metal leaves fixed to the linac head. Each leaf can be positioned individually so that the setting of the MLC determines the shape and intensity distribution of the photon beam delivered to the patient. A photograph of an 80-leaf MLC (Varian Medical Systems) is shown in Figure 1.2. Detailed information about the design and the composition of an MLC can be found in the literature (Huq *et al.* 2002, AAPM 2001, Galvin *et al.* 1993).

In addition to the delivery system, the process of treatment planning is very essential for successful radiotherapy. During treatment planning, the dose distributions within the patient are calculated by using CT based information

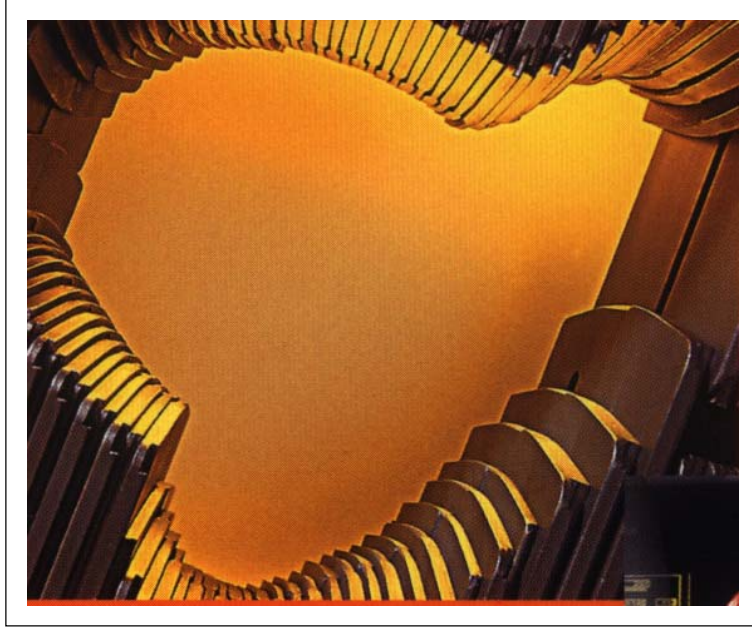


Figure 1.2 In conformal radiotherapy, a multileaf collimator (MLC) enables the delivery of non-rectangular fields. In the figure, an 80-leaf MLC of Varian Medical Systems is shown (courtesy of Varian Medical Systems).

about the patient's anatomy. In recent years, the accuracy of treatment planning systems has been improved mainly due to more accurate dose calculation methods. Nowadays, most commercially available treatment planning systems are based on the convolution-superposition algorithm (Mackie *et al.* 1985, Boyer and Mok 1985, Mohan *et al.* 1986, Ahnesjö *et al.* 1992). To calculate the dose $D(x, y, z)$ within the patient, this algorithm convolves the total energy released (TERMA in J/kg) $T(x, y, z)$ with a photon dose kernel $K(x, y, z)$:

$$D(x, y, z) = T(x, y, z) * K(x, y, z).$$

The TERMA T describes the energy deposited in a medium by primary photon interactions. For a monoenergetic photon beam, T is given by the photon fluence $\phi(x, y, z)$, the mass attenuation coefficient μ / ρ and the energy E :

$$T(x, y, z) = \frac{\mu(E)}{\rho} \cdot \phi(x, y, z) \cdot E.$$

The dose kernel K is calculated either by Monte Carlo (MC) simulations or from measurements. However, in real situations, the photon beam is not

monoenergetic but consists of an energy spectrum. As a consequence, a superposition of T and K is needed to account for polyenergetic beams.

In CFRT the beam energy and directions as well as the shapes are optimized by forward treatment planning. Thereby, the optimization process comprises the evaluation of a number of treatment plans obtained for several different beams. As a consequence, the precision of CFRT – or the conformality of the dose distributions to the target volume – depends significantly on the human who is ‘optimizing’ the plan.

1.4 INTENSITY MODULATED RADIOTHERAPY

Inverse treatment planning determines the intensity distributions required to deliver the dose conformally to the target volume. Figure 1.3 shows schematically the principle of this method and the concept of intensity modulated radiotherapy (IMRT). The analogy to computed tomography is apparent: whereas in inverse treatment planning the intensities are obtained from prescribed dose distributions, computed tomography calculates the density distribution (actually

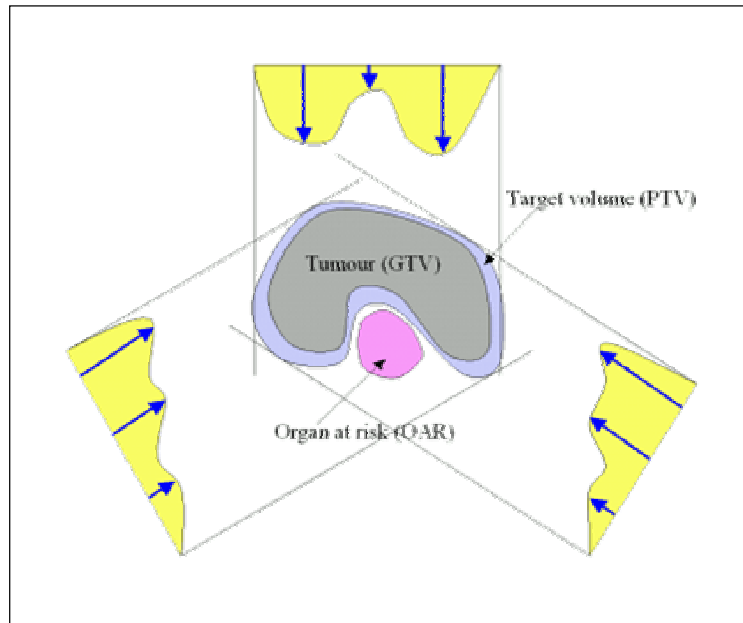


Figure 1.3 Intensity modulated radiotherapy (IMRT) is based on inverse treatment planning. During this process, the intensities needed to achieve the desired dose distributions are calculated by iterative methods. The figure shows schematically an example of three intensity modulated photon beams with different directions. The overlay of these beams results in a homogeneous dose distribution within the planning target volume (PTV). In addition, the organ at risk (OAR) is spared by delivering the dose conformally to the tumour (GTV).

the attenuation coefficients) from measured projections of intensities. However, it was shown, that this analogy is inappropriate due to the fact that negative, and therefore physically unrealistic, intensities turn up (Cormack 1987, Webb 1993).

Commercial inverse treatment planning systems determine the intensity by optimizing an objective function. The objective function represents the quality of a plan and can be based on dose alone or it can account for biological effects caused by radiation. Typically, the TCP is maximized while the NTCP is maintained to within tolerable levels (Wang *et al.* 1996a). But these optimization methods based on biological models are currently not very common. Most of the time, a quadratic objective function is optimized by the use of iterative methods (Stein 1997).

In terms of dose calculation, most commercial inverse treatment planning systems are based on fast algorithms such as pencil beam dose calculations (Mohan *et al.* 1986, Mackie *et al.* 1985, Ahnesjö *et al.* 1992). However, the most accurate method for calculating dose within inhomogeneous tissues is the MC method (Mohan 1997, Jerai *et al.* 2002). In order to overcome the very long computing time, adapted MC methods were developed recently (Fix *et al.* 2001a,b and references therein).

The delivery of intensity modulated beams can easily be performed by the use of physical compensators (Boyer 1982, Mageras 1991). In this case, the modulation is realized by the absorption of the photons according to the law of Beer-Lambert. Though, compensating filters have a number of drawbacks such as the very time-consuming construction and the requirement of re-entering the treatment room for positioning, which makes this approach not very widespread. In recent years, several methods have been developed to enable the delivery of modulated intensities with a conventional MLC.

In the step-and-shoot method, the intensity distribution is approximated by discrete levels of intensity (Bortfeld *et al.* 1994). Each intensity level is delivered separately, resembling the delivery of multiple static fields. The beam is only turned on when the leaves are located at their prescribed positions. Although very intuitive and easy to verify, the step-and-shoot method has a number of drawbacks such as the long delivery time (Chui *et al.* 2001). In addition, the delivery of small fields and only a few MU is a crucial point leading to variations of linac output and beam characteristics (Barish *et al.* 1987, Hansen *et al.* 1998, Cheng and Das 2002).

Another method for the delivery of intensity modulated beams is the sliding-window technique (Convery and Rosenbloom 1992, Spirou and Chui 1994, Stein *et al.* 1994). In contrast to the step-and-shoot method – where the leaves of the

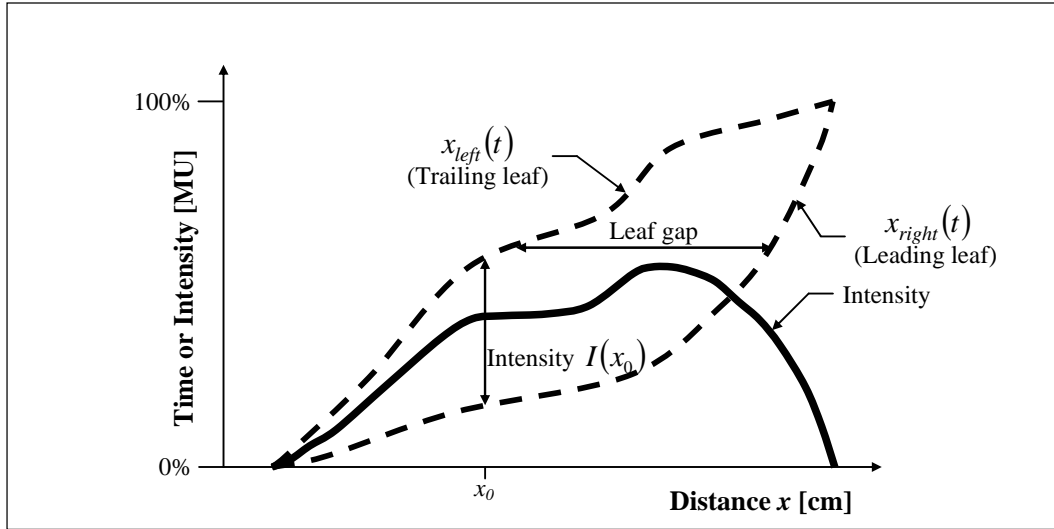


Figure 1.4 IMRT delivery by the use of the sliding-window technique. During the irradiation, the leaves are dynamically moved with varying speed.

MLC are only moved when the beam is off - the sliding-window technique is based on the dynamic operation of the MLC (DMLC). As illustrated in Figure 1.4, the intensity distribution is delivered by adjusting the speed and the gap of the two leaves building a leafpair. The figure shows the leaf positions $x_{right}(t)$ and $x_{left}(t)$ for the leading and the trailing leaves, respectively, as a function of cumulative time t . For a given dose rate \dot{D} (in MU/min) the time t is also a representation of the total MUs delivered. At a given point x_0 the distance $\text{MU}_{left}(x_0) - \text{MU}_{right}(x_0)$ is the intensity (in MU) delivered to this point. In commercial inverse treatment planning systems, the MLC leaf trajectories are calculated by a leaf sequencing algorithm. This is usually performed after the beam optimization. The leaf sequencer accounts for the limitations of the MLC such as leaf transmission, rounded leaf ends, tongue-and-groove design, and leaf scatter (LoSasso *et al.* 1998, Arnfield *et al.* 2000).

With IMRT a higher target dose conformity is achievable compared to conventional CFRT (Eisbruch 2002). As has been estimated in the literature (Nutting *et al.* 2000), 30% of tumors exhibit a concavity in the planning target volume (PTV) for which only IMRT is adequate. In this thesis, as was recommended by the Intensity Modulated Radiation Therapy Collaborative Workin Group (IMRT CWG 2001), the term IMRT is assigned to radiotherapy treatments using inverse planning for beam optimization.

1.5 IMRT IN CLINICAL PRACTICE

Although the basic concepts of inverse treatment planning and the requirement to move the leaves during the delivery were established already in the late 80's, it was not until the mid 90's when the first patients were treated with IMRT. The first IMRT patient has been treated in 1995 at the Memorial Sloan Cancer Center in New York (Ling *et al.* 1996). Since then IMRT has been further implemented at several centers all around the world (Burman *et al.* 1997, Lee *et al.* 2002, Nutting *et al.* 2000). In Switzerland, the university hospital of Zurich (Korevaar and Davis 2002) and the Inselspital Berne reported their first IMRT treatments using DMLC (Vetterli *et al.* 2002a).

The main impediment of the implementation of IMRT into clinical practice is quality assurance (QA). Bearing in mind that IMRT techniques are significantly more complex than conventional treatments, the need for accurate QA procedures is obvious. However, current methods for IMRT testing and verification are not yet well established (IMRT CWG 2001).

1.6 VERIFICATION OF IMRT

The implementation of IMRT into clinical practice depends critically on its verification procedure. Due to the increased complexity introduced by inverse treatment planning and the use of DMLC in IMRT, accurate verification is a major issue. The pre-treatment verification is the process where the dose distributions are verified before actually treating the patient. Usually this is performed by comparing calculated and measured dose distributions within a homogeneous water (or water-equivalent) phantom. For this purpose, the patient's treatment plan has to be converted to this particular situation. The measurement of the dose distributions is performed by the use of thermoluminescent detectors (TLDs), semiconductor diodes, or ionization chambers. A common feature of all these devices is that they are only point-measurement devices. Thus, since the dose distributions of IMRT plans are non-uniform, the correct positioning of the measurement points has to be conducted. In addition, for the verification of dynamically applied fields, these tools involve the measurement of the entire field for every point, which makes the use of these devices very time-consuming. Although two-dimensional, the use of radiographic films is unfavorable because films need to be developed and digitized. Moreover, absolute film dosimetry is a non-trivial problem since the relationship between optical densities and absolute dose values is rather difficult to measure. The accuracy of absolute film dosimetry is about only 5% (Mayer

et al. 1997). In addition, due to saturation effects the verification of IMRT using film dosimetry sometimes requires to apply a reduced amount of MUs than planned. This implies the intensity modulated field to be delivered faster than originally intended. Recent publications show that this may introduce different beam characteristics (Vieira *et al.* 2002, Xia *et al.* 2002). Nevertheless, film dosimetry is a standard for the pre-treatment verification of IMRT (Chui *et al.* 1996, Wang *et al.* 1996b).

In contrast to the pre-treatment verification, treatment verification aims to verify the dose actually delivered to the patient. This kind of verification is also called *in vivo* dosimetry and is routinely used in different clinics. In some countries (Sweden and Denmark), *in vivo* dosimetry is mandatory even for conventional (i.e. not intensity modulated) treatments. Usually the entrance- or the exit-dose are measured by the same point measuring devices indicated above. However, correct positioning is exceedingly difficult leading to extra-time for the patient lying on the treatment couch and to misleading interpretations. As has been shown by Essers *et al.* (1995), point detectors are not accurate enough for treatment fields with high dose gradients. Hence, for IMRT - where high dose gradients exist inherently - the need for two-dimensional detectors is obvious.

1.7 VERIFICATION USING AN ELECTRONIC PORTAL IMAGING DEVICE

The development of electronic portal imaging devices (EPIDs) originally intended to replace the cumbersome film for correct patient set-up. The basic principle of portal imaging lies in the fact that high-energy photons transverse an object (the patient) as described by the law of Beer-Lambert. Whereas these photons do not contribute to the dose delivered to the tumor, they are informative for correct patient positioning. For this purpose, EPIDs generate an image containing information about the anatomical structures of the patient. Most challenging is the circumstance that high-energy photons possess low contrast due to small differences in the attenuation coefficients of the patient's material composition. In the last few years several new technical approaches for the construction of EPIDs have been developed (Antonuk 2002). In terms of image quality, amorphous silicon (a-Si:H) based EPIDs are most promising and are commercially available since 1999. Figure 1.5 shows the PortalVisionTM aS500 (Varian Medical Systems) mounted on a linac as well as a portal image obtained with only 1 MU (Vetterli *et al.* 2002b).

As has been reported in the literature (Kirby and Williams 1993, Hansen *et al.* 1996), EPIDs are not only able to generate anatomical information but are also

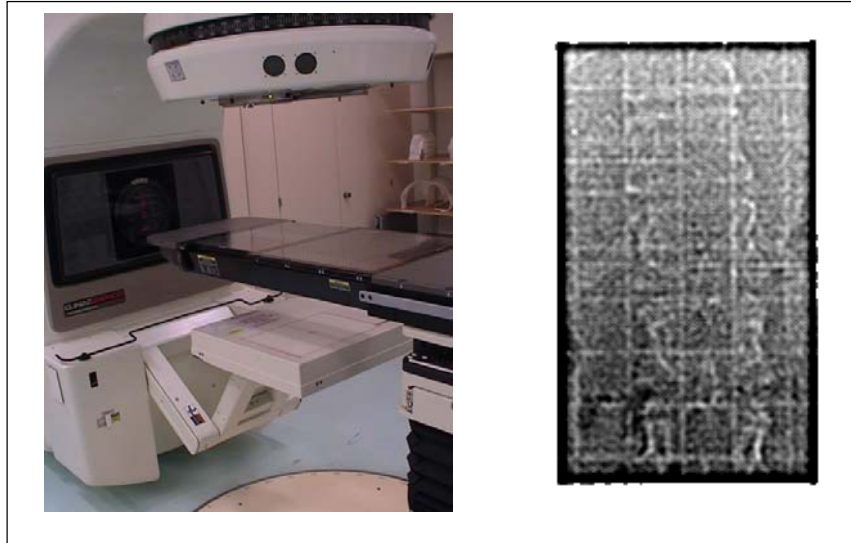


Figure 1.5 Left: the amorphous silicon based PortalVision™ aS500 mounted on the linac. The EPID can be positioned at different source-detector-distances. Right: a typical portal image of a posterior-anterior field. Note that the anatomical details are clearly visible although this image is obtained with only 1 MU.

useful to receive information about the output of the treatment unit, such as the measurement of beam flatness and beam symmetry. Furthermore, EPIDs have the potential to measure portal doses in a two-dimensional manner (Kirby and Williams 1995). This feature as well as the fact that EPIDs can be positioned very accurately make EPIDs good candidates for verification purposes. In addition, EPIDs are acquiring images in real time which is a substantial improvement compared to films. Basically, two different methods were developed to verify the treatment by the use of an EPID.

The measurement of leaf position during the delivery of a dynamically applied field is an approach aiming to verify that the leafmotion is such as intended at the planning stage. Partridge *et al.* (2000) investigated three different EPIDs for the assessment of leaf trajectories by monitoring DMLC treatment deliveries. The first EPID considered was developed by Mosleh-Shirazi (1998) and consists of a charged coupled device (CCD) camera viewing a scintillation screen built from 10 mm thick CsI crystals. The synchronization between the image acquisition and the linac pulse production allows acquiring one image per linac pulse. The other two systems considered in this study are commercially available EPIDs. The scanning liquid-filled ionization chamber (SLIC) system was developed by van Herk *et al.* (1988, 1991). Keller *et al.* (2000) investigated theoretically the feasibility of the SLIC EPID for leafmotion verification. By analyzing the non-

linear dose rate response and the crucial behavior in non-equilibrium states, Keller *et al.* concluded that for a typical maximum leaf speed of about 2 cm/s, frame cycle times of less than 1 s are required. The third EPID examined in the study of Partridge *et al.* (2000) is based on a metal/phosphor screen combination and a CCD camera and is described in more details by James *et al.* (2000). For geometric verification of IMRT, the positions of the leaves are determined by applying field edge detection so that the 50% intensity level is compared to the prescribed position (Partridge *et al.* 1998, Eilertsen *et al.* 1997). In conclusion, Partridge *et al.* (2000) demonstrated similar performance for all three systems investigated. For leaf position, an overall accuracy of about 1.0 mm was reported. However, LoSasso *et al.* (1998) had shown that an MLC position precision of 1.0 mm lead to dosimetric errors of 5% or 10% for a dynamic slit beam delivery (see Section 5.5) with a nominal gap of 2 cm or 1 cm respectively. As a consequence, the dosimetric accuracy obtained by the assessment of leaf positions with an EPID is not sufficient if highly modulated beams are used (Vieira *et al.* 2002).

The second verification approach using an EPID encompasses the dosimetric information underlying in portal images (Partridge *et al.* 1999, Pasma *et al.* 1999). For static treatments, Boellaard *et al.* (1998) investigated the SLIC EPID for the estimation of the midplane dose from a measured portal image. The same EPID was applied by Curtin-Savard *et al.* (1999) for the dosimetric verification of intensity modulated beams delivered by the step-and-shoot technique. Curtin-Savard *et al.* (1999) as well as Keller *et al.* (2000) concluded that the SLIC EPID's underlying physics (mainly the long-term memory effect) deters its use for verification of dynamic beam delivery. In order to overcome the fundamental memory effects inherent to the SLIC EPID, Chang *et al.* (2000) increased the MU per field to simulate higher frame rates, which makes this approach only feasible for pre-treatment verification purposes. Chang *et al.* concluded that treatment verification requires a frame acquisition time of about 1 s. However, due to improved image acquisition van Esch *et al.* (2001) demonstrated accurate dosimetric images of dynamically applied fields. Additionally, the memory effect was found to be of no clinical relevance. Pasma *et al.* (1999) applied a video-based EPID for the measurement of so-called portal dose images (PDIs). A PDI is the two-dimensional dose distribution in the portal plane which is perpendicular to the central beam axis. The actual verification consists in the comparison between the measured and a predicted PDI, as derived from a dedicated numeric algorithm (Pasma *et al.* 1998). With this verification procedure, Pasma *et al.* (2002) demonstrated for a clinical study with prostate

cancer patients dosimetric differences on the central axis of typically 1-2%. However, larger differences occurred for patients with varying rectal filling and for off-axis locations indicating organ motion.

1.8 AIMS OF THIS STUDY

The aim of this study is to investigate the potential of the PortalVisionTM aS500 and a-Si:H based EPID for the dosimetric verification of IMRT. For this purpose, the general concept of dosimetric IMRT verification is based on the comparison between measured and calculated portal dose images (PDIs). For pre-treatment as well as treatment verification, this approach enables to quantify the quality of the delivery by recovering problems like incorrect dose delivery by the treatment unit and differences in patient's anatomy due to variations occurred during the time of planning and the time of treatment (Kroonwijk *et al.* 1998). Moreover, as being an online-tool, the use of an EPID for the measurement of PDIs reduces the enormous effort of current IMRT verification methods and thus supports strongly the successful implementation of IMRT in clinical routine.

Chapter 2 gives a short description of the PortalVisionTM aS500 and provides a basic comprehension of this particular EPID. It elucidates how the EPID is constructed and how high-energy photons are detected. Finally, the linearity of the pixel signal as well as its stability properties is investigated.

In Chapter 3 a detailed analysis of the detector's physical characteristics is given. For this purpose, the signal formation is divided into eight stages. According to the so-called quantum accounting diagram (QAD) analysis, each stage is explored. Monte Carlo simulations are used to study the energy deposition in the phosphor screen of the EPID. In addition, a model for the transport of optical photons within the phosphor layer is developed.

In order to predict a PDI, Chapter 4 is dedicated to the calculation of portal dose images. Based on a multiple source model of a Varian Clinac 2300 C/D, Monte Carlo simulations are used to simulate the transport of high-energy photons through the MLC for dynamically applied fields. From these simulations, PDIs are calculated for pre-treatment as well as for treatment verification intentions. The use of Monte Carlo simulations fulfills the demand on a verification method being fully independent of the original treatment planning system.

Chapter 5 deals with the measurement of portal dose images using the PortalVisionTM aS500. After the calibration of the pixel signal to dose, PDIs are

measured for different photon beams. Particularly for dynamically applied fields, it is necessary that the entire dose information is detected by the EPID.

The verification of IMRT is demonstrated in Chapter 6, where several test fields as well as different clinical fields are verified. For the quantitative comparison between measured and calculated portal dose images, the gamma-evaluation method (Low *et al.* 1998) is applied. This method allows assessing simultaneously the dosimetric and spatial differences between two images.

In Chapter 7, a general discussion of the methods and the results are provided.

2

The PortalVisionTM aS500 EPID

2.1 OVERVIEW

The benefits of electronic portal imaging can only be realized if the efficient detection and the real time viewing of high-energy photon beams are established in a clinical environment. These days, a number of commercial systems with different physical principles of photon detection are available. Most common are video-based EPIDs and the scanning liquid ionization chamber (SLIC) EPID. More recently, hydrogenated amorphous silicon (a-Si:H) based flat-panel detectors have been developed offering better image quality (Antonuk *et al.* 1992, Munro *et al.* 1998). Reviews of EPIDs can be found in the literature (Boyer *et al.* 1992, Munro 1995, Antonuk 2002, Langmack 2001). In this chapter, a short description of the a-Si:H based PortalVisionTM aS500 (Varian Medical Systems) is given.

2.2 GENERAL DESCRIPTION OF THE PORTALVISIONTM AS500

Figure 2.1 shows a photograph of the image detection unit (IDU) of the PortalVisionTM aS500. The IDU is a 1024×768 pixel array with a pixel pitch of $392 \mu\text{m}$. This leads to a total area of $40 \times 30 \text{ cm}^2$. Each pixel consists of a photodiode and a thin-film transistor (TFT), which are the two elements being composed of a-Si:H. In order to position the EPID at different source-detector-distances (SDDs), the IDU is attached to a robotic arm (cf. Figure 1.5). For signal readout purposes, the IDU is equipped with associated electronics and the image acquisition computer (IAS2) is connected to the IDU to control the image acquisition. Eventually, the image data is transferred to a standard personal computer for graphical display and analysis.



Figure 2.1 A photograph of the amorphous silicon based detection unit (IDU) of the PortalVision™ aS500. The IDU consists of 1024×764 pixels with a pixel pitch of $392 \mu\text{m}$ resulting in a total area of $40 \times 30 \text{ cm}^2$. Next to the sensor, electronics is required for the acquisition of a portal image.

2.3 HYDROGENATED AMORPHOUS SILICON

As has been reported elsewhere (Street 2000), research on amorphous silicon is performed since 1960. After several years of confusion and frustration, it was the successful doping after the incorporation of hydrogen into amorphous silicon, which was responsible for a number of applications. Most commonly known are photovoltaic applications (i.e. solar cells) and the active matrix liquid crystal displays.

Amorphous silicon differs from crystalline silicon by its atomic structure. While the degree of order for small atomic distances is rather the same for amorphous and crystalline silicon, the atomic structure for amorphous silicon is totally randomized at large scales. The energy gap of a-Si:H is 1.7 eV and the drift mobility is $1 \text{ cm}^2/\text{Vs}$ for electrons and $0.003 \text{ cm}^2/\text{Vs}$ for holes, respectively. Despite the fact that hydrogen incorporation decreases the number of dangling bond defects in the middle of the energy gap, these defects are even more prevalent for doped materials. As a result, a-Si:H sensors are preferably constructed as p-i-n photodiodes (Madan and Shaw 1988, p 219).

2.4 PHOTODIODE AND THIN-FILM TRANSISTOR

The two main applications of a-Si:H are the photodiode and TFT, which will be described subsequently. In Figure 2.2 the design of the flat-panel array is illustrated schematically.

Essentially, the photodiode consists of two thin doped layers (n- and p-doped, respectively) and an intrinsic i-layer in between. The detection of optical photons by such a photodiode relies on a reverse biased pn-junction (Saleh and Teich 1991). For this reason, the diode requires a transparent conductor (indium tin oxide for the PortalVision™ aS500) for the illuminated surface. The incoming photon generates an electron-hole pair in the depletion layer, which leads to a reverse current in the external circuit. The relation between the photocurrent I and the incoming photon flux Φ_{light} is

$$I = \Phi_{light} \cdot \eta_{diode},$$

where η_{diode} denotes the quantum efficiency and depends on the wavelength of the incident photon and the applied bias voltage. In addition to the detection task, the photodiode acts as a capacitor of the generated charge in the i-layer. As has been derived in the literature (Antonuk *et al.* 1997), the pixel charge capacity is a function of the applied bias voltage V_{bias} and the sensor's capacity C_{pd}

$$Q_{pd} = C_{pd} \cdot V_{bias}.$$

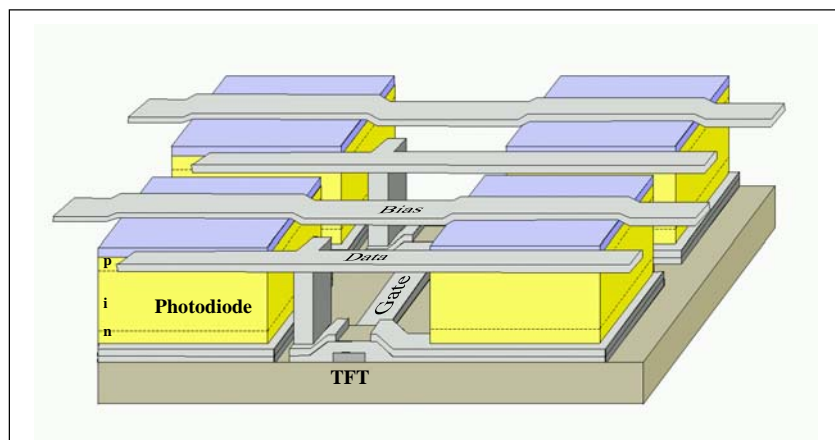


Figure 2.2 The photodiode consists of a p-i-n structure of a-Si:H material. A transparent conductor on the front and a metal contact on the bottom are required to provide a reverse biased voltage. The incident photon generates an electron-hole pair in the depletion layer of the photodiode which then leads to a reverse photocurrent in the external circuit. Each pixel encompasses a thin-film transistor (TFT) for readout purposes (see text for more details).

Table 2.1 provides some of the key parameters of the photodiode used for the PortalVision™ aS500.

These days, a well-known application of TFTs is its use in active matrix liquid crystal displays for laptop computers. For the EPID, TFTs are used to control the readout of the photodiode. For this purpose, each pixel of the detector incorporates a TFT, as shown in Figure 2.2 and the readout of the entire array is performed by correctly adjusting the conductivity of the TFTs on a row-by-row scheme. During the acquisition, a negative voltage is applied to the gate line disabling the conductivity and enabling the photodiodes to generate and store the charges caused by the incident photons. By switching the voltage to a positive value, the conductivity is accomplished and the charge is transported along the data line to external electronics. The signal readout shows an exponential behavior with the time constant

$$\tau_{pix} = R_{TFT_ON} \cdot C_{pd},$$

where R_{TFT_ON} is the on-resistance of the TFT. This time constant is related to the maximum frame rate theoretically possible. For N_G gate lines, the maximum frame rate that obtains is

$$FrameRate_{max} = \frac{1}{\tau_{pix} \cdot N_G \cdot N_\tau},$$

where $\tau_{pix} \cdot N_\tau$ corresponds to the time waited before readout is said to be finished. Due to the fact that each pixel incorporates a photodiode sensor as well as a TFT switch, the sensitive area is not directly given by the pixel pitch but by the so-called fill factor. In Table 2.2 the most important parameters are listed up for the TFTs used in the PortalVision™ aS500.

Table 2.1 Key parameters for the a-Si:H photodiode used in the PortalVision™ aS500.

Parameter	Value	Reference
Photodiode type	p-i-n	(Varian)
Quantum efficiency η_{diode}	80% (at 550 nm)	(Antonuk <i>et al.</i> 1998)
Sensor capacity C_{pd}	8-11 pF (9.4 typical)	(Varian)
Bias voltage V_{bias}	5 V	(Varian)
Pixel charge capacity Q_{pd}	47 pC	

Table 2.2 Key parameters for the *a-Si:H* TFT used in the PortalVision™ aS500.

Parameter	Value	Reference
On-resistance R_{TFT_ON}	0.7 M Ω	(Varian)
Time constant τ_{pix}	6.6 μ s typical	(Varian)
Maximum frame rate	40 frames per second	

2.5 INDIRECT DETECTION OF HIGH-ENERGY PHOTONS

In order to convert high-energy photons to visible photons – which then are able to get sensed by the photodiode – the EPID makes use of the so-called indirect detection method. The main principle lies in the use of a metal plate/phosphor screen combination, as was already employed for video-based EPIDs (Boyer *et al.* 1992). The PortalVision™ aS500 encompasses a 1 mm copper plate bonded to a 0.5 mm thick gadolinium oxysulfide ($Gd_2O_2S:Tb$) phosphor layer. In indirect detection, high-energy photons are first converted to high-energy electrons (and positrons) by the metal plate, which then deposit some amount of energy within the phosphor. The phosphor translates the energy deposition into optical photons, which then are transported through the phosphor and are finally sensed by the photodiode. In Figure 2.3 the principle of indirect detection is shown schematically.

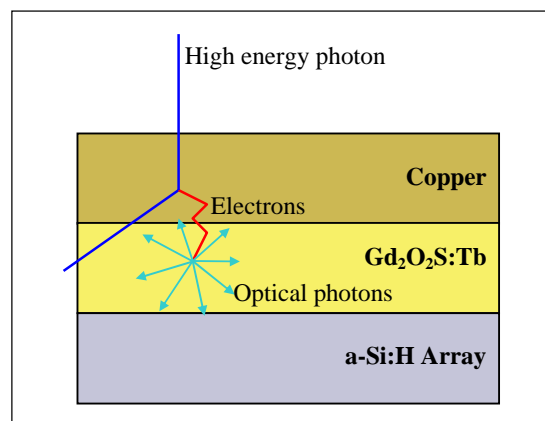


Figure 2.3 The main principle of indirect detection lies in the conversion of high-energy photons into optical photons by the use of a phosphor screen. That is why the EPID is built from a 0.5 mm thick $Gd_2O_2S:Tb$. In order to improve the detection efficiency a 1 mm thick copper plate is used.

The phosphor material used for the EPID is $\text{Gd}_2\text{O}_2\text{S:Tb}$, which is a rather common scintillating material (e.g. in video-based EPIDs) for portal imaging purposes. As an inorganic scintillator, $\text{Gd}_2\text{O}_2\text{S:Tb}$ exhibits luminescence, where it reemits optical photons after absorption of energy. The number of released photons in the phosphor is proportional to the energy deposited in the phosphor layer (Leo 1994).

2.6 LINEARITY OF THE SIGNAL

A detailed analysis of the signal formation using Monte Carlo simulations is given in Chapter 3. At this point, only the basic relationships (linearity, dose rate independence) between the radiation delivered by the linac and the corresponding signal of the EPID are presented.

The output of the linac is given by the dose D_{ij} delivered to a reference system (water phantom). The raw signal P_{ij}^* of the EPID at a pixel i,j is then related to the linac output by

$$P_{ij}^* = s_{ij} \cdot G(D_{ij}) + o_{ij},$$

where s_{ij} denotes the relative sensitivity of the pixel i,j and o_{ij} corresponds to the offset of the pixel i,j . The function G is the dose response of the detector.

The offset is measured by a Dark Field (DF) image, which is an image acquired without any radiation ($D_{ij}^{DF} \equiv 0$). Without loss of generality, it can be assumed that the dose response is zero for this situation ($G(0) = 0$). Then the DF image is characterized by

$$DF_{ij} \equiv P_{ij}^{*DF} = s_{ij} \cdot G(D_{ij}^{DF}) + o_{ij} = o_{ij}.$$

The relative sensitivities of the EPID's pixels are corrected by the use of a Flood Field (FF) image. The FF image corresponds to a measurement of a flat (uniform) field already corrected for offset:

$$FF_{ij} \equiv P_{ij}^{*FF} - o_{ij} = s_{ij} \cdot G(D_{ij}^{FF})$$

The standard correction as implemented in the PortalVision™ aS500 acquisition software is defined as

$$P_{ij} \equiv \frac{P_{ij}^* - DF_{ij}}{FF_{ij}} \cdot \langle FF_{ij} \rangle,$$

where $\langle FF_{ij} \rangle$ is the mean value of the FF image. With this correction scheme, the application of a FF leads to a constant pixel value:

$$P_{ij}^{FF} \equiv \frac{P_{ij}^{*FF} - DF_{ij}}{FF_{ij}} \cdot \langle FF_{ij} \rangle = \langle FF_{ij} \rangle = const.$$

But in practice, a completely uniform field can not be generated since the flattening filter leads to off-axis softening (Mohan and Chui 1985). Thus, the standard correction corrects for both, the non-uniformity of the FF and the individual pixel sensitivities.

Supposing a field which is uniform at least within a region of interest (ROI) around the central axis:

$$D_{ij}^{UF} = D^{UF} = const. \quad \forall (i, j) \in ROI$$

Building the average of the offset corrected pixel values over this ROI leads to

$$\frac{1}{m \cdot n} \cdot \sum_{i,j}^{m,n} (P_{ij}^{*UF} - DF_{ij}) = \frac{1}{m \cdot n} \cdot \sum_{i,j}^{m,n} s_{ij} \cdot G(D_{ij}^{UF}) = \langle s_{ij} \rangle \cdot G(D^{UF}) = G(D^{UF})$$

In the last step the assumption $\langle s_{ij} \rangle = 1$ was made which is allowed due to the relative nature of the sensitivity. The average of the standard corrected pixel values of the ROI leads to

$$\frac{1}{mn} \cdot \sum_{i,j}^{m,n} \left(\frac{P_{ij}^{*UF} - DF_{ij}}{FF_{ij}} \cdot \langle FF_{ij} \rangle \right) = \frac{\langle FF_{ij} \rangle}{m \cdot n} \cdot \sum_{i,j}^{m,n} \frac{s_{ij} \cdot G(D_{ij}^{UF})}{s_{ij} \cdot G(D_{ij}^{FF})} = \langle FF_{ij} \rangle \cdot \left\langle \frac{1}{G(D_{ij}^{FF})} \right\rangle_{mn} \cdot G(D^{UF})$$

On the basis of these equations, the dose response G can be determined by applying a uniform field D^{UF} and measuring the corresponding pixel values P_{ij}^{UF} .

For this purpose, the portal dose D^{UF} has to be modified. This can easily be performed by varying the number of MUs delivered by the linac. The image acquisition of the EPID is performed such that a certain number of frames N_f will be acquired continuously. N_f is mainly determined by the acquisition parameters determining the timing of the acquisition (i.e. frame rate) and the time t needed to deliver the number of MUs

$$t = \frac{D_{ij}^{UF}}{Drate_{ij}^{UF}}$$

The resulting pixel signal $\langle P_{ij}^{UF} \rangle$ of the EPID is the average over all frames:

$$\langle P_{ij}^{UF} \rangle = \frac{1}{N_f} \cdot \sum_{t=0}^{N_f} P_{ij}^{UF}(t).$$

Thus, in order to measure the dose response G , the frame averaged pixel signal $\langle P_{ij}^{UF} \rangle$ needs to be multiplied by the number of frames N_f .

In Figure 2.4 the results are presented for a 6 MV photon beam with a field size of $10 \times 10 \text{ cm}^2$ (at isocenter distance) operating with a dose rate of 200 MU/min. The ROI was 9×9 pixels around central axis, and the EPID was located at an SDD of 140 cm. The excellent linear relationship between the pixel signal P_{ij}^{UF} and the dose (in MU) delivered by the linac is clearly visible ($R^2=0.9999991$). In this experiment, the dose per frame is always the same. As a consequence, the increase of the pixel signal P_{ij}^{UF} is mainly due to the linear growth of N_f with the increased dose delivered demonstrating that the frame addition process works correctly. Note that this is non-trivial, since any likely memory effects would turn up in this experiment.

In order to investigate the dose response, the dose per frame has to be changed. This is accomplished either by modifying the frame rate or the dose rate. One method to change the dose per frame is based on the variation of the SDD . According to the inverse square law, the dose D delivered to the EPID is

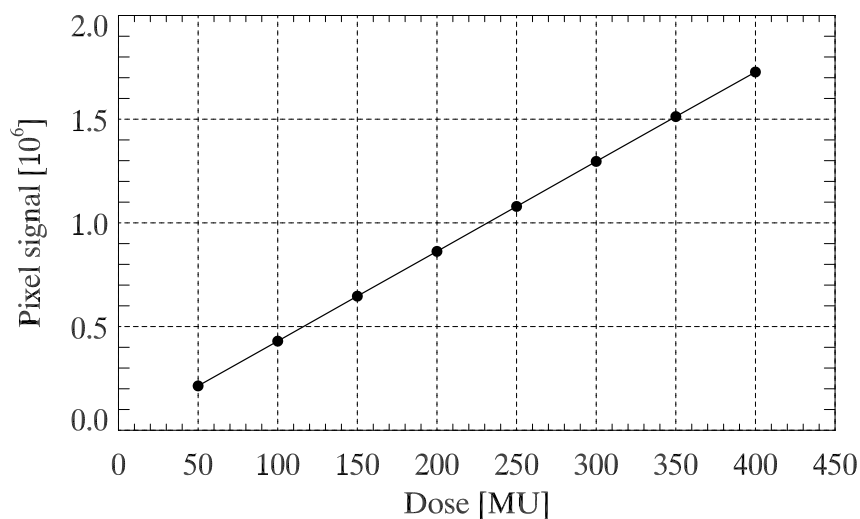


Figure 2.4 Pixel signal (product of the frame averaged pixel signal and the corresponding number of frames) as a function of the dose delivered by the linac. The linear relationship demonstrates that frame averaging works correctly.

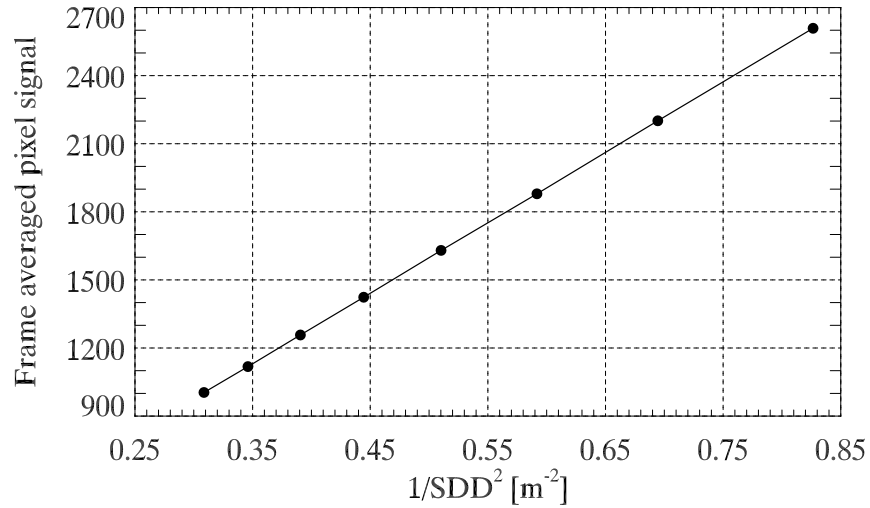


Figure 2.5 The linear relationship between the frame averaged pixel signal and $1/SDD^2$ reveals the linear dose response of the EPID. For this experiment, the dose is changed by varying the EPID's position. According to the inverse square law, the dose is proportional to $1/SDD^2$.

given by

$$D = D_0 \cdot \left(\frac{SDD_0}{SDD} \right)^2$$

where D_0 is the dose at the isocenter distance SDD_0 . Again a 6 MV photon beam with a field size of $10 \times 10 \text{ cm}^2$ (at isocenter distance) is chosen with the linac's repetition rate of 200 MU/min. For each SDD , 100 MU are delivered leading to a constant number of frames N_f . As a result, the decrease of the pixel signal with increasing SDD is only due to a decrease of the dose per frame. Figure 2.5 shows the highly linear ($R^2=0.99995$) relationship between the frame averaged pixel signal and $1/SDD^2$. Note that for this experiment the dose rate changes proportionally to dose, but due to the dose rate independence of the EPID (see below), this experiment reveals the linearity of the dose (and not dose rate) response.

Finally, the dose per frame can be changed by modification of the frame rate of the image acquisition. In this case, the linac provides a constant output (100 MU delivered with different dose rates) and the EPID manages the image acquisition such that different frame times occur. In Figure 2.6 the frame averaged pixel signal is given as function of dose per frame. The dose per frame is determined by the total number of MUs delivered by the linac, the SDD

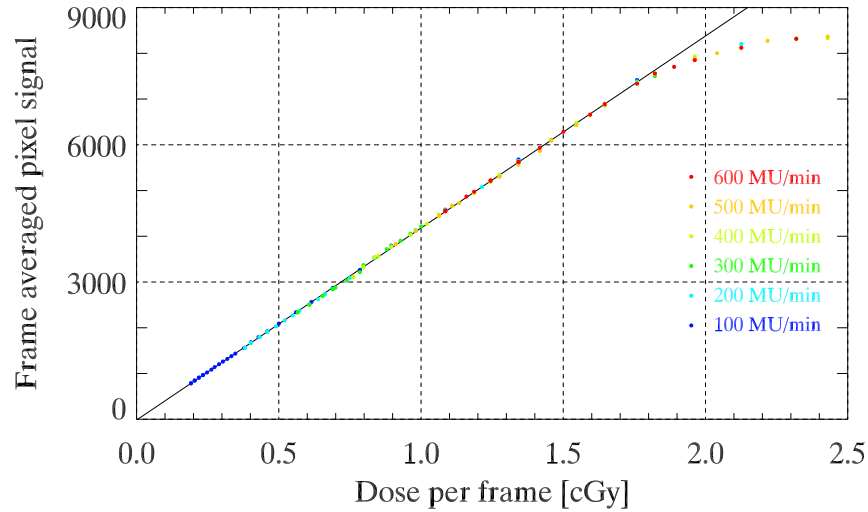


Figure 2.6 Linear dose response relationship for the PortalVision™ aS500. The figure shows the frame averaged pixel signal as a function of the dose per frame. The dose per frame has been modified by acquisition changes and delivering the dose at different dose rates. The linearity between the signal and the dose is clearly visible. In addition, the signal is independent on dose rate.

(inverse-square law), and the number of frames N_f acquired by the EPID. The conversion from MU to cGy is accomplished by the MU calibration of the specific linac, which says that 1 MU corresponds to 1 cGy under reference conditions ($10 \times 10 \text{ cm}^2$ field, 10 cm water depth, $SDD=90 \text{ cm}$). The figure reveals the highly linear relationship ($R^2=0.95$) between the frame averaged pixel signal and the dose per frame until about 1.7 cGy. For higher doses saturation occurs in the photodiode. In addition, the figure demonstrates the independence of the pixel signal of dose rate. This is totally in contrast to the SLIC-EPID, where the pixel signal depends inherently on dose rate (Essers *et al.* 1995).

2.7 STABILITY OF THE SIGNAL

In order to use an EPID for dosimetric applications (such as the measurement of a portal dose image as is shown in Chapter 5), the stability of the EPID's signal has to be ensured. For this purpose, the time dependence of the pixel signal needs to be investigated.

Long-term stability is examined by measuring the day-to-day variations of the pixel signal during a period of 54 days. Each measurement consists of the acquisition of a portal image while applying always the same dose. Typically about 300 frames are averaged for a dose of 100 MU delivered with a repetition

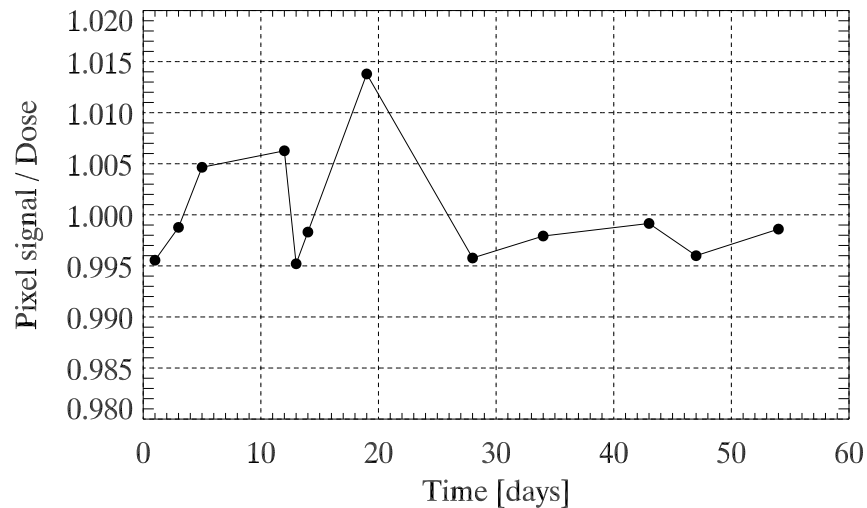


Figure 2.7 Long-term stability is analyzed by acquiring always the same dose at different days. The small variations of the ratio between the pixel signal and the dose – measured by an ionization chamber – demonstrates the highly stable performance of the EPID’s signal.

rate of 200 MU/min. In addition to the portal image acquisition, ionization chamber measurements are performed to assess the linac’s output variations (typically in the order of 1%). Hence, in order to quantify the long-term stability of the EPID itself, each portal image has been corrected for the linac’s output variation. The ratio between the pixel signal and the dose as a function of time is given in Figure 2.7. The normalization is such that the mean of this ratio is equal to 1. Only small day-to-day variations of 0.6% (1 SD) exist, indicating that the EPID’s signal is highly stable. This result backs the motivation to use amorphous silicon material because of its radiation resistant performance (Antonuk *et al.* 1992).

One of the most important impediments for the SLIC EPID is its tremendous memory effect (Curtin *et al.* 1999, Keller *et al.* 2000). As has been shown by Curtin-Savard *et al.* (1999), the short-term stability of the SLIC EPID is a key feature which leads to severe problems for the dose measurement of intensity modulated fields. In this thesis, the investigation on short-term stability for the a-Si:H based EPID is carried out by acquiring a portal image every 60 s during 1 h. An image consists of the average of all frames acquired during the time needed to achieve 50 MU at a linac output rate of 200 MU/min. Figure 2.8 shows that with a standard deviation of 0.1% the short-term stability of the EPID is fulfilled.

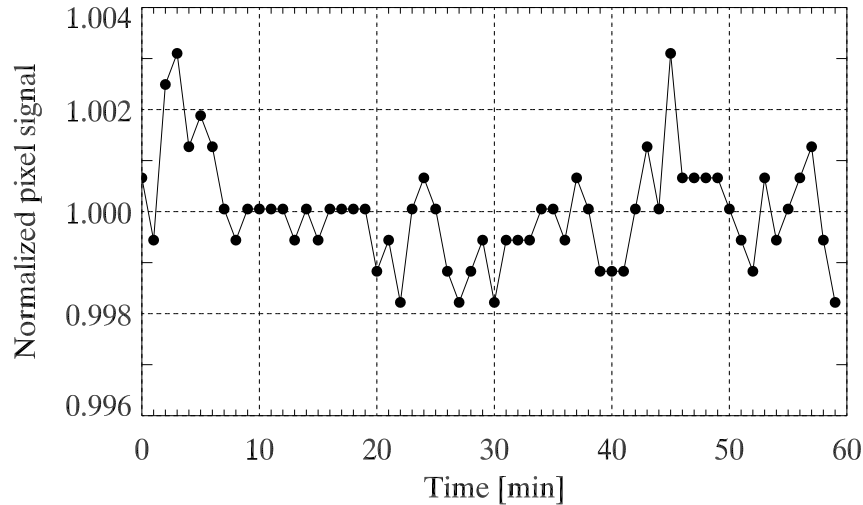


Figure 2.8 Short-term stability is investigated by applying a certain dose (50 MU) at different times. The figure shows that only small variations of 0.1% (1 SD) turn up which is a prerequisite for the measurement of portal dose distributions for dynamically applied fields.

2.8 IMPACT OF DETECTOR COMPONENTS

As has been indicated previously, the detection of high-energy photons relies on the principle of indirect detection. With the intention to improve the understanding of the influence of the different detector components of the

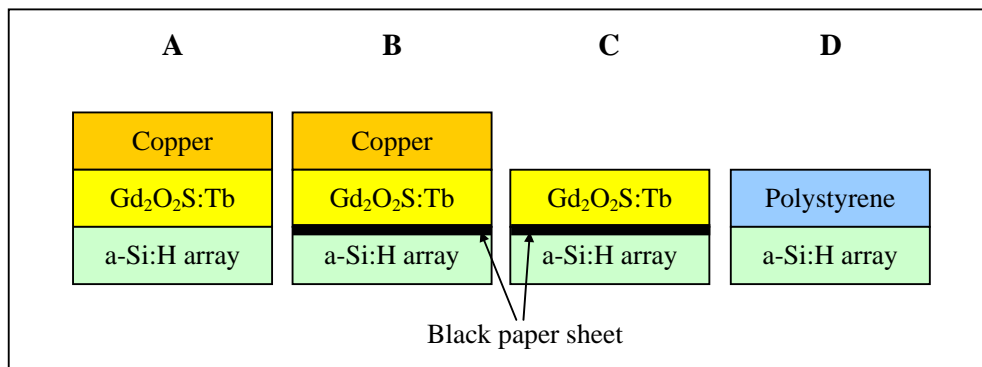


Figure 2.9 Four detector configurations are constructed to investigate the signal contribution due to direct detection. Configuration A represents the original PortalVision™ aS500, for which the signal is formed indirectly by converting high-energy photons into visible (optical) photons by the use of a phosphor screen. In configurations B and C, the optical photons are prevented to generate some signal by the implementation of a black paper sheet between the phosphor screen and the photodiode array. To obtain detailed information about the different components, the copper plate is removed in configuration C. Finally, in configuration D both the copper plate and the phosphor screen are missing. In this case, the signal is formed by charged particles released in the polystyrene plate.

PortalVision™ aS500 on the pixel signal, several detector configurations are generated (Figure 2.9).

The detector configuration A represents the original configuration of the PortalVision™ aS500. This EPID consists basically of a copper plate bonded to a phosphor layer. The copper plate improves the efficiency of the detection of high-energy photons and acts as a filter for electrons scattered from the patient. More details on this is presented in Chapter 3 by using Monte Carlo simulations. At the moment, to study the influence of the signal occurring due to direct

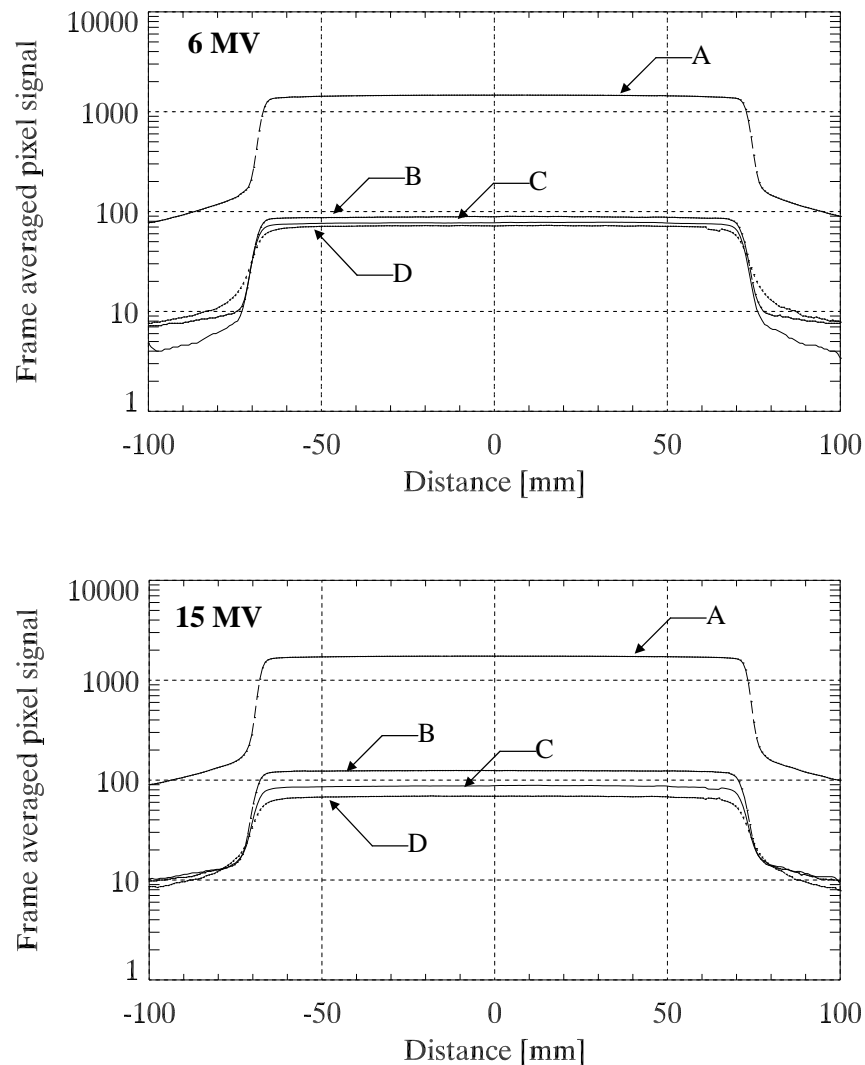


Figure 2.10 The impact of the different detector components for 6 and 15 MV on the pixel signal is investigated by four different detector configurations (cf. Figure 2.10). The figure shows profiles for $10 \times 10 \text{ cm}^2$ fields and an SDD of 140 cm. The frame averaged pixel signal of the original detector (A) is decreased by a factor of about 15, if the detection of optical photons is prevented (B, C, and D).

detection of high-energy particles in the photodiode, a thin black paper sheet underneath the phosphor layer is implemented in configuration B. The black paper sheet deters visible photons to reach the photodiode. To obtain more detailed information about the signal contribution due to direct detection, configurations C and D are generated. Configuration C differs from configuration B by the removal of the copper plate, while in configuration D both the copper plate and the phosphor layer are missing. However, configuration D is supplemented by additional polystyrene plates in order to resemble the situation of a water detection system. In this case, the signal contribution is governed by charged particles released in the polystyrene material.

Note that there are other components in the PortalVision™ aS500 system such as some low-density materials forming a ‘sandwich’ structure. Although these components are not illustrated in Figure 2.9, they are not removed for the experiments.

Figure 2.10 shows profiles of the frame averaged pixel signal obtained for different detector configurations. For all situations, a $10 \times 10 \text{ cm}^2$ field is applied leading to a lateral expansion of 140 mm at an *SDD* of 140 cm. The figure demonstrates that the signal of the original detector configuration is decreased by a factor of about 15 if the detection of optical photons is prevented. In other words, the signal contribution due to direct detection is in the order of 7%. The results for configurations C and D reveal that about 1-2% of the signal is caused

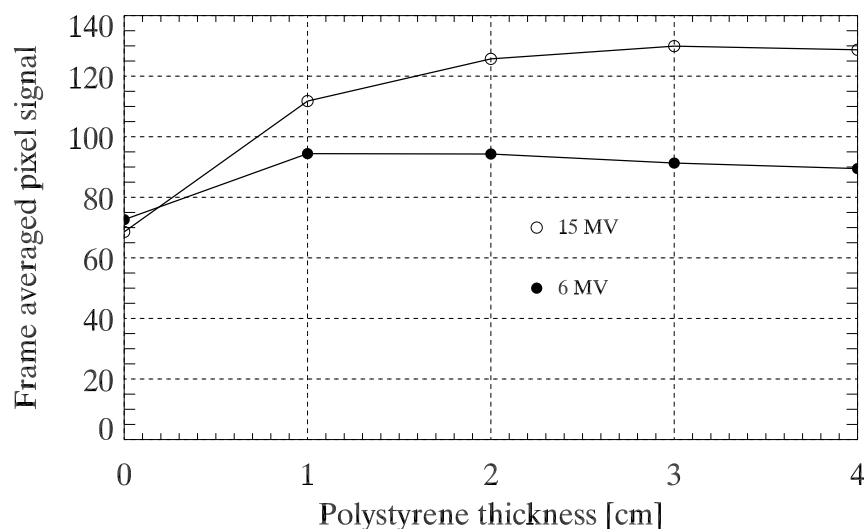


Figure 2.11 Frame averaged pixel signal as a function of the polystyrene thickness for the detector configuration D. In this configuration, the signal is formed mainly by charged particles released in the polystyrene and other detector materials, respectively. Thus, the dependence on the polystyrene thickness reflects the buildup-effect: Whereas for 6 MV the pixel signal reaches a maximum for a thickness of about 1.5 cm, the maximum for 15 MV occurs for a thickness of about 3 cm.

by charged particles released in the copper plate and about 1% is based on the release of charged particles from the phosphor layer.

The effect of direct detection in configuration D is further illustrated in Figure 2.11. The frame averaged pixel signal is given as a function of the polystyrene thickness reflecting the buildup-effect. For 6 MV, a thickness of 1.5 cm is needed to achieve highest signal, while for 15 MV about 3 cm is required.

3

Physical Characteristics of the EPID

3.1 OVERVIEW

Originally, EPIDs had been developed for patient setup purposes. The EPID's design, therefore, was optimized for highest image quality. This is why the EPID is equipped with a metal plate located above the phosphor layer. As has been presumed by Chang *et al.* (2000), the a-Si:H based EPID is a promising alternative to other EPIDs for dosimetric verification purposes. In his thesis, Pasma (1999) discussed briefly the potential of the a-Si:H EPID for portal dosimetry and suggested that a detailed study – such as a Monte Carlo model – might be useful to understand and to improve its dosimetric properties.

3.2 QUANTUM ACCOUNTING DIAGRAM ANALYSIS

In order to characterize the physical properties of the EPID, the quantum accounting diagram (QAD) analysis theory is used. In this theory, a linear and shift-invariant imaging system is described as a cascade of multiple stages (Cunningham *et al.* 1994, Cunningham and Shaw 1999). The main stages are: (1) quantum gain, where the number of quanta is changed according to an amplification or a decrease (e.g., detection of X-rays) and (2) stochastic spread, where the number of quanta is preserved but quanta are smeared at random. In QAD analysis, the number of quanta entering a stage i is connected to the number of quanta leaving the previous stage $i-1$.

Gain stages are described by an average gain factor and gain Poisson excess. For a stage i being composed of a gain only, the mean fluence $\bar{\phi}_i$ is given by the average fluence gain \bar{g}_i and the mean fluence $\bar{\phi}_{i-1}$ entering the stage i . The Poisson excess ε_{g_i} associated with \bar{g}_i is given by the variance $\sigma_{g_i}^2$ in this gain. Thus, for a gain process the following equations can be derived:

$$\bar{\phi}_i = \bar{g}_i \cdot \bar{\phi}_{i-1} \quad \text{and} \quad \varepsilon_{g_i} = \frac{\sigma_{g_i}^2}{\bar{g}_i} - 1.$$

For a binary selection process – such as an interaction probability – the binomial theorem leads to the Poisson excess $\varepsilon_{g_i} = -\overline{g_i}$.

Stochastic spread is characterized by the modulation transfer function (MTF) of the stage. The MTF is obtained by the modulus of the Fourier transform of the point-spread function (PSF). For a stage i describing a spreading process, the mean fluence and the Poisson excess are

$$\overline{\phi_i} = \overline{\phi_{i-1}} \quad \text{and} \quad \varepsilon_{g_i} = -1.$$

Image quality is best described by the detective quantum efficiency (DQE). As was shown by Cunningham and Shaw (1999), the DQE can be expressed as

$$DQE(f) = \frac{1}{1 + \sum_{i=1}^M \frac{1 + \varepsilon_{g_i} |T_i(f)|^2}{P_i(f)}}$$

where f is the spatial frequency. $P_i(f)$ is the product gain and squared MTF $T_i(f)$ up to the i th stage, also known as the quantum accounting diagram *QAD*:

$$P_i(f) = QAD(i, f) = \prod_{j=1}^i \overline{g_j} |T_j(f)|^2.$$

The stage with the lowest $P_i(f)$ is called quantum sink and corresponds to the stage most dominant for noise.

3.3 SIGNAL FORMING STAGES

To characterize the EPID by applying the QAD analysis, the signal formation has been divided into eight stages. As shown in Figure 3.1, the stages are: (0) incident x-ray photon, (1) detection of x-ray photon, (2) spread of high-energy particles within the detector, (3) production of optical photons, (4) spread of optical photons within the phosphor layer, (5) escape of optical photons from the phosphor screen, (6) collection of optical photons by the photodiode array, (7) detection of optical photons by the photodiode.

In the first stage 1, the energy deposition within the phosphor layer is seen as an equivalent expression for the detection of the incident x-ray photon. It is assumed, that only photons lead to a signal if some amount of energy is deposited in the phosphor. In this thesis, the Monte Carlo (MC) method is used to determine the energy deposition and the corresponding fluctuations which are a

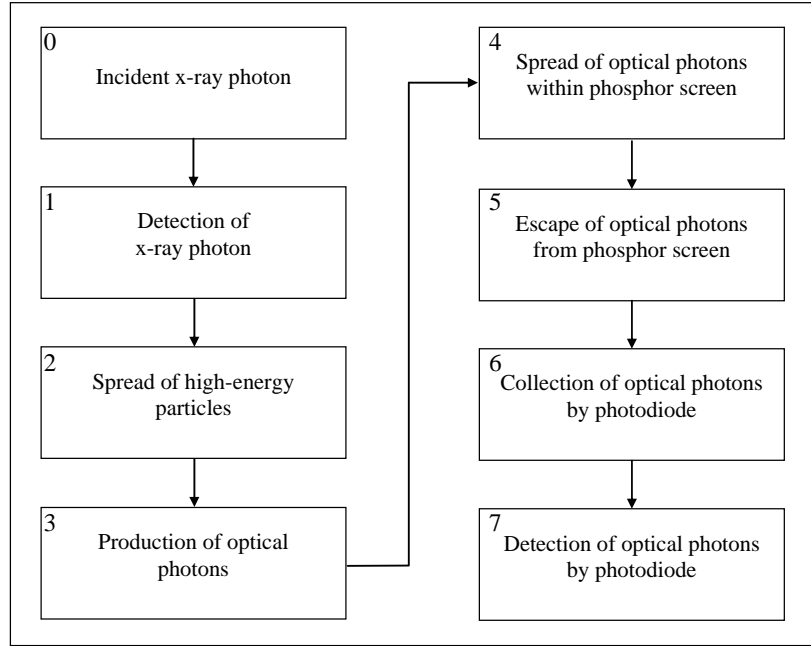


Figure 3.1 The eight stages represent the signal formation processes. Based on these stages, the QAD analysis is used to characterize the physical properties of the EPID.

consequence of the stochastic nature of energy deposition. In addition, MC simulations are used to investigate the spread of high-energy particles by computing the MTF of the energy deposition in the phosphor layer (stage 2).

The production of optical photons (stage 3) is related to the amount of energy deposited in the phosphor layer. If $\overline{E_{ab}}$ is the mean energy absorbed in the phosphor layer per detected x-ray photon (i.e. the x-ray photon deposits some energy in the phosphor), the mean number of optical photons produced per detected x-ray photon is

$$\overline{g_3} = \frac{\eta \cdot \overline{E_{ab}}}{E_{opt}},$$

where η is the energy conversion efficiency and $\overline{E_{opt}}$ the mean energy of the visible photon. For $\text{Gd}_2\text{O}_2\text{S:Tb}$, η is 0.15 and $\overline{E_{opt}}$ is 2.3 eV (Yaffe and Rowlands 1997).

With the purpose of investigating the spread and the escape of optical photons (stages 4 and 5), a model of the transport of optical photons is applied. A specific MC code is developed to simulate the light propagation through the phosphor layer. For stage 6, the collection of optical photons by the photodiode array is

given by the fill factor of the a-Si:H array. For the PortalVision™ aS500, $\overline{g_6}$ is 0.84 (manufacturer). Stage 7 addresses the detection of optical photons by the photodiode.

3.4 MONTE CARLO SIMULATIONS

In radiotherapy, the use of Monte Carlo (MC) methods for the simulation of the transport of high-energy particles through matter has a long tradition. As a consequence of the increase of computer power during the last decade, MC simulations are widely used today for different applications in medical physics such as treatment planning, beammodelling, or physical characterization of radiation detectors. In particular its accuracy of dealing with the challenging radiation transport between low and high density structures makes the MC method an accurate tool for clinical treatment planning (Mohan 1997).

The basic principle of the MC method has been reported in the literature (Andreo 1991). In the following, a short description of the specific MC code GEANT (CERN 1995) will be given by illustrating the transport of high-energy photons and their secondary particles released within a homogeneous medium. Initially the photon is provided with variables describing the initial state such as position, energy, and momentum. According to the probability of an interaction (given by the corresponding cross sections), GEANT simulates the transport of a particle by sampling a mean free path and an interaction type of the photon, which depend on the energy and the medium. After the interaction, the secondary particles (photons, electrons, and positrons) are simulated.

The main interaction types of photons with matter are Rayleigh scattering, photoelectric effect, Compton scattering, and pair production. GEANT allows for all these processes by the use of corresponding cross section data. For higher efficiency, the simulation of electrons and positrons is performed by applying the Molière multiple scattering theory for elastic collisions. In order to deal with inelastic collisions, GEANT utilizes the Møller scattering theory and the Bhabha scattering theory for electron-electron collisions and positron-electron collisions, respectively. Bremsstrahlung is taken into account by applying the cross section data from Seltzer and Berger. Finally, the annihilation process is based on Heitler's formula (CERN 1995).

3.5 ENERGY DEPOSITION IN THE PHOSPHOR LAYER

In order to study the energy deposition in the phosphor layer, the EPID's main components were implemented into a GEANT based routine, as shown in Figure 3.2. The routine calculates the energy deposited within the phosphor for a pencil beam intersecting the detector.

Let E' be the energy deposited within the phosphor due to an incident monenergetic pencil beam with energy E . The stochastic nature of energy deposition implies that E' is not unique but occupies a distribution $A(E, E')$ known as the absorbed energy distribution (AED) (Jaffray *et al.* 1997). The AED is also known as the pulse-height spectra of the energy deposition. For an incident energy of 1 MeV, Figure 3.3 shows the AED for different detector configurations. Note, that for these simulations a simplified geometry was applied such that the detector consisted only of a copper plate and a phosphor screen ($\text{Gd}_2\text{O}_2\text{S:Tb}$). Although many thicknesses of these materials were investigated, the results shown here are restricted to typical thicknesses as employed in EPIDs (cf. Chapter 2). The results show an increase of deposited energy with increasing thickness of the copper plate. Increasing the thickness of the phosphor layer changes the form of the AED, particularly above 0.6 MeV. While for a 1 mm thick phosphor screen it is possible to deposit 1 MeV, this is impossible for a thickness of 0.5 mm. Obviously, the released electrons have too high energies to get absorbed in 0.5 mm thick $\text{Gd}_2\text{O}_2\text{S:Tb}$. Furthermore, for the

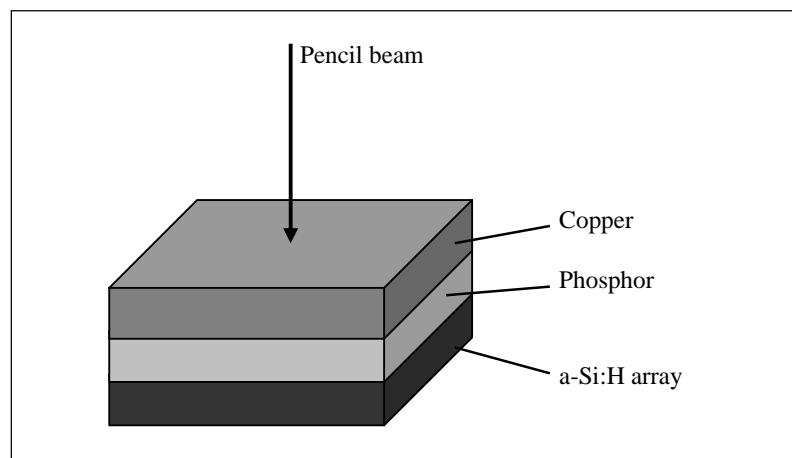


Figure 3.2 The main components of the EPID are implemented in the MC code for the simulations of the energy deposition within the phosphor layer.

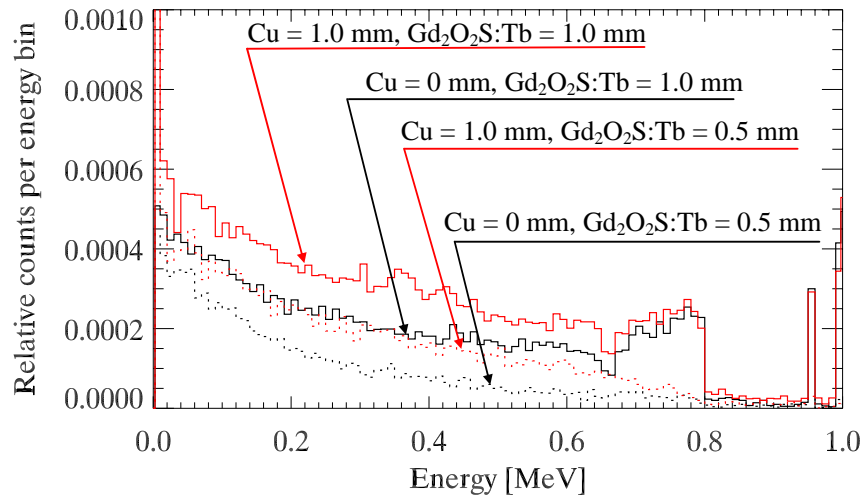


Figure 3.3 Simulated absorbed energy distribution (AED) for a 1 MeV photon beam incident on different detector configurations. For 1 MeV, the copper plate increases the energy deposited in the phosphor layer but the shape of the AED is not affected very much. The thickness of the phosphor layer has an enormous impact on the shape of the AED as well as on the amount of energy deposited in the layer.

1 mm thick phosphor layer a peak at about 950 keV is apparent. This peak is caused by fluorescent radiation occurring due to the K-edge of Gd (50.2 keV).

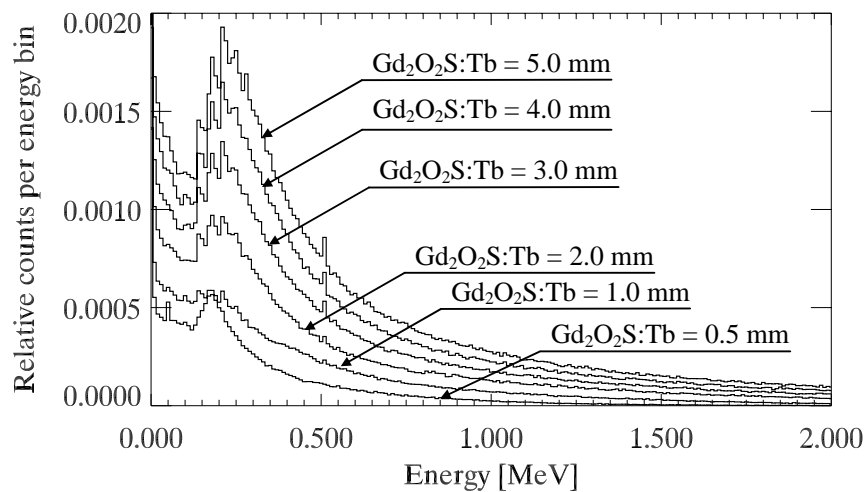


Figure 3.4 AED for a 6 MV photon beam for different phosphor layer thicknesses. In all simulations, the thickness of the copper plate is 1 mm. The thicker the phosphor screen, the more energy is deposited in the phosphor layer.

In Figure 3.4 the AED for a polyenergetic (6 MV) pencil beam is shown for a copper plate thickness of 1 mm and different $\text{Gd}_2\text{O}_2\text{S:Tb}$ thicknesses. The 6 MV spectrum was taken from (Fix *et al.* 2001 a). As before, these simulations are related to the simplified geometry. Unsurprisingly, the probability per incident photon and per 10 keV energy bin increases with the thickness of the phosphor layer. The peak at absorbed energies of about 300 keV is dictated by the incident energy spectrum and is more apparent for thicker phosphor screens due to increased detection probability.

The number N of photons, which deposit some amount of energy within the phosphor, is given by the integral of the AED

$$N(E) = \int_0^E A(E, E') dE'$$

While N is proportional to the number of incident photons N_0 , the quantum absorption efficiency (QAE) is defined as the fraction of the number of incident photons N_0 to the number of photons, which contribute to the signal (by depositing some amount of energy within the phosphor):

$$QAE(E) = \frac{N(E)}{N_0} = \frac{\int_0^E A(E, E') dE'}{N_0}$$

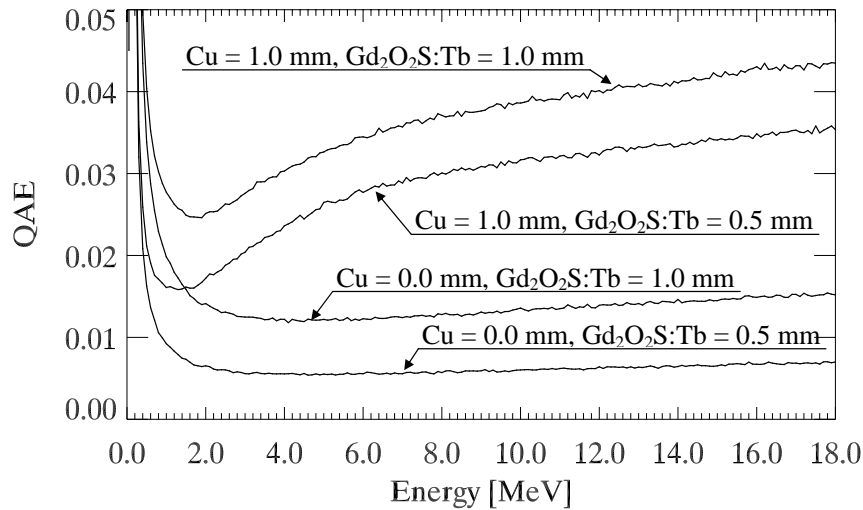


Figure 3.5 The number of pulses (QAE) per incident photon as a function of the incident energy. A pulse occurs if an incident photon interacts with the detector's components such that some amount of energy is deposited in the phosphor screen. Particularly at high energies, the impact of the copper plate is clearly visible: the thicker the copper plate, the more pulses per incident photon.

Table 3.1 Quantum absorption efficiency (QAE) and mean energy deposited in the phosphor for different phosphor layer thicknesses obtained from MC simulations of a 6 MV and a 15 MV photon beam, respectively. The thickness of the copper plate is always 1 mm.

Phosphor layer thickness [mm]	QAE (6 MV)	mean energy deposited (6 MV) [MeV]	QAE (15 MV)	mean energy deposited (15 MV) [MeV]
0.5	0.0211	0.29	0.0222	0.37
1.0	0.0337	0.44	0.0303	0.67
2.0	0.0560	0.58	0.0451	1.05
3.0	0.0774	0.64	0.0593	1.30
4.0	0.0977	0.69	0.0733	1.48
5.0	0.1169	0.72	0.0868	1.62

The QAE corresponds to the number of pulses per incident photon. From the values in Table 3.1 it is apparent that the QAE is highest for the thickest phosphor layer considered in the simulations. Correspondingly, the mean energy deposited in the phosphor increases with increasing thickness. To evaluate the accuracy of the MC simulations performed in this thesis, the values for 6 MV can be compared to corresponding values in the literature. Using the MC code EGS4, Bissonette *et al.* (1997) investigated the energy distribution for a 1 mm thick copper plate bonded to a 1 mm thick Gd₂O₂S:Tb combination and resulted in a QAE of 0.0357 and a mean energy deposition of 0.44 MeV. In Figure 3.5, the QAE is shown as a function of incident photon energy. Particularly for high energies, the detector's efficiency increases with increasing thickness of the copper plate and that of the phosphor layer, respectively. The mean energy deposited in the phosphor layer per detected photon is defined as the ratio of the total energy deposition in the phosphor to the number of photons depositing some amount of energy in the phosphor:

$$\overline{E}_{ab}(E) = \frac{\int_0^E A(E, E') \cdot E' \cdot dE'}{N(E)}.$$

Similarly, the energy response of the detector is defined as:

$$\overline{E}_{resp}(E) = \frac{\int_0^E A(E, E') \cdot E' \cdot dE'}{N_0} = \frac{\overline{E}_{ab}(E) \cdot N(E)}{N_0} = \overline{E}_{ab}(E) \cdot QAE(E).$$

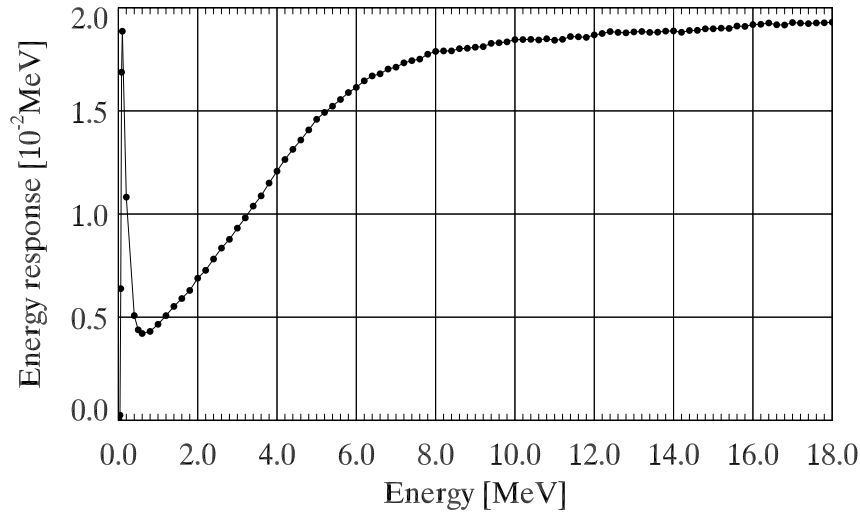


Figure 3.6 Energy response of the a-Si:H based EPID revealing the overresponse to low-energy photons. Between 1 and about 6 MeV, there is nearly a linear increase of the energy deposited in the phosphor layer and the energy of the incident photon. However, above 7 MeV saturation occurs.

$\overline{E_{resp}}(E)$ describes the mean energy deposited in the phosphor per incident photon with energy E . In Figure 3.6 the energy response of the a-Si:H EPID is shown. Note that for these simulations the exact geometry of the EPID is taken into account. The overresponse to low-energy photons is clearly visible. As will be demonstrated below, this peak is caused by the photo-electric effect. The figure also shows that above about 7 MeV the energy response curve is getting saturated. McCurdy *et al.* (2001) has recently published the same behavior and concluded that the detector does not have enough buildup to achieve electronic equilibrium in the phosphor layer at higher energies.

A more detailed analysis of the energy response is given in Figure 3.7, where the energy response is separated into several components. The notation of the components is such that $\overline{E_{resp}^{M,K}}$ represents the energy deposition within the phosphor screen by the particles of the type K , which were released due to at least one interaction only (except within $\text{Gd}_2\text{O}_2\text{S:Tb}$, of course) within the material M . To give an example, the component $\overline{E_{resp}^{Cu,e^-}}$ represents the energy deposition in the phosphor screen performed by electrons, which are released due to at least one interaction within the copper plate but did not have any interaction in the a-Si:H layer. In Table 3.2 all these components are listed up and explained. In MC simulations, the particle's history is pursued until it leaves the simulation space or falls below a user-defined cutoff energy. In the latter case, the particle is stopped and its energy is deposited locally at this site. In GEANT the

corresponding parameters are $PCUT$ and $ECUT$ for photons and electrons, respectively. In all simulations performed in this thesis, $PCUT$ as well as $ECUT$ were set to 10 keV (the lowest possible for GEANT). From the definition of the components it can be derived:

$$\overline{E_{resp}} = \overline{E_{resp}^{Cu}} + \overline{E_{resp}^{Gd_2O_2S:Tb}} + \overline{E_{resp}^{Asi}} + \overline{E_{resp}^{CuAsi}} + \overline{E_{resp}^{Other}} .$$

where

$$\overline{E_{resp}^{Cu}} = \overline{E_{resp}^{Cu} e^-} + \overline{E_{resp}^{Cu} e^+} + \overline{E_{resp}^{Cu} CUT}$$

$$\overline{E_{resp}^{Gd_2O_2S:Tb}} = \overline{E_{resp}^{Gd_2O_2S:Tb} e^-} + \overline{E_{resp}^{Gd_2O_2S:Tb} e^+} + \overline{E_{resp}^{Gd_2O_2S:Tb} CUT}$$

$$\overline{E_{resp}^{Asi}} = \overline{E_{resp}^{Asi} e^-} + \overline{E_{resp}^{Asi} e^+} + \overline{E_{resp}^{Asi} CUT}$$

$$\overline{E_{resp}^{CuAsi}} = \overline{E_{resp}^{CuAsi} e^-} + \overline{E_{resp}^{CuAsi} e^+} + \overline{E_{resp}^{CuAsi} CUT}$$

$$\overline{E_{resp}^{Other}} = \overline{E_{resp}^{Other} e^-} + \overline{E_{resp}^{Other} e^+} + \overline{E_{resp}^{Other} CUT} .$$

Table 3.2 Components for the MC simulations of the energy response of the PortalVision™ aS500. For detailed information see text.

Component	Energy deposition due to	Particle interacts in
$\overline{E_{resp}^{Cu} e^-}$	e ⁻ interactions	Copper plate
$\overline{E_{resp}^{Cu} e^+}$	e ⁺ interactions	Copper plate
$\overline{E_{resp}^{Gd_2O_2S:Tb} e^-}$	e ⁻ interactions	Gd ₂ O ₂ S:Tb
$\overline{E_{resp}^{Gd_2O_2S:Tb} e^+}$	e ⁺ interactions	Gd ₂ O ₂ S:Tb
$\overline{E_{resp}^{Asi} e^-}$	e ⁻ interactions	a-Si:H
$\overline{E_{resp}^{Asi} e^+}$	e ⁺ interactions	a-Si:H
$\overline{E_{resp}^{CuAsi} e^-}$	e ⁻ interactions	Copper plate and a-Si:H
$\overline{E_{resp}^{CuAsi} e^+}$	e ⁺ interactions	Copper plate and a-Si:H
$\overline{E_{resp}^{Other} e^-}$	e ⁻ interactions	Other detector materials
$\overline{E_{resp}^{Other} e^+}$	e ⁺ interactions	Other detector materials

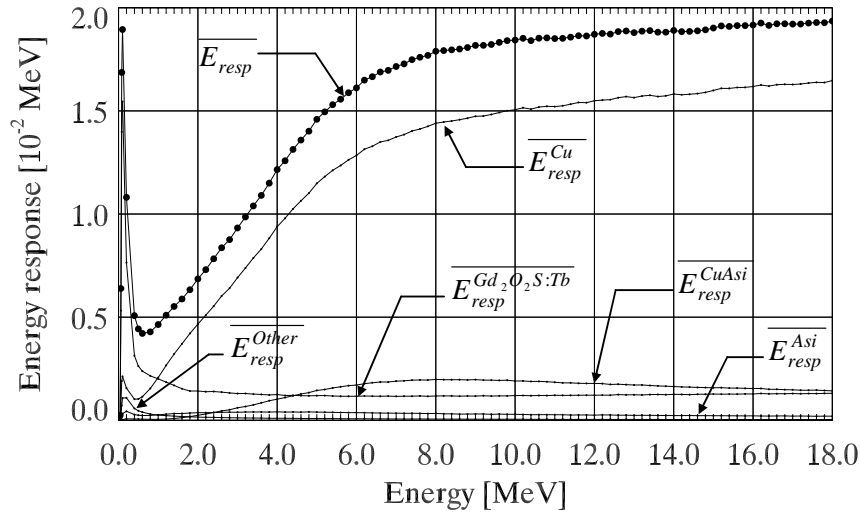


Figure 3.7 The MC method allows to simulate the energy deposition such that an analysis of different components responsible for the energy response of the EPID can be performed. The figure elucidates the impact of the metal plate on the energy deposited in the phosphor layer of the EPID. At low energies, the energy deposition is mainly due to electrons released in the phosphor screen only. Whereas this component decreases with increasing energy, the energy deposition is getting more and more dominated by electrons with at least one interaction within the copper plate. Furthermore, especially at higher energies, the positrons which interacted within the copper plate, contribute considerably to the energy deposition in the phosphor layer.

From Figures 3.7 and 3.8 an improved understanding of the physical characteristics of the EPID is obtained. Whereas at low energies – where the photo-electric effect is dominant – the energy response is caused mainly due to electrons interacting solely in the phosphor layer, the energy deposition for high energies is governed by electrons and positrons interacting in the copper plate. At low energies, the contribution of electrons interacting also in the copper plate is small which is due to the fact, that the electrons released in the copper plate have too small energies to leave the copper. However, above 1 MeV the main component is the energy deposition caused by electrons interacting in the copper plate. There is a linear increase of this contribution from 1 to about 6 MeV before it's getting saturated above 7 MeV. At high energies, the electrons released in the copper plate have enough energy to escape from the phosphor layer, which explains the rather constant behavior of this contribution.

Pair production is not an issue for low energies. However, at energies greater than 2 MeV, the contribution of positrons released from the copper plate is increasing more or less linearly with increasing photon energy. The contribution of positrons released directly in the phosphor screen is smaller because of the

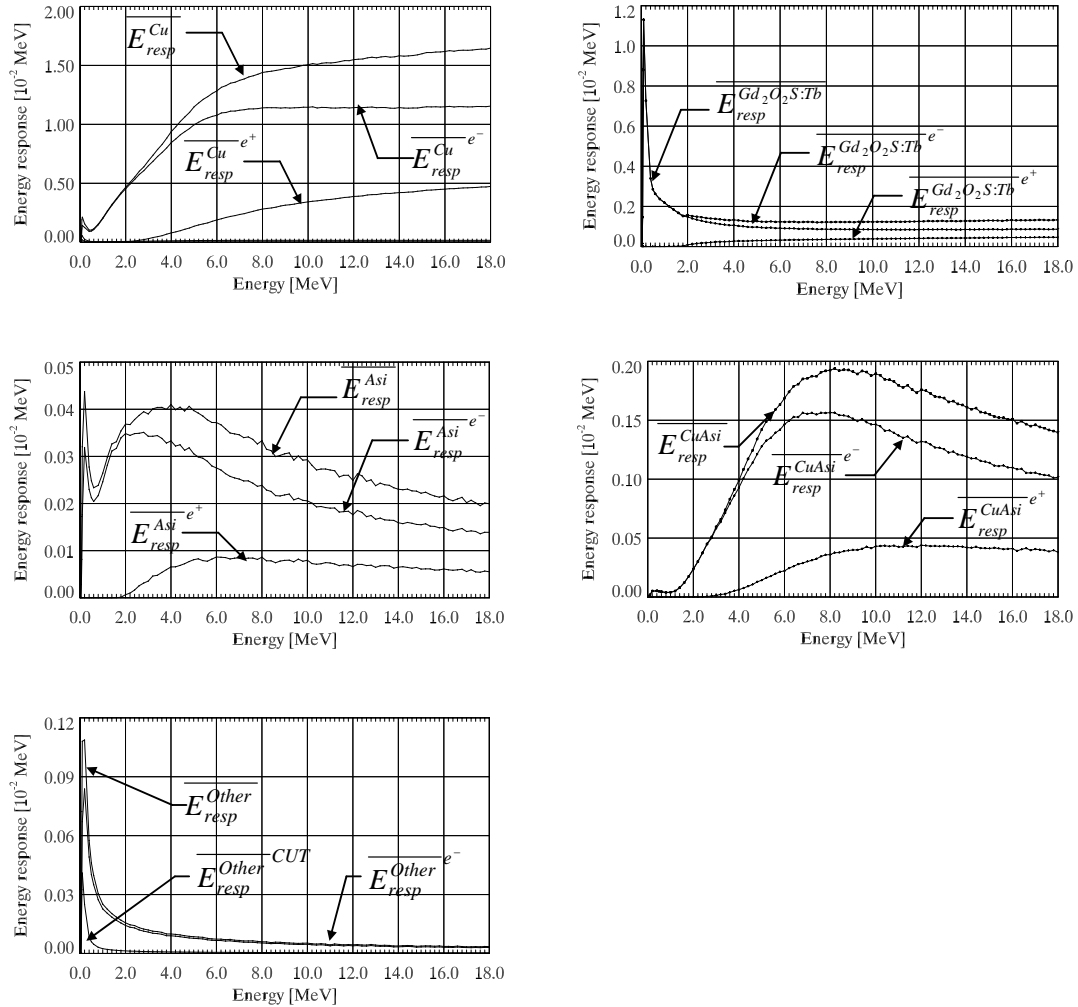


Figure 3.8 Details of Figure 3.7 revealing the fact, that above 1 MeV mainly the electrons from the copper plate are responsible for the energy deposition in the phosphor layer. Above 7 MeV, however, the electrons have too much energy to fully deposit all energy in the phosphor screen, which leads to a saturation of this component. Positrons are important for energies greater than 2 MeV. As for electrons, the positrons from the copper plate are most important. The contribution of particles (mainly electrons) interacting in the amorphous silicon material can not be neglected. Interestingly, the component CuAsi is more essential than the Asi component. For energies lower than 1 MeV, energy deposition is governed by particles (mainly electrons) interacting solely in the phosphor layer. In addition, the energy deposition due to particles falling below the energy cutoff of GEANT is only important for low energies.

same reason mentioned before for the contribution of electrons: the energy of the positrons is large enough to allow the positron to escape from the phosphor screen.

Figure 3.9 uncovers the impact of the different interaction types on the EPID's energy response. In these simulations, GEANT is caused to simulate only

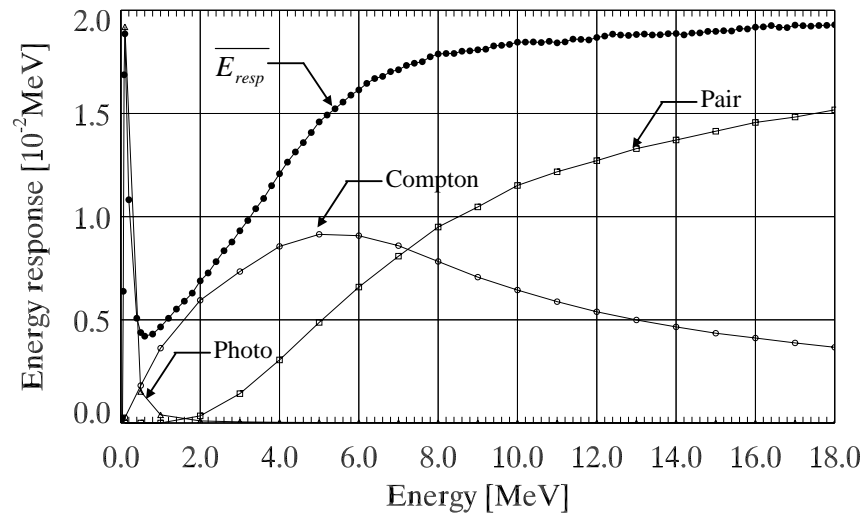


Figure 3.9 Simulated energy responses for different interaction types. At low energies, the photo-electric effect is predominant. For energies between 1 and 7 MeV, the energy deposition is governed by Compton scattering. Above 7 MeV, energy deposition due to Compton scattering decreases with growing energy of the incident photons due to a bigger chance for electrons to be transferred through the phosphor screen. At high energies, pair production is most important for the energy deposited in the phosphor layer.

specified interactions such as only photo-electric effect, Compton scattering, or pair production. As expected, at low energies the photo-electric effect is responsible for the energy deposition. More details can be observed from Figure 3.10, where for each interaction type the components of Table 3.2 are presented.

Obviously, the photo-electric effect deposits energy solely due to electrons released in the phosphor layer since the photo-electrons released in the copper plate have too low energies to reach the phosphor layer. The importance of Compton scattering is clearly visible from Figure 3.9. With increasing energy up to 5 MeV, an increase of energy deposition due to Compton scattering occurs. As seen from Figure 3.10, the main contribution is given by electrons released in the copper plate except for very low energies, where electrons released in $\text{Gd}_2\text{O}_2\text{S:Tb}$ are more important (as already seen for the photo-electric effect). Above 5 MeV a decrease of the Compton scattering component takes place, indicating that the energy of the Compton electrons is large enough so that the electron can be transmitted through the entire phosphor screen. Above 1 MeV, energy can be deposited by pair production. The main component is caused by electrons and (although less important) positrons released in the copper plate.

For pair production, the particles released in the phosphor layer do not contribute much for energy deposition. As expected, for high energies (above 7 MeV), pair production is the most important component to the total energy deposited in the phosphor layer.

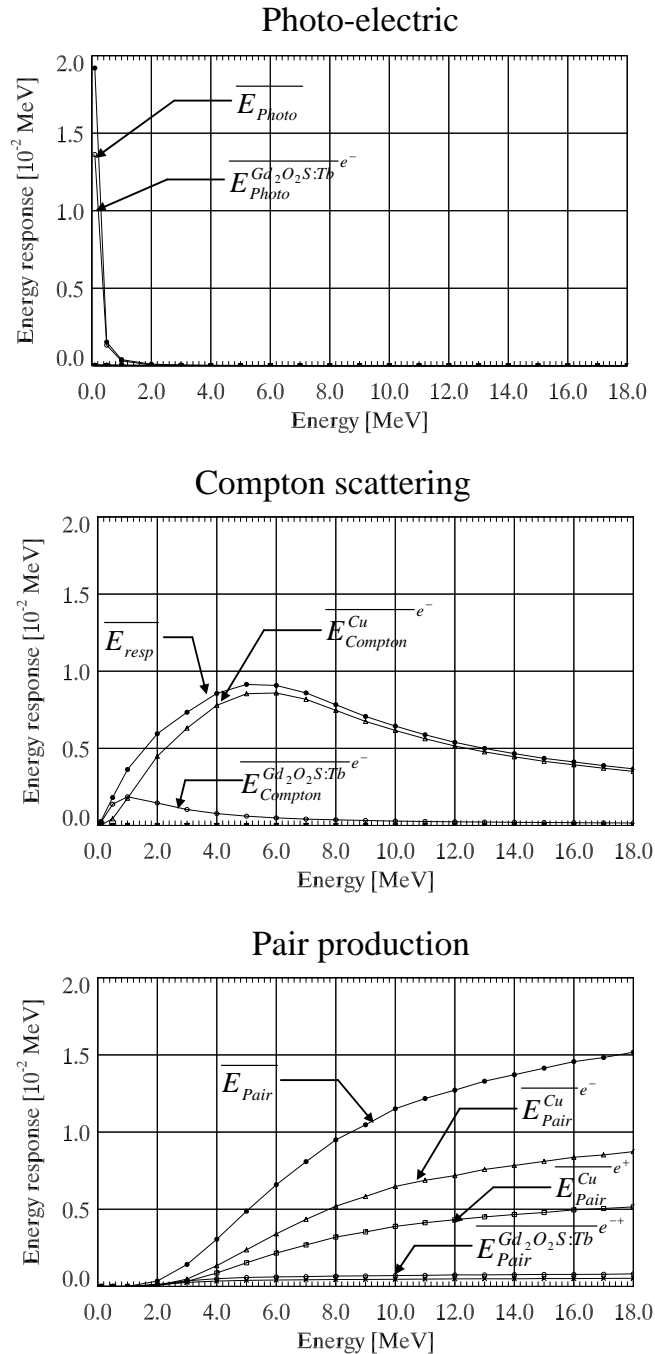


Figure 3.10 Energy responses for different interaction types. Whereas the photo-electric effect is governed by electrons released in the phosphor layer, Compton scattering and even more distinctively pair production are predominated by particles released from the copper plate. More details are given in the text.

The influence of this energy response to a polyenergetic beam is analyzed by taking energy spectra from Fix *et al.* (2001 a, b). Provided that $\varphi(E)dE$ designs the number of incident photons with an energy between E and $E + dE$, the energy response $\overline{E_{resp,poly}}$ to a polyenergetic beam is given by

$$\overline{E_{resp,poly}} = \int_0^{E_{max}} \overline{E_{resp}}(E) \cdot \varphi(E) dE.$$

where E_{max} denotes the maximum energy for the energy spectrum considered. Figure 3.11 shows the energy spectra of a 6 and a 15 MV photon beam, respectively, together with the energy response of the EPID and a polyenergetic energy response $\overline{E_{resp,poly}}(E)$ defined by

$$\overline{E_{resp,poly}}(E) = \overline{E_{resp}}(E) \cdot \varphi(E) dE.$$

From Figure 3.10 it can be proposed that for 6 and for 15 MV, mainly Compton scattering is responsible for the energy deposition in the phosphor layer. These suggestions are endorsed in Table 3.3, where the different contributions to the energy deposition are summarized. For these investigations, the MC simulations were forced to consider solely a certain interaction type. As expected, Compton scattering is most dominant with 67.5% and 61.6% of total energy deposition for 6 and for 15 MV, respectively, whereas photo-electric effect (16.9% and 1.1%, respectively) and pair production (12.2% and 32.1%, respectively) are smaller contributions. However, at 15 MV the energy deposition due to pair production is increased by a factor of three compared to 6 MV, while photo-electric effect can be neglected for 15 MV but not for 6 MV. Note that in all these investigations the MC simulations were restricted to simulate only a specified interaction type but not combinations of them. That is the reason why the sum of all components listed up in Table 3.3 is less than one.

Table 3.3 Energy deposition due to an incident polyenergetic photon beam subdivided into the three interaction types: photo-electric effect, Compton scattering, and pair-production.

Interaction	6 MV	15 MV
Photo-electric effect	16.9%	1.1%
Compton Scattering	67.5%	61.6%
Pair production	12.2%	32.1%

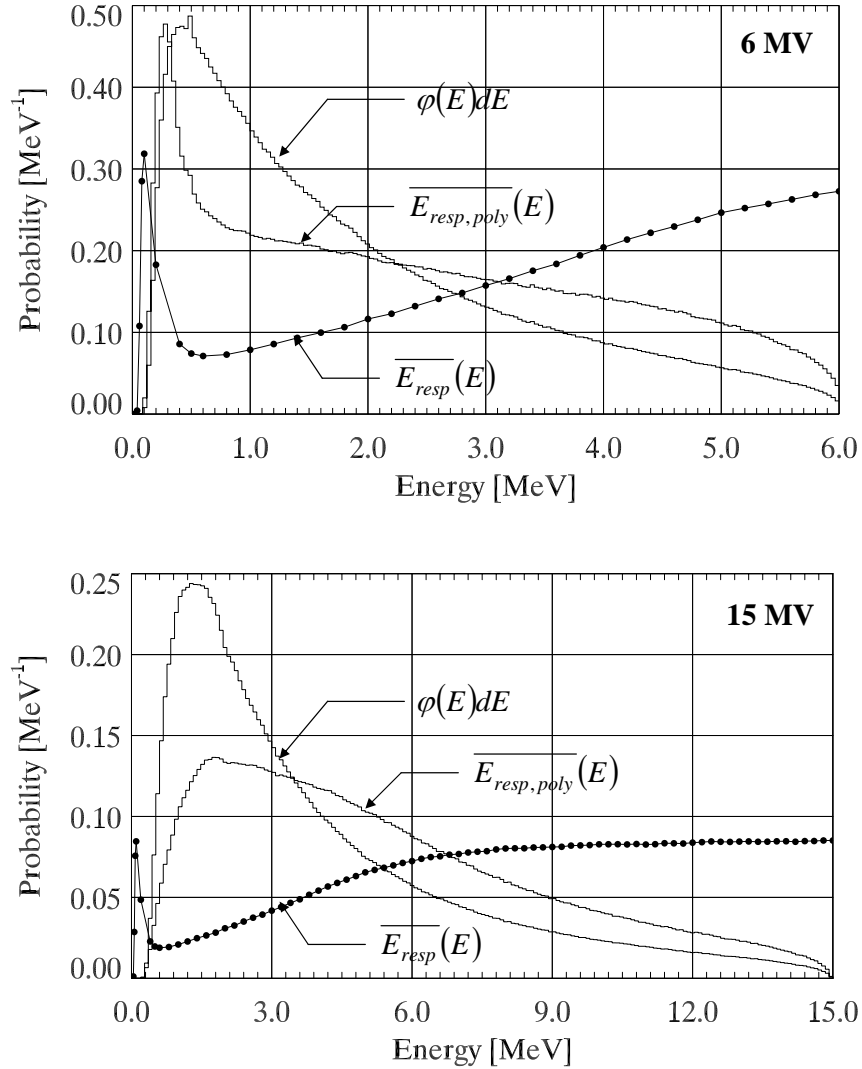


Figure 3.11 Energy deposition due to an incident polyenergetic pencil beam. The upper figure shows the situation of a 6 MV photon beam, where the lower figure represents a 15 MV case. The energy spectra are obtained from a beammodel of a Varian Clinac 2300 C/D. The energy response of the EPID is overlaid in the figure together with a corresponding polyenergetic energy response.

Figure 3.12 provides more details on the influence of different components (c.f. Table 3.2) to the energy deposition due to an incident polyenergetic beam. For both polyenergetic beams the most important contributions are electrons released in the copper plate with 59.9% and 70.6% for 6 MV and 15 MV, respectively. Electrons released just in the phosphor layer are more important for 6 MV (32.1%) than for 15 MV (15.7%). In contrast to the 6 MV case, the positrons released in the copper plate contribute considerably to the energy deposition (10.0%) for 15 MV. For both energies, the contribution of positrons

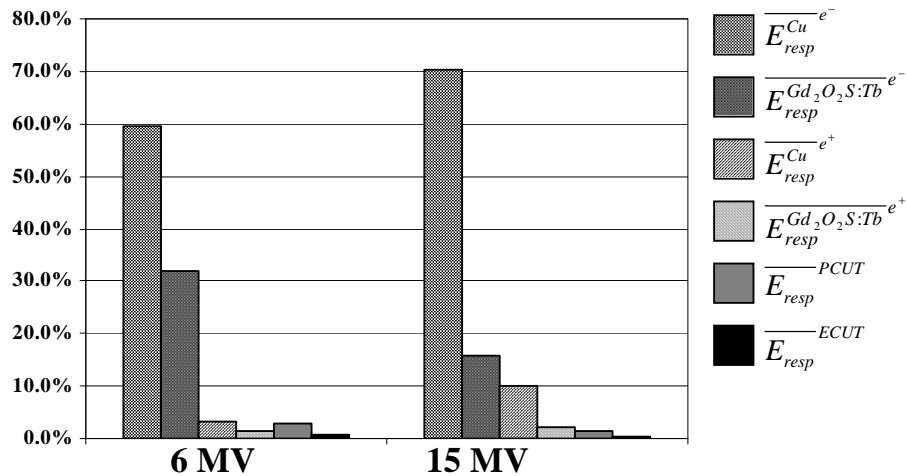


Figure 3.12 Detailed analysis of the energy deposition due to polyenergetic (6 MV and 15 MV) photon beams. The figure demonstrates that the energy deposition is governed by electrons released from the copper plate. The influence of higher photon energies is clearly visible for the positrons, which are only important for 15 MV. On the other hand, the electrons released only in the phosphor screen show a higher contribution for 6 MV than 15 MV, demonstrating the effect of using a copper plate to increase the efficiency of the detector.

released just in the phosphor layer is marginal (1.4% for 6 MV and 2.1% for 15 MV, respectively). However, the energy deposition due to particles falling below the GEANT cutoff energies is in the order of 3% and needs to be taken into account.

3.6 SPREAD OF HIGH-ENERGY PARTICLES

As defined in Section 3.3, stage 2 of the QAD analysis addresses the spread of high-energy particles. In QAD analysis, this process is described by the corresponding MTF. Again, the MC method is employed to calculate this MTF. Figure 3.13 illustrates the geometric design as has been implemented into GEANT. In these simulations, x-ray photons are impinging perpendicularly on the detector. An infinitesimally thin line source is used and the energy deposition in the phosphor screen is scored across the line source direction resulting in a point-spread-function (PSF). To improve the understanding of the physical processes responsible for the spread of high-energy particles, the energy deposition process was refined by using the components already defined earlier.

Figure 3.14 shows the PSFs for different monoenergetic photon beams. The normalization is such that for each energy the PSF at distance 0 cm is 1. For all

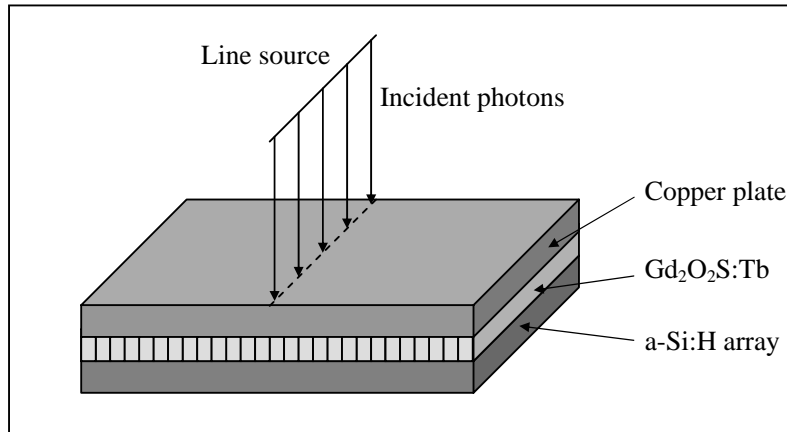


Figure 3.13 The geometric setup for the MC simulations of the spread of high-energy particles. Photons are released from a line source and impinge the a-Si:H EPID. The deposited energy within the phosphor layer is scored in stripes of 5 μm width.

energies, the decrease of the normalized PSF to 1% is found to be within 0.5 cm. Unsurprisingly, the most decreasing PSF appears for 100 keV. For this specific energy, mainly photo-electric interactions take place and the released electrons have too small energies to deposit energy at large distances. Interestingly, the broadest PSF does not correspond to the highest energy considered but to 6 MeV. From Figure 3.8 it turns out that for 6 MeV Compton scattering and pair

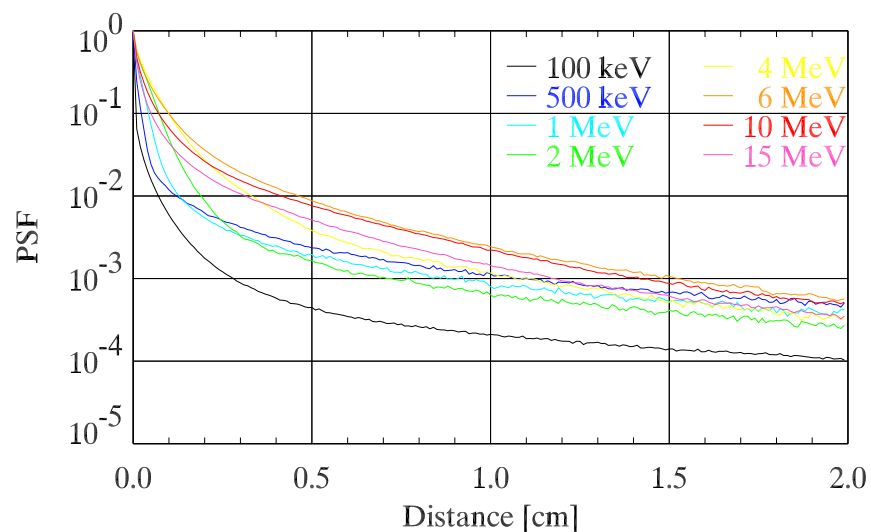


Figure 3.14 The lateral spread of high-energy particles is given by the point-spread function (PSF). The PSF describes the energy deposited in the phosphor layer as a function of lateral distance. Different energies of the incident photons lead to different PSFs, which is a result of different interactions and scattering properties (see text for more details).

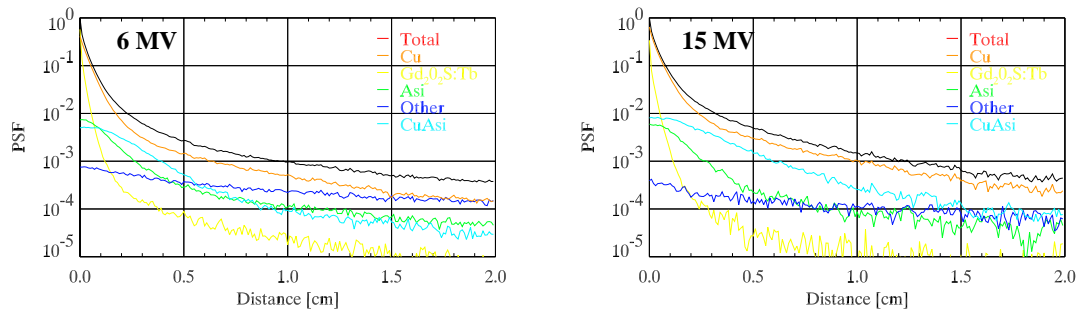


Figure 3.15 The PSF for 6 (left) and 15 MV (right) photon beams. In addition to the total PSF the PSF is subdivided into the main contributors to the energy deposition in the phosphor layer. Obviously, the particles released from the copper plate contribute for the most part of the lateral spread.

production are nearly of the same importance, while for higher energies the Compton scattering component is decreased. Additionally, Figure 3.9 reveals that for 6 MeV mainly electrons released in the copper plate contribute to the energy deposition. A more detailed analysis on the basis of these components shows that mainly the electrons released in the copper plate are responsible for the differences in the PSFs for different energies.

The results for polyenergetic photon beams are given in Figure 3.15, where besides the original PSF also the main contributors to the energy deposition are shown. The PSF decreases to 1% within 2.3 mm and 3.2 mm for 6 and 15 MV, respectively. While for both beam energies, the energy deposition is governed by particles (predominantly electrons) released from the copper plate, there are other components contributing to the energy deposition. Note that with increasing

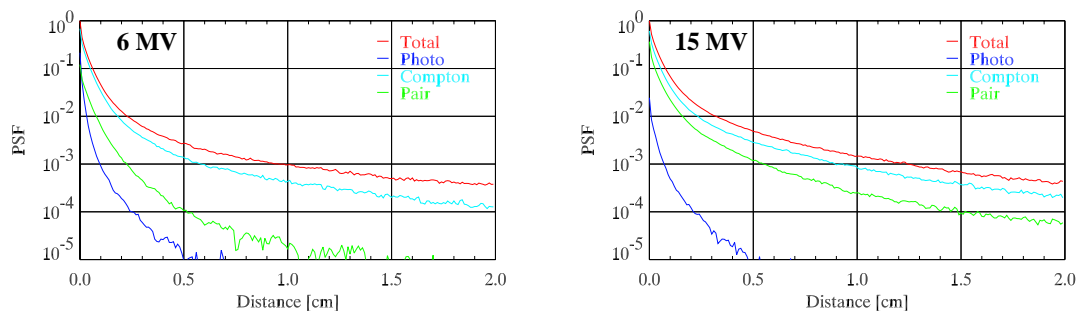


Figure 3.16 For 6 (left) and 15 MV (right) the PSF is subdivided into parts of different interaction types. Unsurprisingly, the Compton scattering governs the energy deposition. However, at least for 15 MV, pair production is essential.

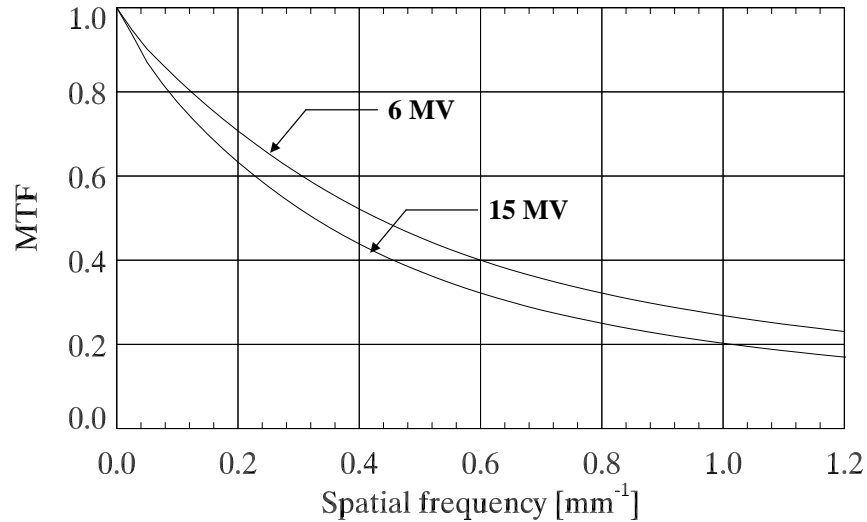


Figure 3.17 The MTF for 6 and 15 MV photons obtained from MC calculations of the lateral spread of energy deposition in the phosphor layer. The MTF is given by the amplitude of the fourier transform of the PSF and describes the contrast as a function of the spatial frequency.

distance, the relative importance of the particles released in the copper plate is more or less constant, whereas the relative importance of the particles solely interacting in the phosphor layer is decreasing. In any case, however, the spread of high-energy particles is primarily determined by Compton scattering as shown in Figure 3.16. However, for 15 MV the pair production process shows an essential contribution to the energy deposition. In these simulations the GEANT code has been forced to solely simulate either photo-electric, Compton scattering, or pair production interactions but not combinations of them. For instance, if a Compton scattered electron produces x-ray photons by radiation loss (bremsstrahlung) which themselves undergo photo-electric interactions, the latter interactions and thus the corresponding energy deposition would not be simulated by GEANT, if solely Compton scattering is simulated. As a consequence, the sum of the energy depositions according to these components is always lower than the total energy deposited.

To calculate the corresponding MTFs, a fast-fourier transform (FFT) of the PSF has been performed. In Figure 3.17 the results for 6 and 15 MV photons are given. For both energies considered, the MTF of the spread of high-energy particles leads to spatial resolution better than 1 mm^{-1} in the portal plane. Due to the increased lateral spread, the MTF of the 15 MV photon beam is slightly inferior compared to 6 MV.

3.7 PRODUCTION OF OPTICAL PHOTONS

To calculate the number of optical photons released in the phosphor layer, the energy deposition has to be multiplied with the energy conversion efficiency η and divided by the energy of an optical photon $\overline{E_{opt}}$. Table 3.4 summarizes the energy deposition for several photon energies E (Column 1) incident on the detector. Column 2 represents the energy response $\overline{E_{resp}}(E)$. With respect to QAD analysis, the energy response needs to be converted to the energy deposition per detected photon $\overline{E_{ab}}(E)$ (Column 4), which is performed by calculating the number of pulses per incident photon QAE (Column 3). Eventually, the number of optical photons corresponds to the gain $\overline{g_3}$ of stage 3 and is presented in Column 5. Due to the stochastic process of energy deposition noise is attributed to the production of visible photons. The noise and thus the Poisson excess ε_{g_i} (Column 6) are determined by the standard deviation of the corresponding AED.

Table 3.4 The number of optical photons released in the phosphor layer is related to the energy deposition in the phosphor screen. For QAD analysis, the number of optical photons per detected photon $\overline{g_3}$ is needed.

E	$\overline{E_{resp}}(E)$ [MeV]	QAE	$\overline{E_{ab}}(E)$ [MeV]	$\overline{g_3}$	ε_{g_i}
0.1 MeV	0.0188	0.2522	0.07	4876	
0.5 MeV	0.0044	0.0254	0.17	11268	
1.0 MeV	0.0047	0.0178	0.26	17094	
2.0 MeV	0.0069	0.0181	0.38	24853	
4.0 MeV	0.0121	0.0268	0.45	29423	
6.0 MeV	0.0161	0.0351	0.46	30009	
10.0 MeV	0.0185	0.0424	0.44	28392	
15.0 MeV	0.0190	0.0454	0.42	27249	
6 MV	0.00731	0.0238	0.307	20002	20288
15 MV	0.01066	0.0260	0.409	26679	23678

From the numbers in Table 3.4 it turns out that the number of optical photons $\overline{g_3}$ per detected x-ray photon depends critically on the energy of the incident x-ray photon, as is illustrated in Figure 3.18. For low energies, the energy response is high (c.f. Table 3.4) resulting in a large number of optical photons per *incident* x-ray photon. But due to the high QAE for low energies – indicating that lots of impinging x-ray photons are detected – the number of optical photons per *detected* x-ray photon is small for low energies. The number of optical photons per detected x-ray photon increases with the energy of the x-ray photon until

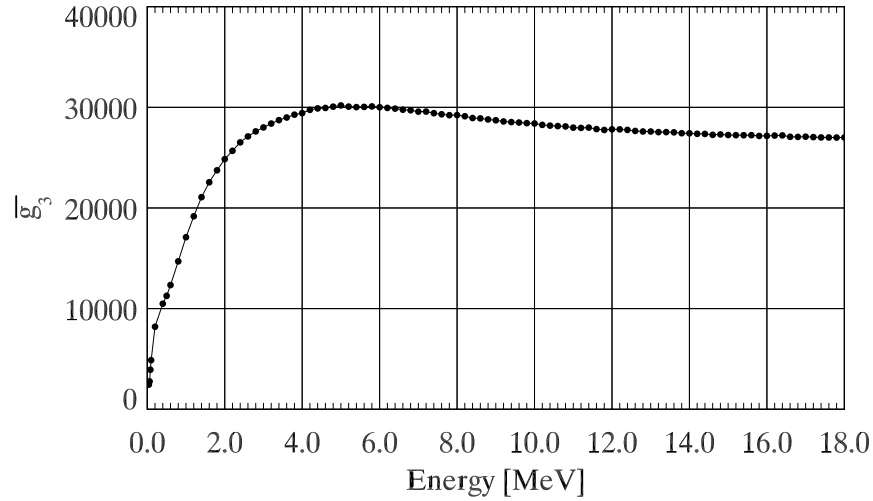


Figure 3.18 The number of optical photons per detected x-ray photon as a function of the energy of the incident x-ray photon. \bar{g}_3 is small for low energies due to a high QAE. Until 5 MeV an increase is observed for \bar{g}_3 , while above 6 MeV a slow decrease is apparent.

about 5 MeV. Above 6 MeV, \bar{g}_3 decreases slowly with increasing energy of the incident x-ray photon. For polyenergetic beams, \bar{g}_3 is about 20000 for 6 MV and 27000 for 15 MV, respectively, which corresponds to 1.3 MeV for 6 MV and 2.5 MeV for 15 MV, respectively.

Thus far, the energy deposition was scored in the entire phosphor layer but nothing has been pointed out about the dependence on the scoring depth. In the following, however, this subject is investigated by the simulation of depth dose curves in the phosphor layer. The corresponding results are given in Figures 3.19 for 6 and 15 MV photon beams. As indicated before, the energy deposition is

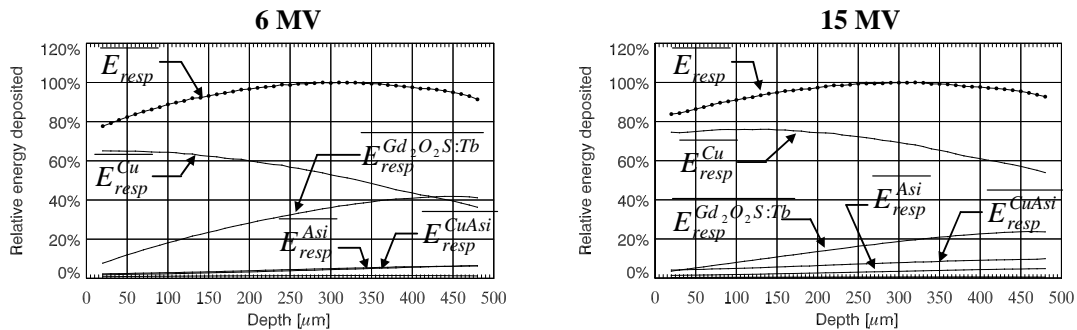


Figure 3.19 The energy deposited in the phosphor layer depends on the scoring depth. While for 15 MV the ‘copper particles’ are most dominant, the energy deposition for 6 MV is also determined by ‘phosphor particles’.

subdivided into the known components (cf. Table 3.2). The curves associated to the total energy deposition are normalized to the maximum energy deposited in the phosphor which takes place at a scoring depth of about 320 μm , independent of the initial energy. However, there are distinct differences in the components for 6 and 15 MV photon beams. For 15 MV the energy deposition is chiefly determined by particles released in the copper plate, while the component associated to the particles released only in the phosphor layer is inferior. For 6 MV, on the other hand, there is an intersection point at about 420 μm for the component related to the ‘copper particles’ and the one related to the ‘phosphor particles’.

3.8 TRANSPORT OF OPTICAL PHOTONS

In order to investigate the performance of the phosphor screen, a model of the transport of the optical photons is applied (Radcliffe *et al.* 1993). This model is based on the assumption that optical photons are either absorbed or scattered in the phosphor medium. In addition, optical photons are absorbed or reflected at the boundary between the copper plate and the phosphor.

To simulate the absorption within $\text{Gd}_2\text{O}_2\text{S:Tb}$, an exponential absorption length distribution $\exp(-T/\bar{T})$ is considered, from which the transport length T is sampled

$$T = -\bar{T} \cdot \ln(1 - \xi)$$

where ξ denotes a uniformly distributed random number. For the absorption length \bar{T} a value of 4 cm is used, in accordance to the literature (Kausch *et al.* 1999, Radcliffe *et al.* 1993).

Scattering of optical photons occurs due to Fresnel reflection and refraction at the boundaries between the phosphor grains and the binder. As has been shown in the literature (Maidment and Yaffe 1995), the binder inhabits only a small fraction of the total volume and can therefore be neglected for the simulations. In the MC algorithm a scattering length S is calculated by sampling an exponential scattering length distribution $\exp(-S/\bar{S})$ and the scattering is assumed to be isotropic. A mean scattering length \bar{S} of 25 μm is taken, which is similar to the distances between the grains.

An average refractive index of 2.4 is used to account for the total reflection, which occurs at the surface of the phosphor screen (Radcliffe *et al.* 1993). The PortalVisionTM aS500 encompasses a black paper sheet between the copper plate

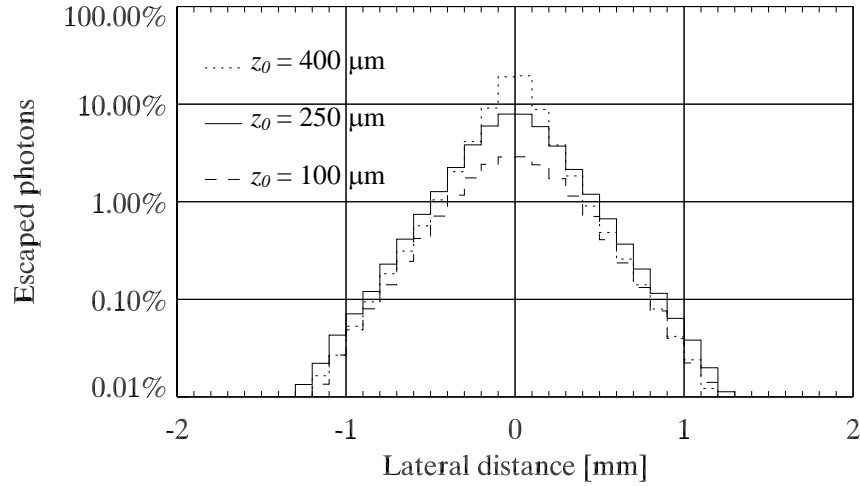


Figure 3.20 The point spread functions (PSFs) describe the number of optical photons leaving the phosphor at the point (x,y) in the exit plane of the phosphor layer. The figure shows PSFs for two different starting points.

and the phosphor layer. As a consequence, no reflection at the copper plate takes place.

Based on these assumptions, the transport of optical photons is simulated by starting a certain number of optical photons at a starting point $\vec{P}_0 = (0,0,z_0)$. The starting photons are assumed to be released isotropically, thus for each particle a

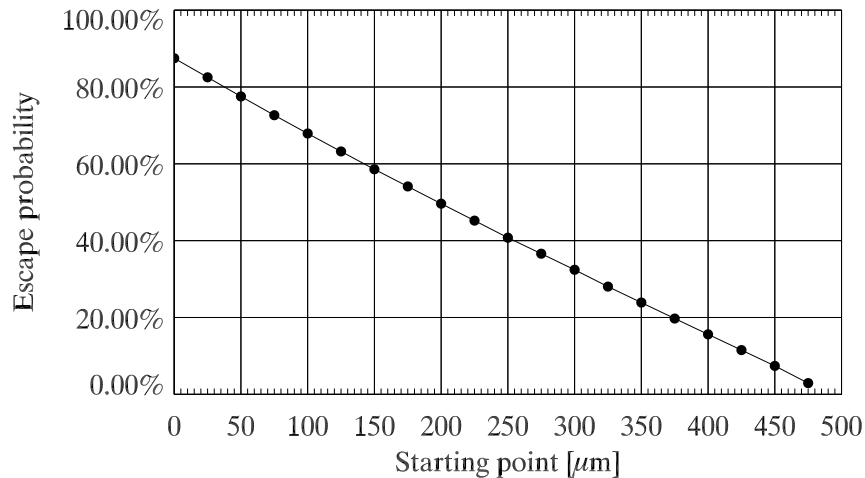


Figure 3.21 The escape probability as a function of the starting point location (distance between the bottom boundary of the phosphor layer and the starting point). As expected, the nearer the starting point to the bottom of the 0.5 mm thick $\text{Gd}_2\text{O}_2\text{S:Tb}$, the higher the escape probability. Note, that only a small fraction of optical photons released close to the top boundary are able to escape from the phosphor.

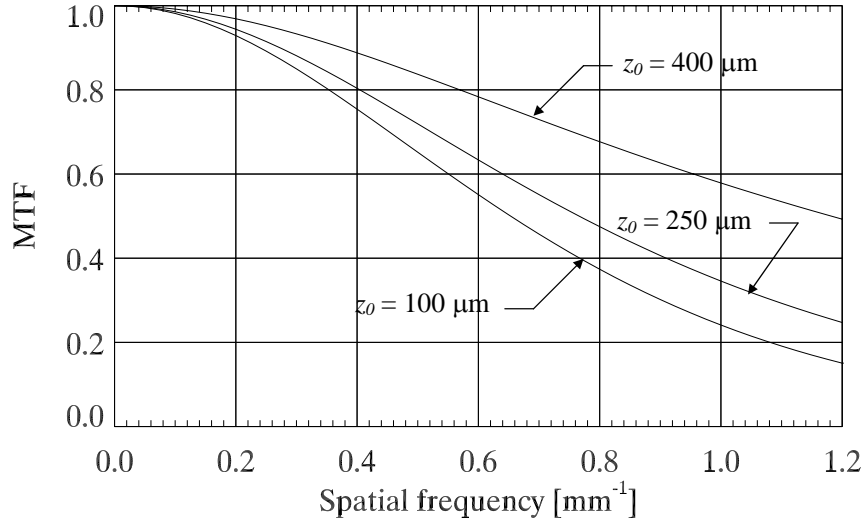


Figure 3.22 The MTF of the transport of optical photons for different starting points ($z_0=400$, 250, and 100 μm). Due to the increased probability to scatter for visible photons starting at lower depths, the MTF is decreased.

vector \vec{Q} representing the direction of motion is determined. Subsequently, the absorption length T and the scattering length S are sampled. The photon is then transported to the point $\vec{P}_1 = \vec{P}_0 + S \cdot \vec{Q}$. If \vec{P}_1 is located outside the phosphor screen, then reflection is simulated as described above. Otherwise, the next scattering length is sampled and the simulation continues until its total travel distance exceeds the absorption length or the photon escapes from the phosphor. In the latter case, the MC code generates an entry in the optical fluence distribution at the phosphor/a-Si:H array interface. The optical fluence distribution $l_{z_0}(x, y)$ expresses the number of optical photons escaped at (x, y) per started photon at the starting point $\vec{P}_0 = (0, 0, z_0)$. Since the phosphor material is homogeneous and large enough, $l_{z_0}(x, y)$ is rotational symmetric. As a consequence, $l_{z_0}(x, y)$ represents a point-spread function (PSF) depending on the location of the started particles z_0 .

Figure 3.20 shows some PSFs for different starting point locations. The area under the curve corresponds to the escape probability for an optical photon released at the specified starting point. As expected, the escape probability increases with increasing z_0 , as is shown in Figure 3.21. Furthermore, an expanded spread of optical photons is observed for lower values of z_0 . However, with respect to the pixel size of the PortalVisionTM aS500, the results of the optical transport model demonstrate that the spread of optical photons can be neglected. The corresponding MTFs of the transport of optical photons are depicted in Figure 3.22 for different starting locations z_0 .

As has been demonstrated previously, the energy deposition in the phosphor layer depends on the scoring depth (cf. Figure 3.19). Consequently, the result of the transport of optical photons – the point-spread function $l_{z_0}(x, y)$ – needs to be combined with the energy e_{z_0} deposited at the depth z_0 . Following this, point-spread functions are calculated for 6 and 15 MV photon beams according to

$$PSF(x, y) = \sum_{z_0} e_{z_0} \cdot l_{z_0}(x, y).$$

The corresponding escape probabilities are 42.9% for 6 MV and 43.2% for 15 MV, respectively. Further analysis of the data indicates that the combination of the depth dependence of the energy deposition and the transport of optical photons in the phosphor screen can be simplified. The results confirm the assumption that the transport of optical photons can be taken into account by assuming that all optical photons are released in the center ($z_0 = 250 \mu\text{m}$) of the phosphor layer.

3.9 COLLECTION AND DETECTION OF OPTICAL PHOTONS

The steps 6 and 7 of the QAD analysis deal with the collection and the detection of the optical photons escaped from the phosphor screen. As has been shown in Chapter 2, each pixel of the EPID's flat-panel array incorporates a photodiode, acting as a sensor and charge capacity, and a TFT, which is needed for readout purposes. Figure 2.7 gives a sketch of the pixel arrangement, from which it is seen that the actual sensitive area does not match to the photodiode's area, but is reduced by the area, which is needed for the TFTs and additional readout electronics. This is expressed by the so-called fill-factor, which is 84% for the PortalVision™ aS500 (manufacturer).

The detection of optical photons by the photodiode depends on the wavelength of the photons (Saleh and Teich 1991). The photons released from a $\text{Gd}_2\text{O}_2\text{S:Tb}$ phosphor layer have a major output at 550 nm, for which the photodiode's detection efficiency is 80% (Antonuk *et al.* 1998).

3.10 QAD AND DQE OF THE PORTALVISION™ AS500

In the previous sections, all signal forming steps are investigated. Table 3.5 summarizes the corresponding gains and poisson excesses for 6 and 15 MV photon beams. At a spatial frequency of zero, the influence of the spread of high-

energy particles as well as the spread of optical photons is ignored. As a consequence, the QAD is highest for zero spatial frequency ($f=0$). This is demonstrated in Figure 3.23 where the QADs for 6 and 15 MV are given at different spatial frequencies f . As expected, the QAD decreases with increasing spatial frequency since the number of quanta at a certain stage is reduced by the corresponding MTF.

Table 3.5 The eight stages and their corresponding gains, Poisson excesses, and MTFs for 6 and 15 MV photon beams.

Stage	Description	Gain	Poisson excess	MTF
0	Incident photon	$g_0 = 1$	$\varepsilon_0 = 0$	1
1	Quantum absorption efficiency	6 MV $g_1 = 0.0238065$	$\varepsilon_1 = -g_1$	1
		15 MV $g_1 = 0.0260444$	$\varepsilon_1 = -g_1$	1
2	Spread of charged particles	$g_2 = 1$	$\varepsilon_2 = -1$	T_2
3	Conversion to visible photons	6 MV $g_3 = 20002$	$\varepsilon_3 = 20288$	1
		15 MV $g_3 = 26679$	$\varepsilon_3 = 23678$	1
4	Spread of visible photons	$g_4 = 1$	$\varepsilon_4 = -1$	T_4
5	Escape of visible photons	$g_5 = 0.43$	$\varepsilon_5 = -g_5$	1
6	Collection by photodiode	$g_6 = 0.84$	$\varepsilon_6 = -g_6$	1
7	Detection by photodiode	$g_7 = 0.80$	$\varepsilon_7 = -g_7$	1

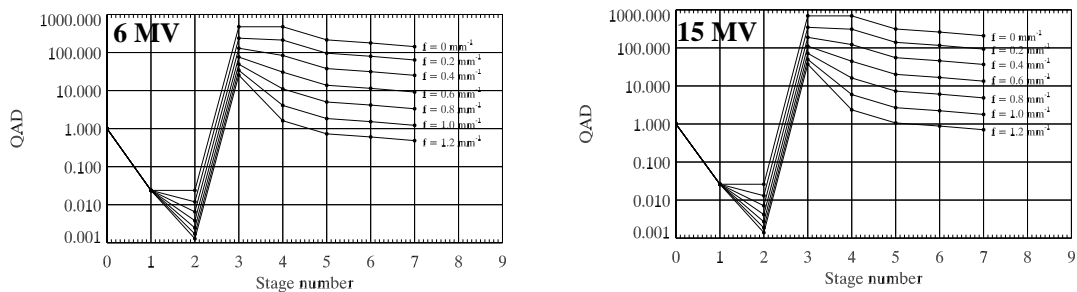


Figure 3.23 The QADs for 6 and 15 MV photon beams demonstrate the very good imaging properties of the *a*-Si:H based EPID.

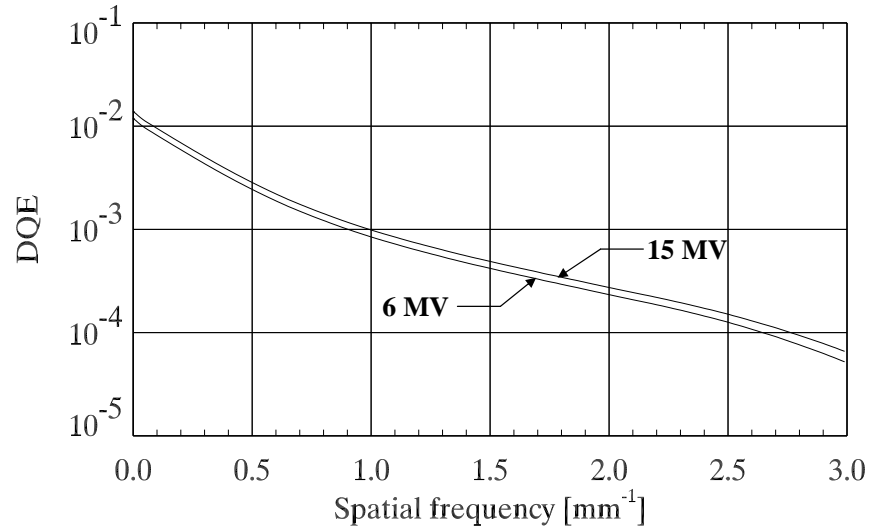


Figure 3.24 The spatial frequency dependence of the DQE for 6 and 15 MV photon beams. At a spatial frequency of zero, the DQE is 1.18% for 6 MV and 1.38 for 15 MV, respectively.

While the QAD pays no attention to noise propagation, the DQE describes how the signal and noise are propagated through an imaging system. As for the QAD, the DQE is highest at spatial frequency of zero and decreases with increasing frequency. In Figure 3.24 the DQE of the PortalVisionTM aS500 is given for 6 and 15 MV.

4

Calculation of Portal Dose Images

4.1 OVERVIEW

The dosimetric verification procedure consists in the comparison between measured and calculated portal dose images (PDIs). Due to practical reasons, the airgap between the patient's exit surface and the EPID is of the order of 30 or more centimeters. For such distances, commercial treatment planning systems do not provide accurate portal dose calculations (Pasma *et al.* 2002). Several groups made efforts to develop algorithms for portal dose predictions (Wong *et al.* 1990, McNutt *et al.* 1996, Pasma *et al.* 1998, 2002, McCurdy and Pistorius 2000). In this thesis, the Monte Carlo (MC) method is employed for the calculation of PDIs. Note that the use of MC simulations for portal dose prediction fulfills the demand on a verification method being fully independent of the original treatment planning system.

In order to make portal dose calculations applicable for intensity modulated beams, several steps are necessary. First of all, an accurate description of the beam characteristics of the treatment unit is required. For this purpose, a beammodel had to be developed enabling the simulation of dynamically applied treatment fields. Subsequently, the patient's anatomy needs to be considered in the MC simulations. In this thesis, phase space data are generated to permit the interface between the GEANT code and the EGSnrc based DOSXYZnrc. While in GEANT, the consideration of the patient's anatomy is not straightforward, the DOSXYZnrc allows to import a CT data set for patient related calculations.

4.2 MULTIPLE SOURCE MODEL

The MC method is considered to be the most accurate method for dose calculations. MC simulations mimic the transport of ionizing particles through matter by utilizing probability distributions obtained from cross-section data of the corresponding particle interactions. However, in order to calculate patient

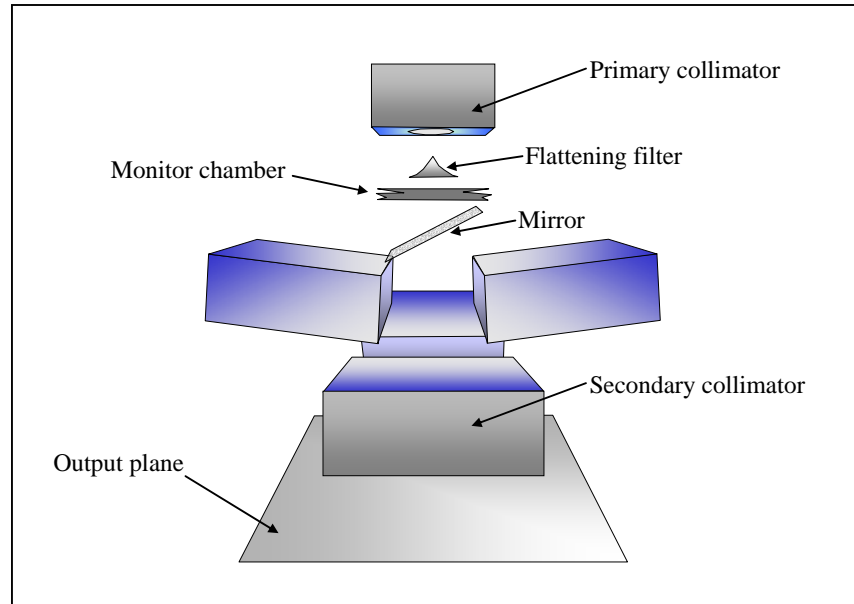


Figure 4.1 Main components of a Varian Clinac 2300 C/D as implemented in the multiple source model (MSM). For a set of square field sizes the radiation is transported through the complete geometry resulting in phase space (PS) data in the output plane. Based on these simulations, twelve sources of the beam defining system are characterized and provide an accurate beammodel for arbitrary rectangular fields for 6 and 15 MV photon beams.

related dose distributions, accurate knowledge of the beam characteristics is required.

In this thesis, the so-called multiple source model (MSM) is applied for the prediction of PDIs. The MSM has been developed at our institute and is an accurate beammodel for a Varian Clinac 2300 C/D for 6 and 15 MV photon beams (Fix *et al.* 2001 a, b). The basic principle of this model comprises the simulation of the radiation transport through the complete geometry of the linac head for a set of square fields (3×3 , 5×5 , 8×8 , 10×10 , 15×15 , 30×30 , and 40×40 cm²). From these simulations, phase space (PhSp) data for all particles intersecting a plane (perpendicular to the beam axis) below the secondary collimator are stored. For each particle crossing the output plane (cf. Figure 4.1), the PhSp data contains information such as the charge, the energy, the direction of motion, and the last interaction source in the linac head. The simulated PhSp data enable the definition and the parameterization of twelve sources representing the main components of the linac head. The MSM includes a fitting algorithm to extend the validity of the beammodel to arbitrary rectangular fields (containing the 3×3 cm² field) without the need of pre-calculation of corresponding PhSp data.

As has been shown by Fix et al. (2000 a, b), the MSM is a flexible and efficient tool for accurate dose calculation purposes. In addition, the accuracy has been investigated by comparing the MC calculated primary energy spectrum with an energy spectrum achieved by transmission measurements.

4.3 MONTE CARLO SIMULATION OF DMLC DELIVERY

The MSM is supplemented by the implementation of an 80-leaf MLC (Varian Medical Systems). As shown in Figure 4.2, each leaf is modeled by seven subvolumes. In order to reduce radiation leakage between adjacent leaves, the MLC includes a tongue and groove design, which is accounted for in the MC model. However, since in GEANT rounded forms are not straightforward to define, the leaf front ends are modeled as plane surfaces. Therefore, an additional shift of 1.2 mm between opposite leaves is implemented to account for the rounded form of the leaf front ends. The suitability of this correction has been shown in the literature (Arnfield *et al.* 2000, LoSasso *et al.* 1998, Wang *et al.* 1996).

The supplemented MSM allows the calculation of dose distributions of static and dynamic MLC fields. For the latter, the leafmotion file (as obtained from the leaf sequencer during inverse treatment planning) has to be discretized into static subfields. This approximation is performed such that the fraction of MUs

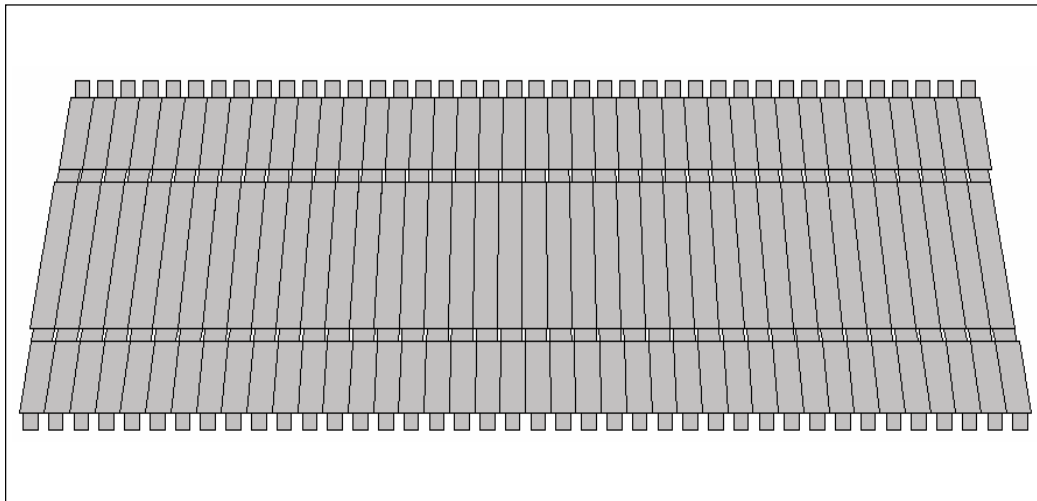


Figure 4.2 The MSM is supplemented by the implementation of an 80-leaf MLC (Varian Medical Systems). Each leaf is modeled by seven subvolumes and the tongue and groove design is taken into account.

delivered in each segment is kept constant. The simulation of dynamically applied fields is then accomplished so as to simulate each subfield independently.

4.4 PORTAL DOSE IMAGE CALCULATION

In order to calculate a PDI, the geometric representation of the patient needs to be implemented into GEANT. As was already indicated above, the definition of complex geometries (such as a patient) in GEANT is hard to perform. Thus at the moment, for treatment verification situations, we only consider artificial geometries (phantoms) imitating the patient. In Section 4.5 it will be elucidated how one can link GEANT with another MC calculation code (DOSXYZnrc) and thus enable to consider real patient anatomies by corresponding CT data.

Figure 4.3 shows an inhomogeneous phantom ($30 \times 30 \times 25 \text{ cm}^3$) consisting of solid water, an air (4 cm thick) and a bone (4 cm thick) inhomogeneity. The source-to-surface distance SSD is 90 cm. The a-Si:H EPID is represented as a homogeneous (polystyrene) slab with the dimensions $40 \times 40 \times 10 \text{ cm}^3$ and a source-to-detector distance SDD of 140 cm. Depending on the energy of the photon beam used, the portal dose is scored in different depths. While for 6 MV a depth of 3 cm is chosen, the scoring plane for 15 MV is located at 5 cm depth. In this way, the dose is scored with a voxel size of $1 \times 1 \times 10 \text{ mm}^3$.

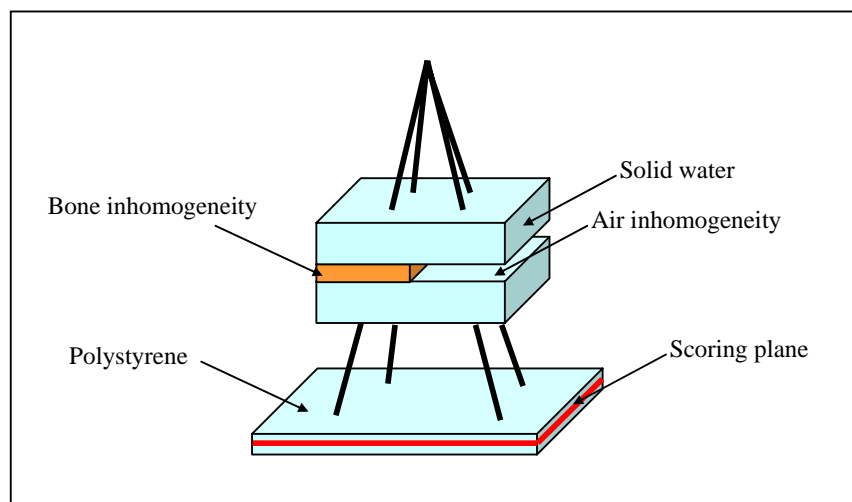


Figure 4.3 The inhomogeneous phantom considered for the calculation of a portal dose image (PDI) consists of solid water, an air and a bone inhomogeneity. The EPID is represented as a polystyrene slab with a thickness of 10 cm. In the MC calculations, the PDI is scored in a plane located at 3 cm depth for 6 MV and 5 cm for 15 MV, respectively.

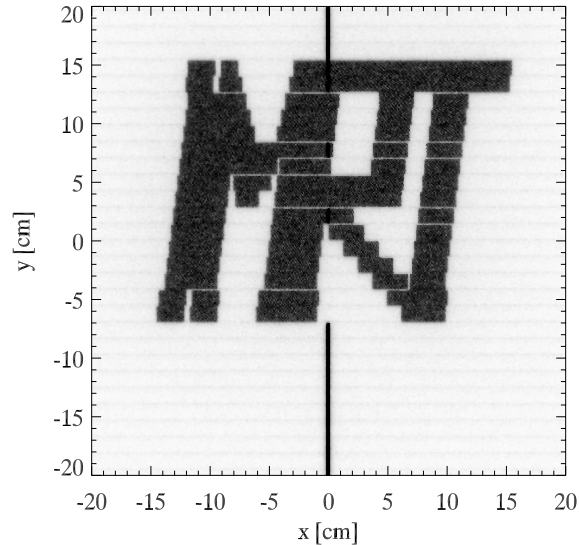


Figure 4.4 Monte Carlo simulated portal dose image (PDI) of an artificial IMRT beam ‘delivered’ by the step-and-shoot technique. Four subfields are needed to generate this intensity distribution. The leakage through adjacent leaves is clearly visible and relies on the tongue-and-groove design of the MLC. The rounded leaf ends are accounted for by the incorporation of a shift of 1.2 mm and affects the dose distribution, particularly if the leaves are not beneath the secondary collimators.

For the pre-treatment situation, where no phantom is in the beam, Figure 4.4 shows a PDI of an artificial IMRT delivery. The intensity is ‘delivered’ by the step-and-shoot technique with four subfields of a 6 MV photon beam. Each

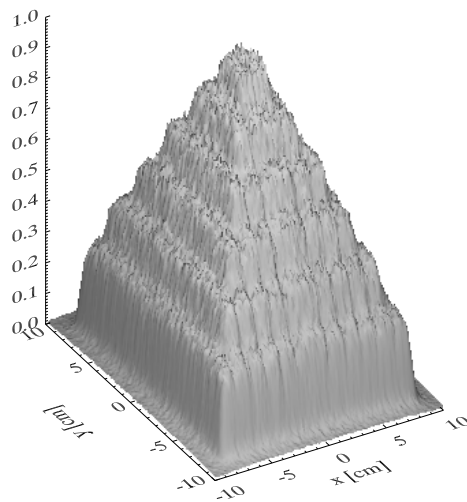


Figure 4.5 Simulated portal dose distribution for a 15 MV step-and-shoot ‘delivered’ field. This pyramidal distribution is used for benchmark purposes and contains seven subfields. The figure represents the pre-treatment situation (no patient in the beam). Due to statistics, which are inherent in the MC method, small fluctuations occur.

subfield contains the same number of photon histories (1000 Mio). The impact of the tongue and groove design is clearly visible. Furthermore, the radiation leakage between two opposing leaves affects the dose distributions enormously, as exposed by the dark (vertical) line. This is due to the additional shift of 1.2 mm introduced in the MLC model for taking the rounded leaf ends into account. In realistic cases, this situation would be avoided by positioning ‘closed’ opposing leaves under the secondary collimators.

Figure 4.5 shows a portal dose distribution of a step-and-shoot delivery, which is used for benchmark purposes in treatment planning systems. This application consists of seven subfields of a 15 MV photon beam shaping a pyramid with a maximum lateral extension of $12 \times 12 \text{ cm}^2$ at isocenter distance. As before, the

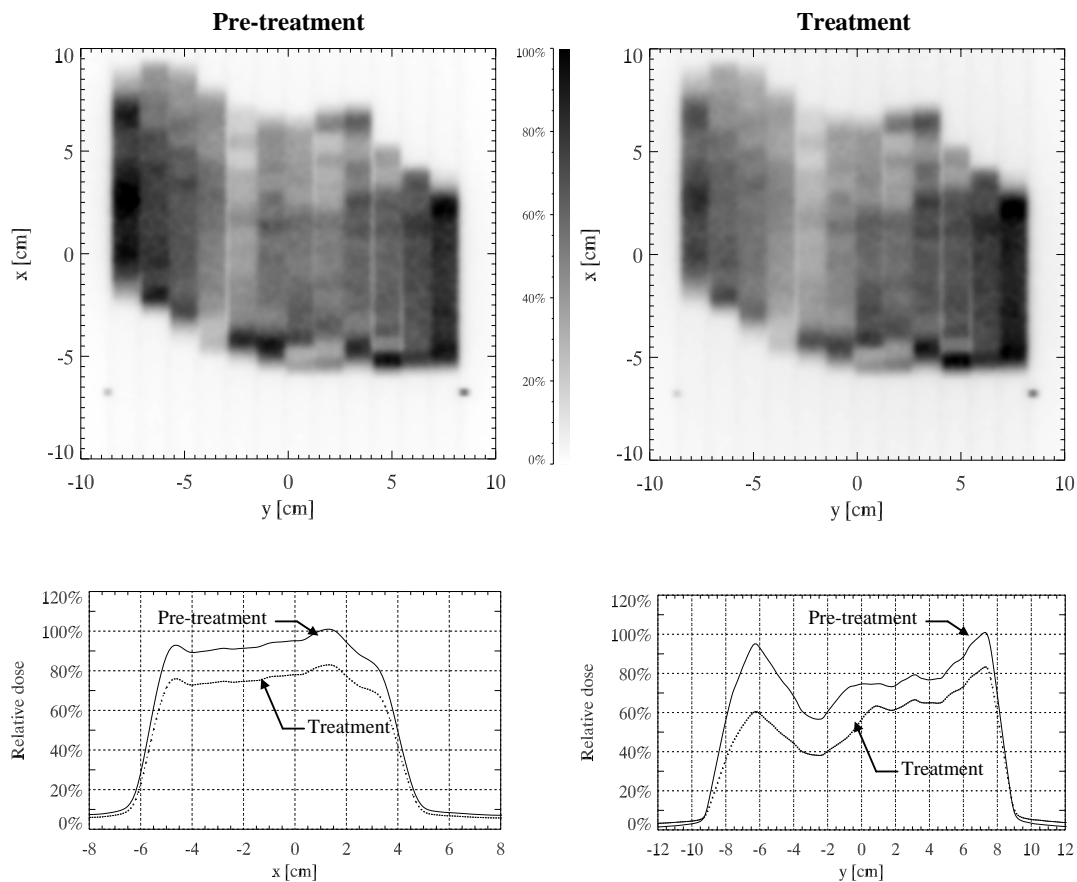


Figure 4.6 PDI and corresponding dose profiles of a realistic intensity modulated field ‘delivered’ by the sliding-window technique to the inhomogeneous phantom shown in Figure 4.3. This IMRT field corresponds to an optimized 6 MV treatment plan of a head and neck carcinoma. For the MC simulations, the field is discretized into 196 subfields and for each subfield 25 Mio. starting particles are simulated.

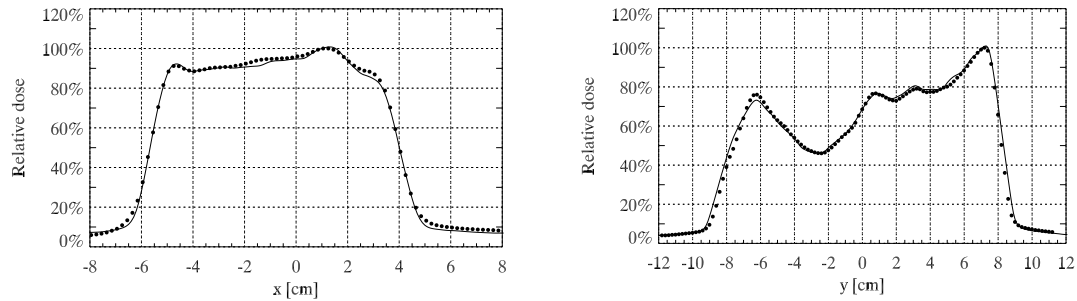


Figure 4.7 Calculated and measured (dotted) portal dose profiles for the treatment situation of the head and neck case. The measurements are performed by the use of an ionization chamber placed in a miniphantom. The very good agreement of 3% and 2 mm demonstrates the suitability of the supplemented MSM for accurate portal dose prediction.

PDI is calculated without any phantom in the beam (pre-treatment situation) and for an SDD of 140 cm. The PDI of the pyramid points up nicely the tongue and groove effect of the MLC on (portal) dose distributions. This effect is caused by the segmentation of the step-and-shoot delivery and results in a dose reduction between adjacent leaves of about 8% in the PDI. In contrast to the example shown in Figure 4.4, hot spots are avoided for the pyramid by placing the contact points of closed leaf pairs underneath the secondary collimator.

For a realistic IMRT delivery, Figure 4.6 shows two simulated PDIs and corresponding dose profiles for the pre-treatment as well as the treatment situation. The IMRT field considered is obtained from inverse treatment planning (Helios, Varian Medical Systems) of a head and neck carcinoma. The treatment plan consists of five 6 MV IMRT beam portals and the leaf trajectories are calculated according to the sliding-window technique (cf. Chapter 1). For the MC simulations, the leaf motion is subdivided such that a total of 196 subfields occur and for each subfield 25 Mio. starting particles are simulated in a sequential manner. For the treatment situation, the phantom shown in Figure 4.3 is used. Obviously, the air inhomogeneity is located on the left side leading to higher intensity values, whereas on the right side the dose values are lowered due to the increased attenuation by the bone structure. In addition to the PDI, the figure shows dose profiles along the leafmotion (x-) direction and perpendicularly (y-direction) to it.

In order to compare the MC simulated portal dose distributions, ionization chamber measurements are performed. For this purpose, the ionization chamber (RK 8305, Scanditronix) is put into a miniphantom. The miniphantom is built from polystyrene with the dimensions $7 \times 7 \times 10 \text{ cm}^3$. As is shown in Figure 4.7 for the treatment situation, the comparison between MC simulated portal dose profiles to ionization chamber measurements results in a good agreement of about 3% and 2 mm. The disagreement mainly occurs at the extremes of the intensity modulation and at steep dose gradients. However, since the resolution of the ionization chamber is limited due to its volumetric extension, the

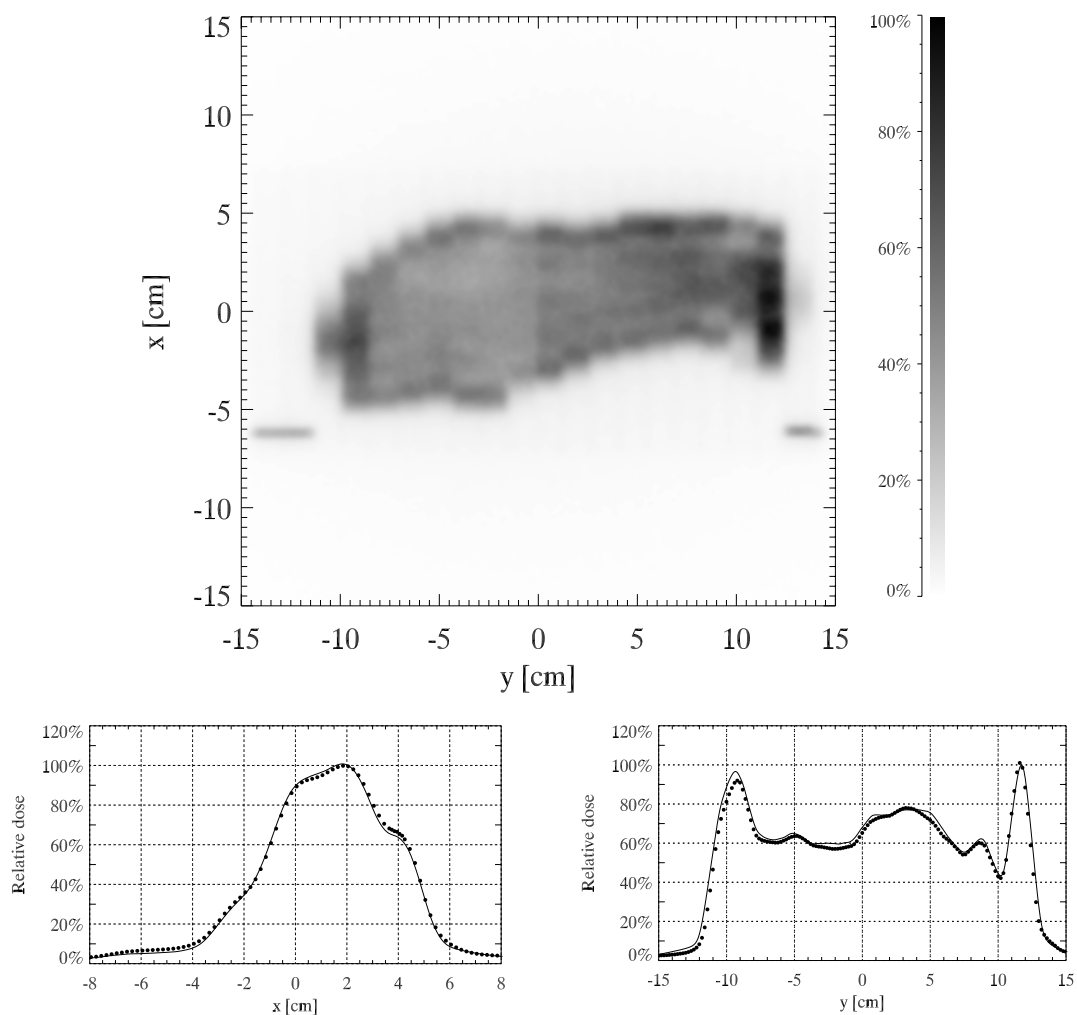


Figure 4.8 The PDI and corresponding dose profiles for the treatment situation of the bronchus case. The field belongs to an optimized treatment plan utilizing 15 MV photon beams. For the MC calculation, 25 Mio. starting particles are simulated for each subfield. Portal dose profiles are measured by the use of an ionization chamber (dotted). As for the 6 MV case (cf. Figure 4.7), very good agreement of 3% and 2 mm is observed between the MC calculated profiles and ionization chamber measurements.

deviations underline the difficulty to accurately measure intensity modulated treatment fields by the use of an ionization chamber.

The MC calculated PDI shown in Figure 4.8 is a result of a 15 MV photon beam for a realistic bronchus carcinoma. This field is subdivided into 177 subfields and for each subfield 25 Mio. histories are simulated. As before, the inhomogeneous phantom from Figure 4.3 is used for the treatment situation. A very good agreement of about 3% and 2 mm is observed between the MC calculated portal dose profiles and corresponding measurements by the use of an ionization chamber.

4.5 PDIs FOR REAL TREATMENTS USING THE MSM AND DOSXYZ

Thus far, only phantoms were used for portal dose calculations. Phantoms, in fact, play an important role in radiotherapy. However, to enable the calculation of PDIs for a real treatment situation, the patient's geometry has to be taken into

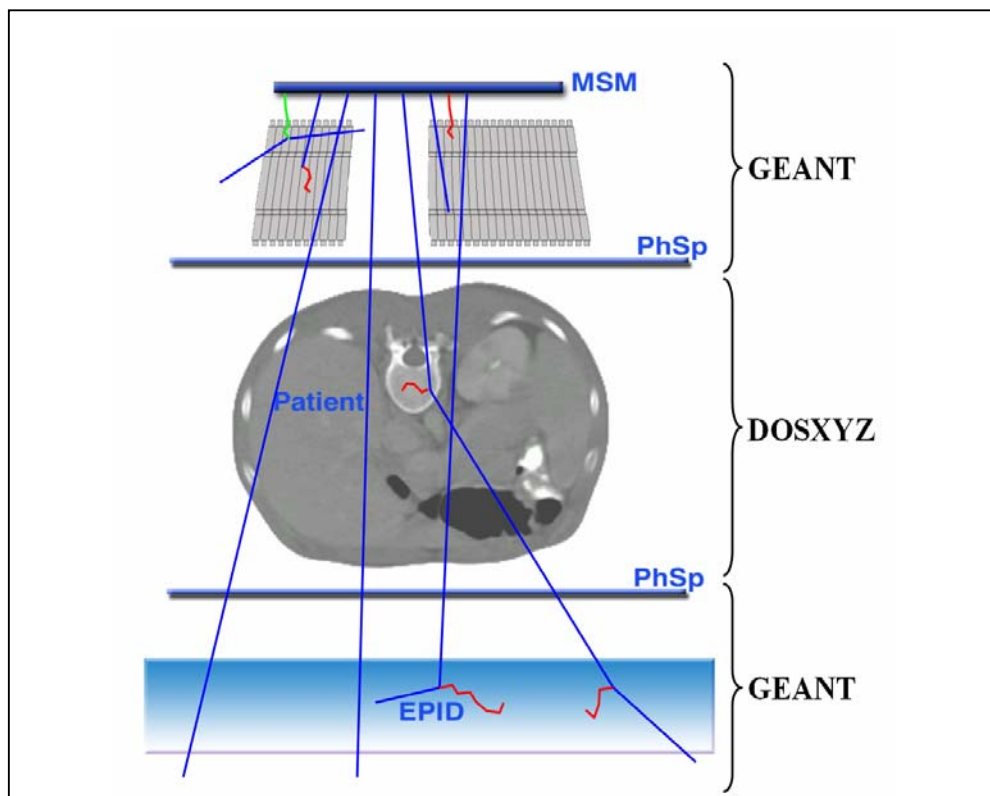


Figure 4.9 Schematic overview of the MC based calculation of a PDI for a real treatment. In a first step, GEANT provides phase space (PhSp) data at an output plane located directly behind the MLC. The radiation transport through the patient (represented by corresponding CT data) is performed by DOSXYZnrc leading to a second PhSp behind the patient. Finally, the PDI is calculated using GEANT.

account. This implies the necessity to import the patient's CT data set into the PDI calculation algorithm. By this means, the CT data is either accomplished from the treatment planning stage or by a separate CT scan at treatment time. The latter would be preferred due to being fully independent of the treatment planning process and allowing to assess potential inter-fractional changes in patient's anatomy.

The MC code DOSXYZnrc has been developed for calculating dose distributions in a rectilinear voxel phantom. This code is based on the EGSnrc MC code and thus is part of the OMEGA-BEAM system (Walters and Rogers 2002). In contrast to GEANT, DOSXYZnrc is capable of importing a CT data set of Hounsfield numbers and converting it to material density in each voxel using a corresponding calibration.

Figure 4.9 is a schematic overview of the processes involved to calculate a PDI for a real treatment situation. Initially, the GEANT-based MSM is used for the simulation of dynamically applied fields providing PhSp data directly below the MLC. This part of calculation is totally independent of the patient's geometry. Using these PhSp data as an input, DOSXYZnrc simulates the radiation transport through the patient. The DOSXYZnrc-based MC code provides further PhSp data in the portal plane. And finally, these PhSp data serve as an input for the GEANT-based MC simulations of the PDI.

The accuracy of the calculated PDIs is mainly determined by statistics. However, the method lacks of being very inefficient. In order to calculate a PDI of a dynamically applied field with 200 subfields with appropriate statistics, 2 Mio. histories per subfield were simulated with GEANT to generate the PhSp data below the MLC. The total CPU time required on an Alpha DS20E workstation (833 MHz) is about 24 h for a 6 MV beam. Note that the CPU time for a 15 MV beam is of the same order. This is due to the fact that for 15 MV there is a compensation of the increased number interaction processes and the decreased histories needed for the same statistical accuracy. For statistical purposes, the simulation of the radiation transport through the patient by DOSXYZnrc is replicated ten times by reusing the GEANT's output PhSp data ten times. The estimated CPU time required to simulate the corresponding PhSp output data is about 12 h. Finally, these PhSp data in the portal plane were used to calculate the PDI in a water phantom. As before, the PDI calculation reuses the PhSp data ten times for improving the statistics. This procedure takes about 240 h on an Alpha DS20E workstation (833 MHz). In the end, working in parallel mode on a powerful Alpha Cluster at our institute, a total simulation time of about 60 h turns up for one IMRT treatment field.

5

Measurement of Portal Dose Images

5.1 OVERVIEW

The general concept of IMRT verification in this thesis is based on the comparison between measured and calculated portal dose images (PDIs). In order to allow the a-Si:H based EPID for measurements of PDIs, the detector's pixel signal needs to be calibrated to dose values. The linear dose response relationship has already been shown in Chapter 2. However, due to changes of the radiation impinging the EPID introduced by changes of the delivery, the calibration procedure needs to be investigated for different clinical situations. In Chapter 3 it has been shown that the signal of the EPID is created by indirect detection. The use of a metal/phosphor screen combination is motivated by a suitable $DQE(f)$ for megavoltage portal imaging but also introduces problems for portal dosimetry purposes. For example, the question of water-equivalence is becoming evident if high-Z materials (such as Cu and $Gd_2O_2S:Tb$) are used in the detector system. Nevertheless, in order to enable the dosimetric verification of IMRT, the pixel signal needs to be calibrated to a water dose.

5.2 FIELD SIZE DEPENDENCE

As is well known in radiotherapy, the linac's output changes with different field sizes. Due to increased collimator scatter contribution at larger field sizes, the dose output grows with increasing field size (van Dyk 1999). In the literature, the corresponding quantity is called collimator scatter factor (or output factor) S_c and is defined as the ratio between the dose measured at a certain field size to the dose measured for a $10 \times 10 \text{ cm}^2$ field. In order to separate between collimator scatter factor S_c and in-phantom scatter S_p , the dose is measured in air (or a miniphantom) and in a water phantom, respectively.

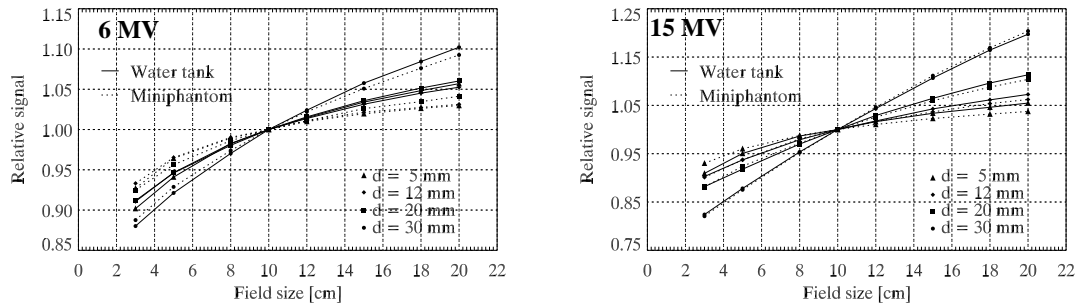


Figure 5.1 The difference of collimator scatter S_c and in-phantom scatter S_p is measured with two different water phantoms. Generally, the water tank ($50 \times 50 \times 40 \text{ cm}^3$) measurements show a stronger field size dependence than the miniphantom ($7 \times 7 \times 10 \text{ cm}^3$) measurements. This is caused by additional scatter in the increased volume of the water material (see text for more details).

Figure 5.1 shows the field size dependence of the in-phantom measured dose for two different water phantoms. The first phantom is built from a water tank with the dimensions $50 \times 50 \times 40 \text{ cm}^3$. The second phantom is a miniphantom with the dimensions $7 \times 7 \times 10 \text{ cm}^3$. The figure reveals the difference between the collimator scatter factor S_c and the in-phantom scatter S_p for 6 and 15 MV photon beams. As indicated above, due to the increased scatter contribution, the dose grows with increasing field size. In addition, due to the existence of more scatter volume, the water tank measurements show a stronger field size dependence than the corresponding miniphantom measurements. This difference is more pronounced at higher water depths where the difference of scatter volume is also more pronounced.

The field size dependence of the EPID's pixel signal together with corresponding water tank measurements are shown in Figure 5.2 and Figure 5.3 for 6 and 15 MV, respectively. For each field size, 100 MU are delivered with 200 MU/min and the pixel signals are averaged over a ROI of 9×9 pixels around the central axis. In order to investigate the indicated water-equivalence of the pixel signal, the water tank measurements are performed at different water depths d . From the figures it can be concluded that the signal of the PortalVisionTM aS500 depends strongly on the field size. The comparison to the measurements performed in the water tank shows best agreement for $d=5 \text{ mm}$ and $d=15 \text{ mm}$ for 6 and 15 MV, respectively. For both energies, these water depths are lower than the depths of maximum dose. Hence, in terms of field size dependence, the a-Si:H based EPID acts as a detector which is water-equivalent only in the buildup region. These results lead to the hypothesis that the a-Si:H EPID requires additional buildup material on top of the EPID to get a pixel signal

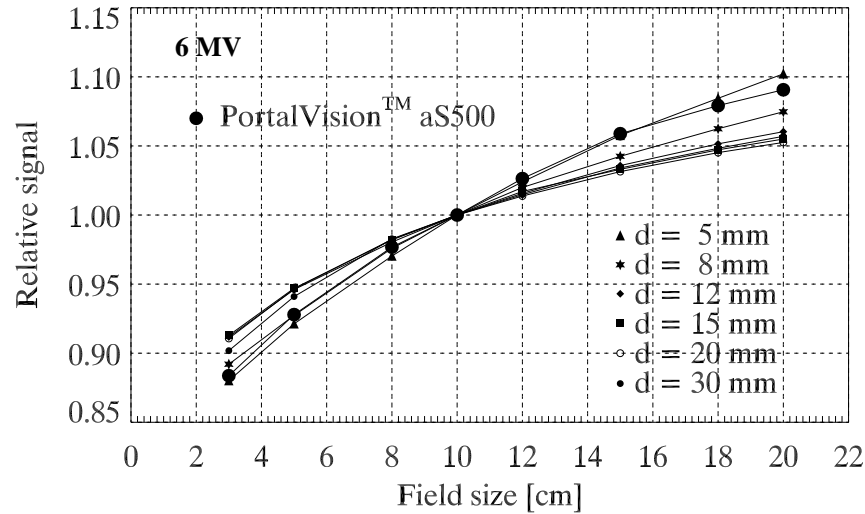


Figure 5.2 The field size dependence of the pixel signal and corresponding water tank measurements for 6 MV photon beams. Best agreement between the EPID and the water tank is achieved for a water depth d of 5 mm.

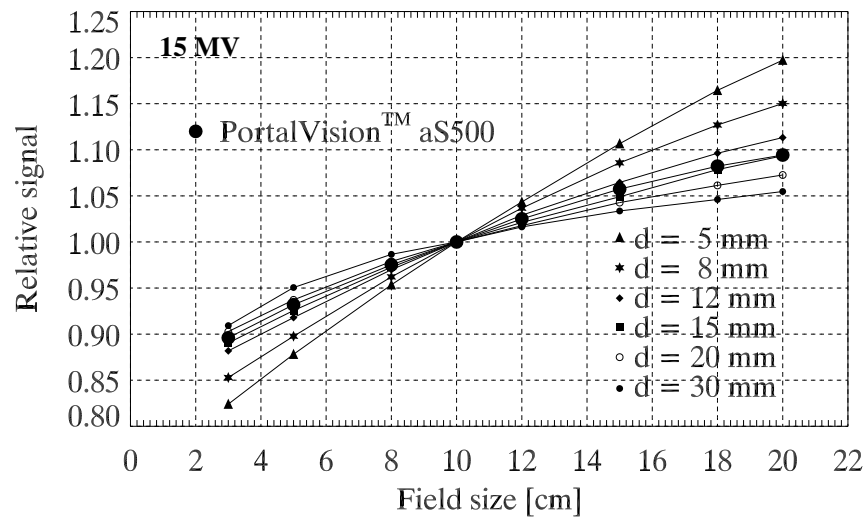


Figure 5.3 The field size dependence of the pixel signal and corresponding water tank measurements for 15 MV photon beams. Best agreement between the EPID and the water tank is achieved for a water depth d of 15 mm.

which is equivalent to water depths behind the buildup region. The same requirement has also been stipulated for the SLIC EPID (Boellaard *et al.* 1996). Notice that in this thesis, the additional buildup material consists of polystyrene

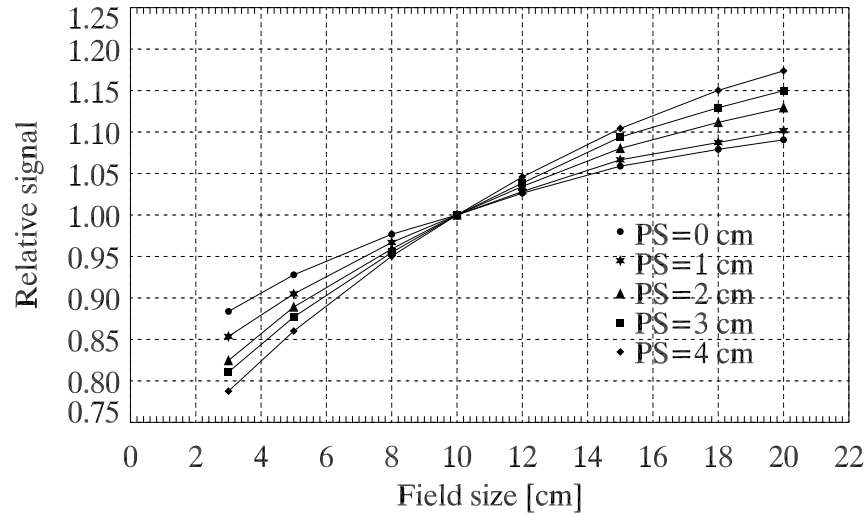


Figure 5.4 The impact of varying the thickness of additional buildup plates (PS) on the field size dependence shows that for 6 MV, the field size dependence is stronger with increasing the thickness of the buildup plate.

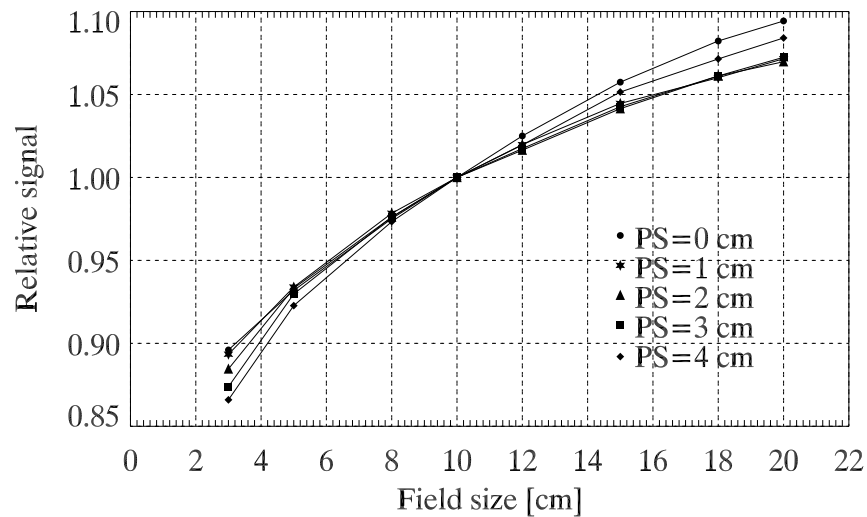


Figure 5.5 For 15 MV, the field size dependence weakens for thicknesses of additional buildup plates (PS) up to 2 cm, indicating that additional buildup plates lead to a corresponding water depth closer to d_{max} (cf. Figure 5.3).

(PS) plates with different thicknesses. These plates are loaded directly on top of the EPID's cover and not on top of the sandwich structure.

However, as shown in Figure 5.4 for 6 MV photon beams, the field size dependence of the EPID's pixel signal is stronger with increasing the thickness

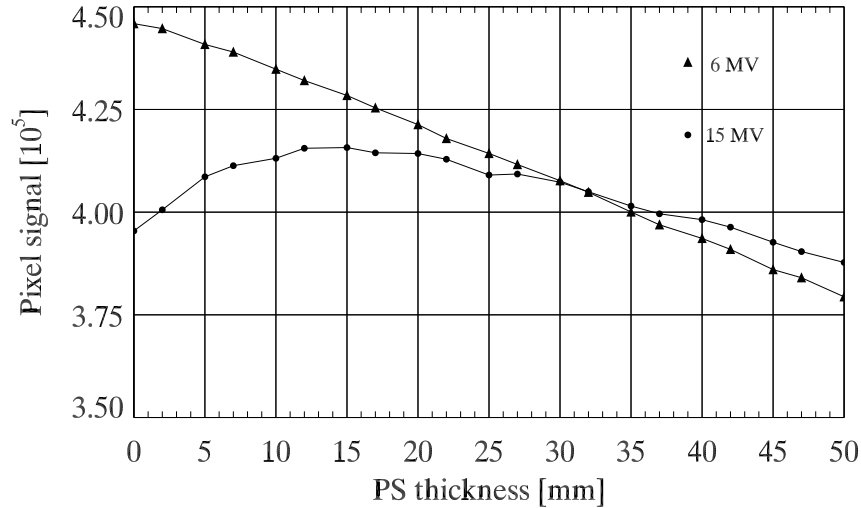


Figure 5.6 The dependence of the pixel signal as a function of the thickness of additional PS plates on top of the EPID's cover. Whereas for 6 MV the signal decreases with increasing PS thickness, the pixel signal exhibits a maximum at 15 mm for the 15 MV photon beam.

of the additional polystyrene (PS) plates. Hence, at least for 6 MV the PortalVision™ aS500 does not require any additional buildup material on top of the EPID. For 15 MV photon beams, Figure 5.5 shows that with increasing the thickness of the polystyrene plates up to about 1 cm the field size dependence declines, while thicknesses of more than 2 cm lead to stronger field size dependences.

In order to evaluate the dependence of the EPID's signal on the thickness of additional PS on top of the cover, measurements of the frame averaged pixel signal were performed. The corresponding results are given in Figure 5.6 from which it can be concluded that for 15 MV, the a-Si:H EPID requires some additional buildup plate with a thickness of 15 mm to get the highest signal. However, due to practical reasons, the accessory of an extra PS plate on top of the EPID is undesirable in a clinical point of view.

5.3 DOSE CALIBRATION OF THE EPID

In order to perform EPID dosimetry, a calibration of the EPID's signal is needed, which allows to convert the pixel signal to dose values in a reference system (water). Following this aim, the energy response of both systems, the EPID as well as the water reference system, needs to be investigated. For the EPID, the energy response has already been investigated in Chapter 3. In the same way, the

energy response of the water reference system is determined by the use of MC simulations. Therefore, a water phantom with the dimensions of $40 \times 40 \times 40 \text{ cm}^3$ is implemented in GEANT (cf. Figure 5.7) and the energy deposition in a plane perpendicular to the central axis is scored for monoenergetic pencil beams with different energies. The scoring plane is located at different water depths d ranging from 0.2 up to 50 mm.

The energy response of the water reference system is shown in Figure 5.8, demonstrating the effect of different water depths on the energy response. This effect is mainly driven by the same reasons, which are responsible for the well-known buildup effect: With increasing energy, the energy deposition in the scoring plane is accomplished by charged particles set in motion from lower depths. Hence, for a given depth of the scoring plane, this contribution begins to lack above a certain energy of the incident photons due to electronic disequilibrium (Johns and Cunningham 1983). As a consequence, the energy deposition starts to saturate and even decrease with increasing energy.

With the intention of dosimetric calibration of the a-Si:H based EPID, the energy responses for the EPID and for the water reference system are shown in Figure 5.9. In order to compare them, a normalization is performed such that each energy response equals one at a photon energy of 10 MeV. The different behaviors of the two detector systems are clearly visible. The EPID holds a high sensitivity to low-energy photons leading to a peak at about 50 keV and a local minimum at about 1 MeV. On the contrary, at least for low energies, the energy

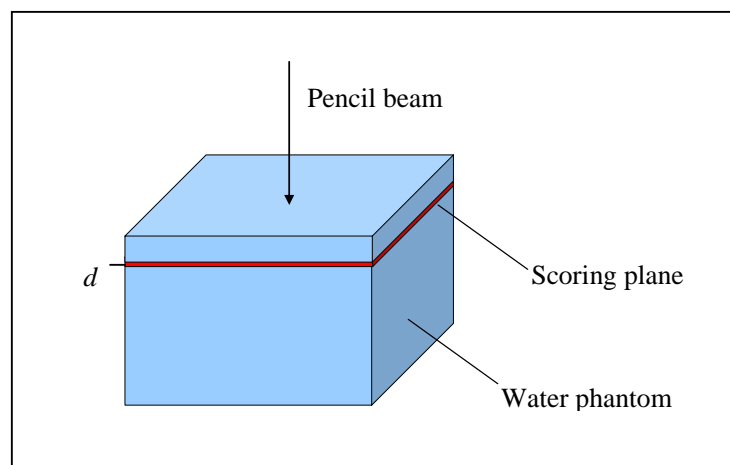


Figure 5.7 The water phantom as implemented into the MC code for simulating the energy deposition within water. In order to calibrate the EPID to a water dose the depth d of the scoring plane is variable.

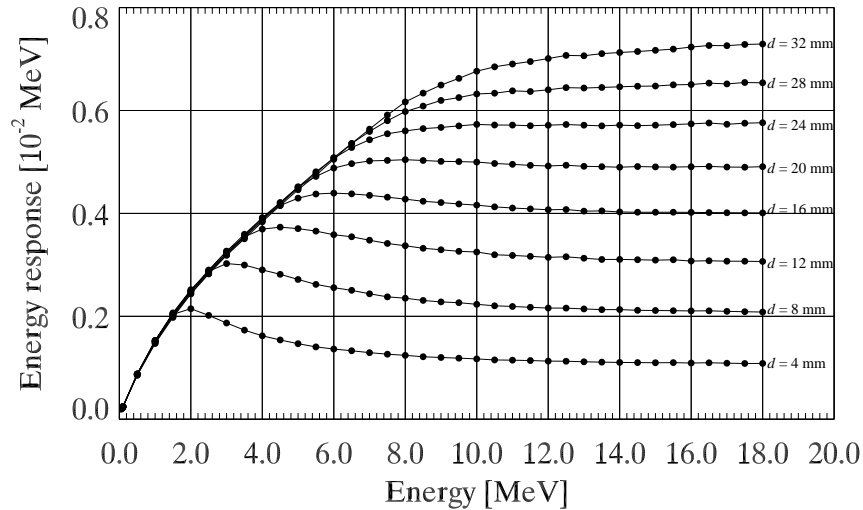


Figure 5.8 Energy response of the water detection system. The form of the energy response changes depending on the depth d in the water phantom. For low energies a linear growth occurs for the energy deposition with increasing energy of the incident photon pencil beam. According to the depth d the energy response is getting saturated or even decreases at higher energies. See text for more details.

response of the water system grows more or less linearly with energy. The different characteristics of the two energy responses are caused by different detector composition. As has been shown in Chapter 3, for low energies, the energy deposition in the phosphor layer of the PortalVisionTM aS500 is governed by the photo-electric effect, which is given by the high-Z of the Gd₂O₂S:Tb phosphor. However, determined by eye, the best agreement between the energy responses of the PortalVisionTM aS500 and the water reference system is achieved for a water depth of 24 mm. In this inspection, the distinct peak of the energy response for the a-Si:H EPID at low energies is not taken into consideration.

In order to calibrate the EPID signal to a water dose, the water depth d is not the only parameter to be changed. As has already been seen, the use of additional buildup material is another possible solution for better agreement between the pixel signal and the dose in water. For this purpose, the impact of using additional buildup plates (polystyrene) on top of the EPID is shown in Figure 5.10. As expected, the response to high-energy photons increases with increasing thickness of the PS plate. The figure demonstrates that the use of additional buildup plates has no effect on the energy response of photons with energies lower than 5 MeV. More details are visible on the right illustration of Figure 5.10, where the contributions of particles released in the PS plate are

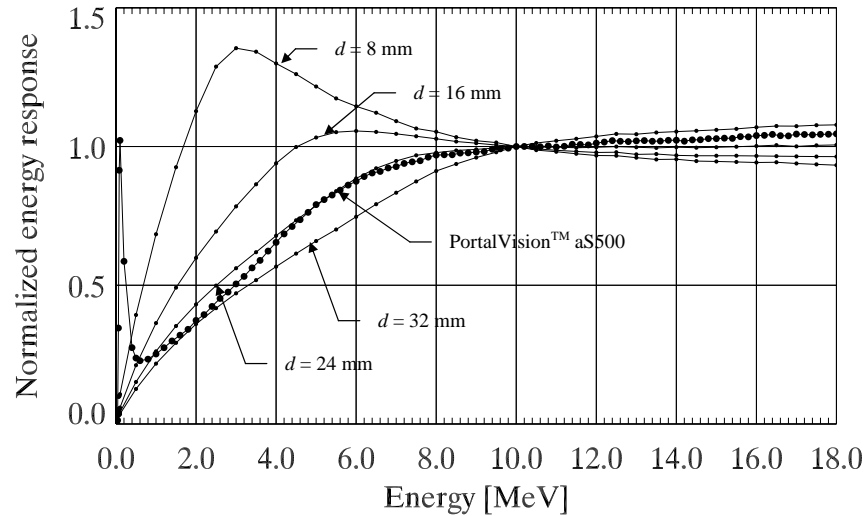


Figure 5.9 For calibration purposes the energy responses of the PortalVision™ aS500 and the water reference system need to be compared. Therefore, a normalization is performed at 10 MeV for both energy responses. The figure shows that best agreement is achieved for a water depth of 24 mm. However, the EPID's overresponse to low-energy photons is completely undiscoverable in the water reference system.

shown (cf. Chapter 3). Further investigations show that the increase of this PS contribution is caused mainly by particles, which interacted in the PS and the copper plate. Particles, which interact solely in the PS plate (and the phosphor layer, of course), are responsible for the differences observed at low energies. With growing thickness of the PS plate, the low-energy contribution is also increased. However, these low-energy differences are eliminated by corresponding, but contrary differences, which occur for the particles interacting

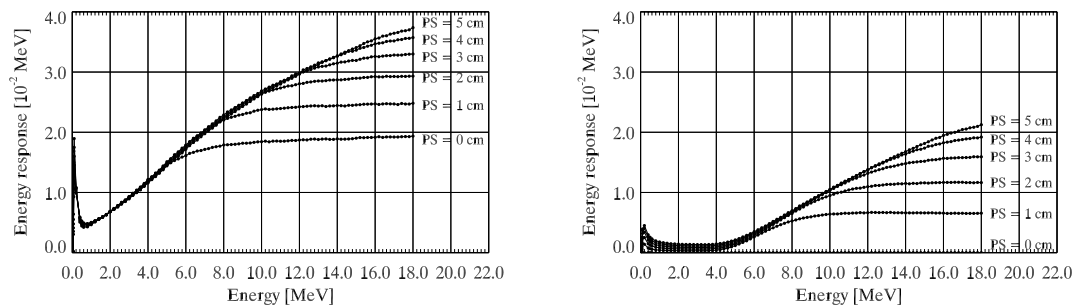


Figure 5.10 The energy responses of the PortalVision™ aS500 for different buildup plate (PS) thicknesses on top of the EPID. While the left figure shows the total energy response, the right figure shows only the energy deposition due to particles released within the PS layer. See text for more details.

solely in the phosphor layer (not shown). Overall, best agreement is achieved for the situation, where no additional buildup material ($PS = 0$ cm) is used and a water depth of 24 mm is chosen.

For portal dosimetry by the use of an EPID, not only the energy responses, but also the form of the energy deposition kernels needs to agree for the two detector systems. The energy deposition kernel $e_k(x, y, z)$ is defined as the energy deposited at the point (x, y, z) due to an incident pencil beam at the origin $(0, 0, 0)$.

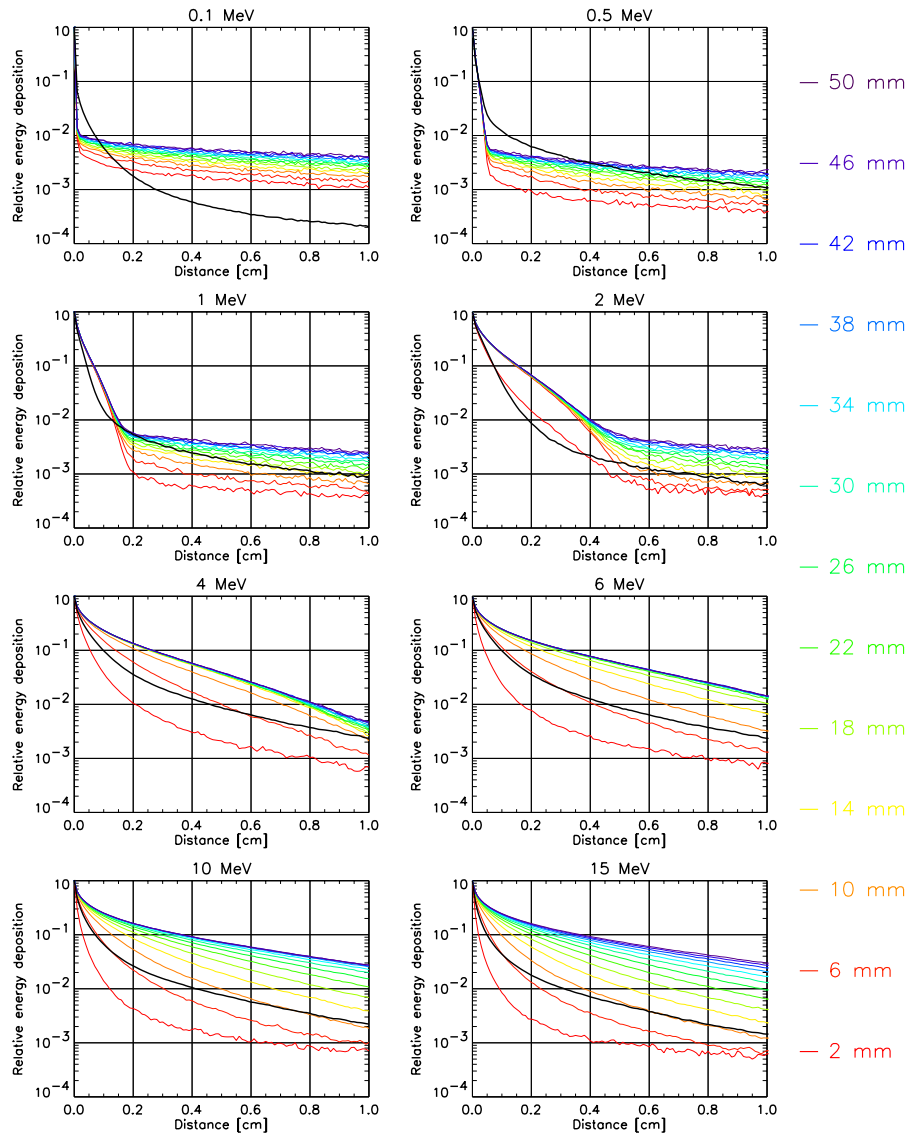


Figure 5.11 Relative energy depositions as a function of the lateral distance (point-spread functions) for the a -Si:H EPID (black curve) and water (colored curves) at different water depths. Depending on the initial photon energy, the point-spread functions of the two systems agree best at different water depths.

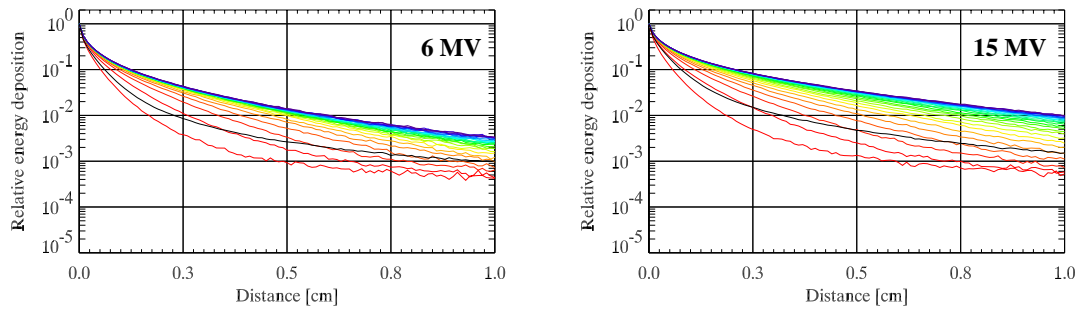


Figure 5.12 Point-spread functions for polyenergetic photons of the a-Si:H EPID (black curve) and the water (colored curves) at different water depths. Best agreement is achieved for water depths of 10 mm for 6 MV and about 15 mm for 15 MV, respectively.

Hence, the energy response corresponds to the integral of the energy deposition kernel over the whole scoring plane. Figure 5.11 shows the lateral distribution of the energy deposited in the phosphor layer (no additional PS on top of the EPID) and in water for a scoring plane at different water depths. In these simulations, the energy deposition is scored in voxels with the dimensions of $1 \times 1 \times 0.5 \text{ mm}^3$. As in the investigations on the energy response, the largest discrepancy turns up at low photon energy, where scattering is more pronounced in the water reference system. The figure demonstrates that these scatter properties depend critically on the water depth d . While for the comparison between the energy responses a water depth of 24 mm has been suggested (cf. Figure 5.9), this would not be a suitable choice in terms of lateral spread of the energy deposition. This is explained by the fact, that the peak arising in the energy response of the a-Si:H EPID at very low energies has been disregarded for the proposal of the 24 mm water depth.

Thus far, only monoenergetic photon beams are considered. But in real world, a linac is used for the delivery of IMRT fields, which means that polyenergetic beams are used. Consequently, the calibration of the EPID's signal to water dose values is not a matter of investigations on monoenergetic beams but needs to be performed for realistic treatment situations. As an example, Figure 5.12 shows lateral energy distributions for two pencil beams with energy spectra of 6 and 15 MV, respectively. In terms of the lateral spread, best agreement between the EPID and the water reference system is achieved for a water depth of 10 mm and 15 mm for 6 and 15 MV, respectively. This corresponds more or less to the measurements performed in Section 5.2, where the field size dependence is investigated.

5.4 ACQUISITION OF A PDI FOR DYNAMICALLY APPLIED FIELDS

As every EPID, the PortalVision™ aS500 acts mainly as an imager and is therefore intended to provide information about anatomical structures for patient setup purposes. With this intention, the EPID acquires portal frames during a short time while the beam is on (typically 1-4 MU is applied for a portal image). Portal dose image acquisition for a static field works more or less in the same way. For relative dosimetry, it is sufficient to measure the portal dose during a certain period of the full application. This is in contrast to the situation where dynamic deliveries are to be verified. In this case, the intensity is a continuous function of time, which leads to the demand to measure the portal dose distribution during the full treatment delivery. The standard acquisition mode (for portal imaging) can't be used for the measurement of a PDI, which makes the development of a special acquisition mode necessary.

The readout scheme of the EPID has been described in Chapter 2. Basically, the TFTs control the readout on a row-by-row basis. Typical frame rates are in the order of about 10 frames per second. The standard image acquisition is connected to the beam delivery system such that the start of the image acquisition is triggered to the first beam pulse. Analogously, the image acquisition stops if the beam is disabled. During the time between the start and the end of the image acquisition, frames are acquired continuously and the corresponding information is stored in a frame buffer. However, due to limited storage space (20 bit) of the frame buffer, only 64 frames (each of which with 14 bit) can be stored. After this, the frame buffer's content needs to be moved to another memory storage before it is emptied. This data transfer requires a time of about 160 ms during which the pixel's photodiode detects photons from the beam delivery but the corresponding charge generated is not readout. This means that the next frame to be read out would have an extra amount of information compared to the 64 frames just acquired before. That is the reason why in standard image acquisition the readout process causes to drop this specific frame. For portal imaging purposes, where the image acquisition takes place only in a very short time, this drop of a frame does not affect the quality of the image. The same is true for (relative) dosimetric verification purposes of static fields or IMRT delivered by the step-and-shoot technique. Even if the beam delivery causes the EPID to acquire more than 64 frames, the image is not influenced by dropping a frame since every frame looks the same. But for the verification of dynamically applied fields (DMLC) this frame dropping needs to be prevented since the intensity distribution changes with time. Note that in DMLC deliveries, the dose for a certain point (x,y) in the portal plane is mainly given by the opening density, which is defined as the time

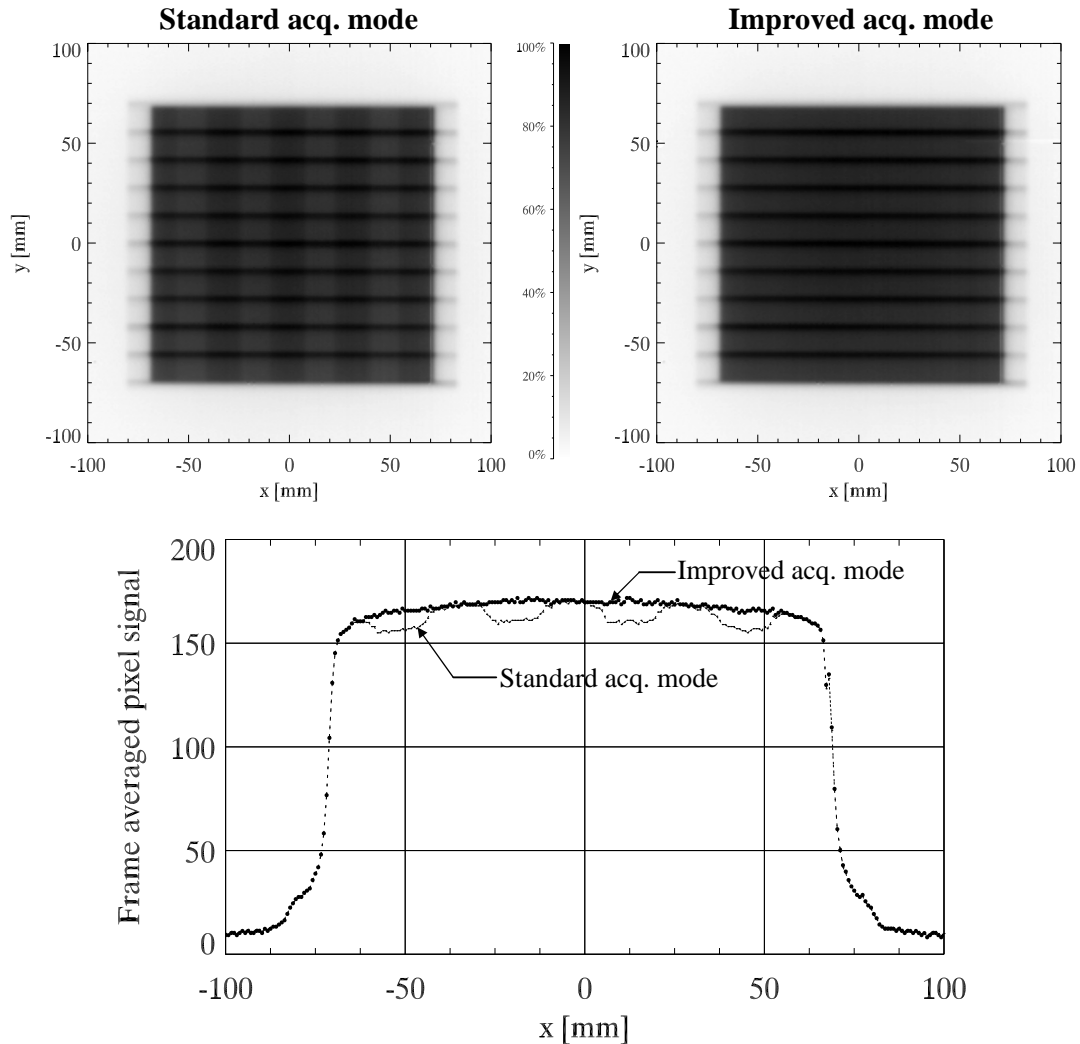


Figure 5.13 Improvement of the measurement of PDIs for a uniform $10 \times 10 \text{ cm}^2$ field delivered with a dynamic slit beam incorporating a slit gap width of 1 cm. The PDI obtained with the standard acquisition mode (left) differs severely from the one measured by the improved acquisition mode (right). The comparison between portal dose profiles along the leafmotion direction shows that due to dropping one frame after each 64th frame, the dose decreases dramatically at the corresponding positions. This loss of information is completely avoided for the improved acquisition mode.

during which this point “sees” the beam source (Mohan *et al.* 2000). In dynamic IMRT deliveries, it is possible that the dose at the point (x,y) is delivered in a very short time period. If now the portal image acquisition is such that during this specific time period the frame buffer data needs to be transferred, then the entire dosimetric information for the point (x,y) is lost.

In order to overcome this ‘frame dropping problem’ a new acquisition mode has been developed, where no frames are dropped at all. Furthermore, an

improvement of the acquisition of the last frame is achieved by reading out the last frame two times (Manser *et al.* 2002b).

The improvement of the new acquisition mode is clearly visible from Figure 5.13, where two portal images are compared. For both images, a dynamic slit beam (see next Section) is delivered with a slit gap width of 1 cm. Overall, 100 MU (at a repetition rate of 200 MU/min) are delivered with a 6 MV photon beam resulting in a beam delivery time of about 30 s. In this time, the EPID acquired about 300 frames. Thus, the problem of frame dropping indicated previously occurs for four times since after every 64th frame, dose information is lost. The figure demonstrates that exploiting the features of the EPID for portal dosimetry of intensity modulated beams is only ensured if all dose information is captured during the delivery.

5.5 DYNAMIC SLIT BEAM DELIVERIES

In order to benchmark the performance of the EPID for dosimetric purposes, dynamic slit beam deliveries are created. The principle of such a delivery is outlined in Figure 5.14 for a 1 cm wide slit gap moving from left to right with constant speed. The speed v of one leaf is determined by the total distance w traveled by the leaf and the total beam-on time T , which on its own part is given by the total dose D and the dose rate \dot{D} :

$$v = \frac{w}{T} = \frac{w}{D/\dot{D}}.$$

The intensity I delivered to a certain point x_0 is directly related to the opening density (i.e. the time during which the point x_0 ‘sees’ the source). From the figure it can be derived that the intensity I (in MU) is related to the slit gap width s as follows:

$$I = \frac{s}{w+s} \cdot T = \frac{s}{w+s} \cdot \frac{D}{\dot{D}}.$$

However, due to transmission through the MLC, the real intensity at a certain point x_0 is augmented by an intensity I_{MLC} . Given that the transmission through

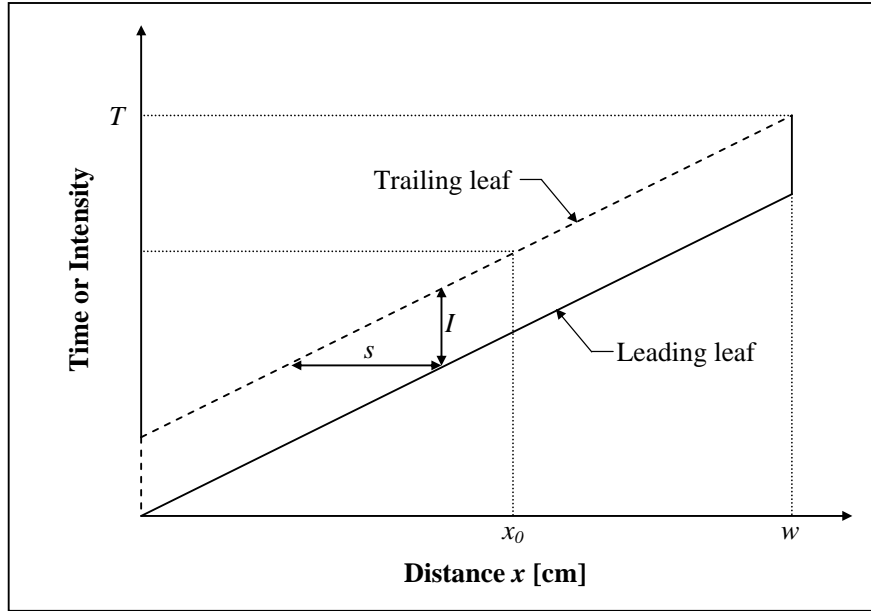


Figure 5.14 Schematic illustration of the principle of dynamic slit beam deliveries. A uniform field over the distance w and with the intensity I is delivered by moving slits with a slit gap width s .

the MLC is constant in space, I_{MLC} is directly determined by the time during which the point x_0 'sees' no source and the transmission factor τ_{MLC} :

$$I_{MLC} = \left(T - \frac{s}{w+s} \cdot T \right) \cdot \tau_{MLC} = \frac{w}{w+s} \cdot T \cdot \tau_{MLC}.$$

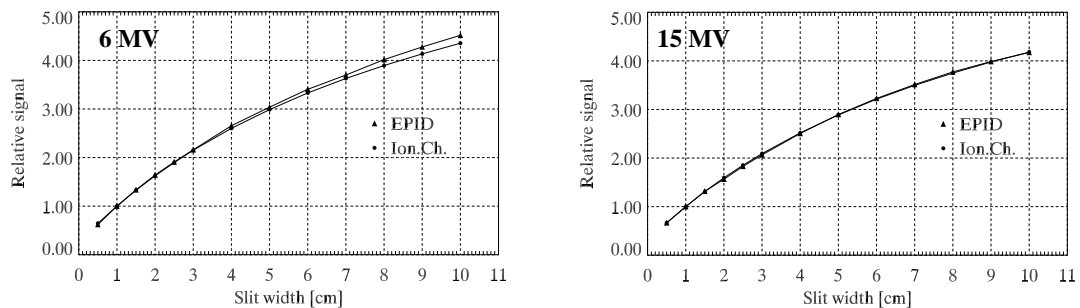


Figure 5.15 Measurements showing the dependence of the intensity I on the slit gap width. Based on theoretically derived equations, the transmission through the MLC can be determined to 3% and 3.5% for 6 and 15 MV, respectively. The figure demonstrates the different behaviors of the measurements performed with the α -Si:H EPID and with an ionization chamber. While for 15 MV hardly any difference occurs, the overresponse of the EPID's signal is becoming obvious for 6 MV at large slit gap widths.

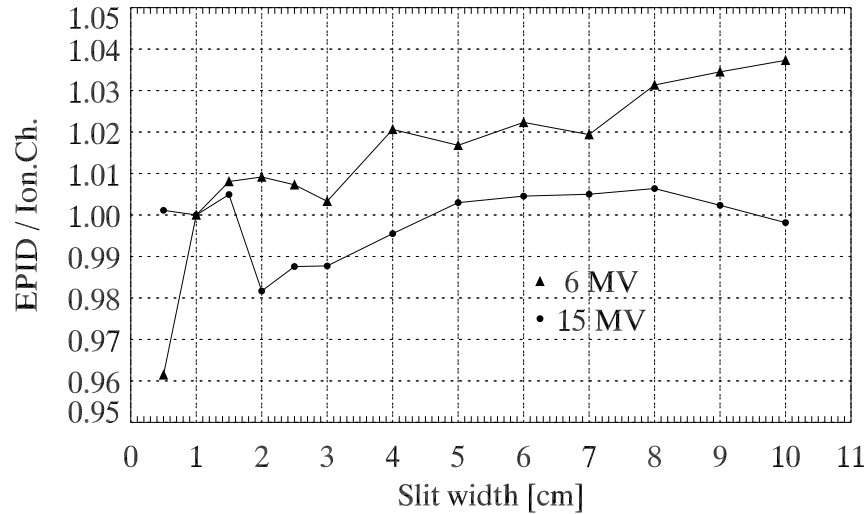


Figure 5.16 Dependence of the ratio between the EPID signal and the ionization chamber reading on the slit width for 6 and 15 MV photon beams. The 6 MV case reveals that with increasing slit width, the ratio increases, whereas for 15 MV no dependence on the slit width is observed.

Typically about 3% of transmission occurs for the MLC used in this thesis. The equation demonstrates the effect of additional intensity I_{MLC} introduced by MLC transmission. With increasing slit gap width s , the importance of the transmission through the MLC decreases.

The dependence of the intensity I on the slit gap width s is shown in Figure 5.15. The measurements were performed with the a-Si:H EPID and ionization chamber measurements. For the EPID, the average of the pixel signals over a region of 9×9 pixels around the central axis is built. The ionization chamber measurements are performed by the use of a miniphantom (see Section 5.2). In order to compare the ionization chamber measurements to the EPID signals, the signals are normalized to a slit gap width of 1 cm. From the figures, a transmission of 3% and 3.5% is calculated for 6 and 15 MV, respectively, by fitting the data to the equations indicated above. In addition, particularly for 6 MV, the figures demonstrate the different behavior of the measurement systems. While for 15 MV hardly any difference occurs, the EPID's signal shows an overresponse with growing slit gap width for 6 MV photon beams.

This is shown in more detail in Figure 5.16, where the ratio between the EPID's signal to the ionization chamber reading is plotted versus the slit gap width. Again, a normalization at a slit gap width of 1 cm is applied. Obviously, the ratio is more or less constant for the 15 MV photon beams. On the other

hand, the 6 MV case shows an increase of the ratio with increasing slit gap width. Note that in these measurements the ionization chamber was located in 3 cm and 5 cm for 6 and 15 MV, respectively. Thus, the dependence of the ratio on slit gap width is hardly influenced by electron contamination but is assumed to be governed by spectral changes caused by the dynamic delivery of the fields.

5.6 SPECTRAL CHANGES CAUSED BY DMLC

The dynamic delivery by an MLC (DMLC) is based on the sliding-window technique (see Chapter 1). In principle, the gap between a leafpair is moving over the tumor region, whereby the width of the gap as well as the speed of the leaves are changing with time. For a realistic treatment delivery of a head and neck carcinoma, Figure 5.17 shows the variation of the gap widths for one treatment field. Depending on the smoothness of the intensity distribution, different leaf gap widths arise. However, with varying slit gap widths, the scatter contribution by the MLC and consequently the photon energy spectrum change. Therefore, detailed knowledge of the impact of DMLC deliveries on the photon energy spectra is essential for calibration purposes of the EPID (Manser *et al.* 2002c).

Based on the multiple source model (MSM, see Chapter 4) and its supplemented MLC model, energy spectra are simulated for different dynamic slit beam deliveries with different slit gap widths ranging from 0.25 up to 4 cm

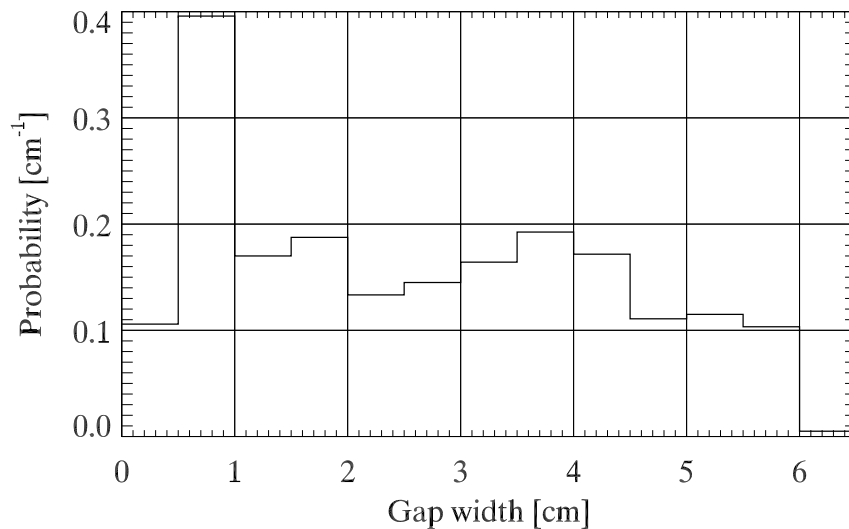


Figure 5.17 Histogram representation of the distribution of the slit width for a typical treatment field delivered dynamically by the sliding-window technique. The variation of these slit gap widths has an impact on the photon energy spectrum delivered by the linac.

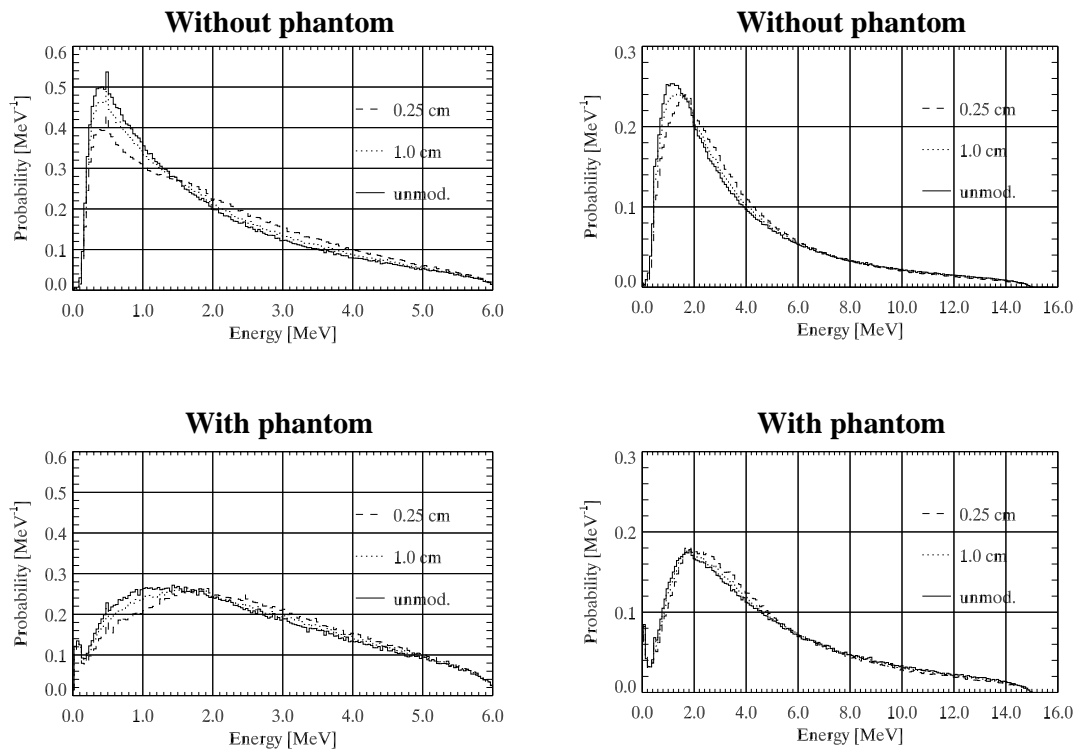


Figure 5.18 Energy spectra for 6 and 15 MV photon beams with and without a phantom in the beam. In every situation, spectral changes occur due to changes of the slit width.

and for an unmodulated beam. Each slit beam irradiation consists of 150 subfields delivering a $13 \times 20 \text{ cm}^2$ field. In order to study the influence of a patient on the energy spectra in the portal plane, a water phantom (with the dimensions of $30 \times 30 \times 25 \text{ cm}^3$) is placed in the beam at an SSD of 75 cm. Finally, the photon energy spectrum is scored at different portal planes perpendicular to the central axis at distances of 100, 110, 120, 130, and 140 cm from the target.

For 6 and 15 MV, Figure 5.18 shows the energy spectra for a distance of 140 cm from the target. The normalization is such that the area under the spectrum equals one. The effect of beam hardening is clearly visible from the figure. The smaller the gap between two leafpairs, the more apparent is the beam hardening. Although weakened, this effect is still evident if a phantom is in the beam. Note that all these spectral changes are less pronounced for the 15 MV case.

As shown in Figure 5.19, the energy spectra depend critically on the airgap distance between the phantom and the portal plane. With increasing airgap

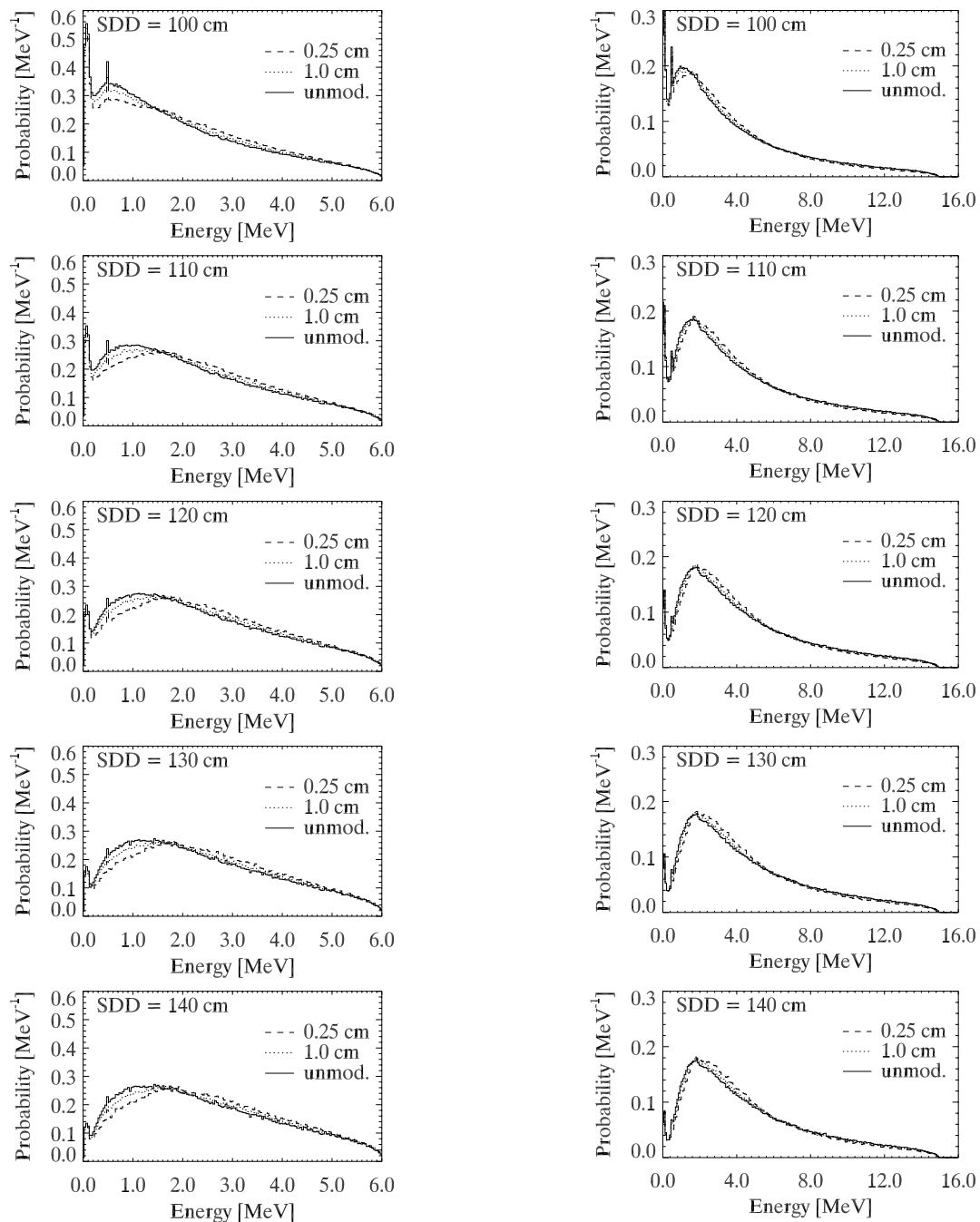


Figure 5.19 Energy spectra for 6 and 15 MV photon beams for different portal planes (SDD=110, 120, 130, and 140 cm). Depending on the slit width and the SDD, spectral changes occur.

distance, the photons scattered by the phantom are less likely to be detected due to wider angular distributions (Jaffray *et al.* 1994). As a consequence, the contribution of low-energy radiation is reduced with increasing airgap distance. In addition, the differences in energy spectra due to different slit gap widths are weakly decreasing for increasing airgap distances.

5.7 IMPACT OF SPECTRAL CHANGES ON EPID DOSIMETRY

As has been indicated previously, the energy spectrum depends critically on the treatment delivery (e.g. slit gap width of a dynamically applied field). In the following, the impact of these spectral changes on the EPID calibration is investigated. For this purpose, the changes in photon spectra caused by dynamic slit beam deliveries are combined with the different energy responses of the EPID and the water reference system. For the EPID, a signal G_{EPID} is calculated based on its energy response $\overline{E_{resp}^{EPID}}(E)$ to monoenergetic pencil beams and the energy spectrum $\varphi(E)$ of the incident photon beam by

$$G_{EPID} = \int_0^{E_{max}} \varphi(E) \cdot \overline{E_{resp}^{EPID}}(E) \cdot dE$$

A corresponding signal G_{WAT} is calculated for the water reference system.

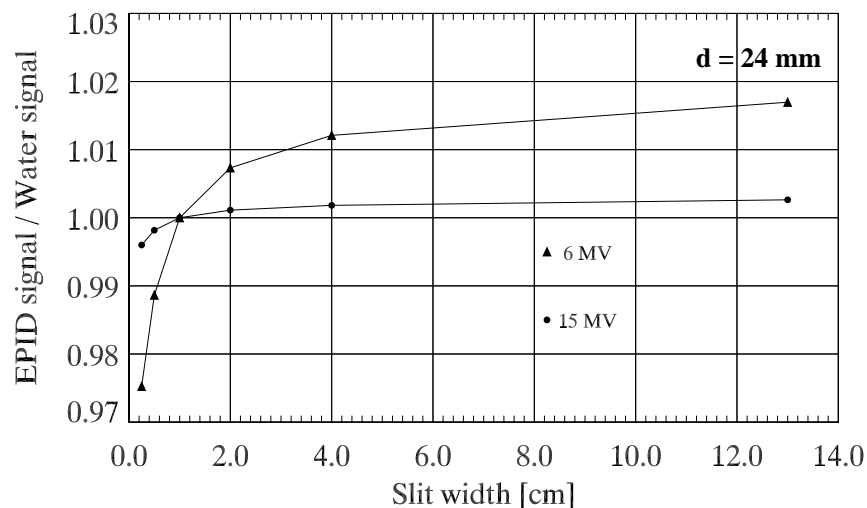


Figure 5.20 Calculated ratio between the EPID signal and the water signal as obtained from the MC simulations of the energy responses and of the spectral changes due to changes of the slit width.

Herewith, if the EPID needs to be calibrated to a water dose, then the ratio between these two signals needs to be analyzed. In the following, this ratio will be investigated for different situations. As derived from the comparison between the energy responses of water and the EPID, a water depth of 24 mm will be taken as a first approach. Note that although this preliminary fixing corresponds to the best agreement between the two energy responses, it is not expected to be the best choice due to the disregard of the EPID's overresponse to low photon energies.

For the pre-treatment situation, where no phantom is in the beam, Figure 5.20 shows the ratio of the EPID's signal G_{EPID} to the water signal G_{WAT} as a function of the slit gap width. Note that the dependence of this ratio on the slit gap width originates from the spectral changes caused by the dynamic MLC delivery (cf. Figure 5.18). The ratio between the signals is normalized to a slit gap width of 1 cm. Depending on the initial energy of the incident photon beam, differences of up to 3% appear. This is of the same order as the results from measured ratio by using slit beam deliveries (see Section 5.5). Hence, from these MC investigations it can be concluded that the different behaviors of the ionization chamber and the EPID are due to a combination of different energy responses and different energy spectra.

In Figure 5.21, the corresponding results for the treatment situation are given for an SDD of 140 cm. For these simulations, a water phantom ($30 \times 30 \times 25 \text{ cm}^3$)

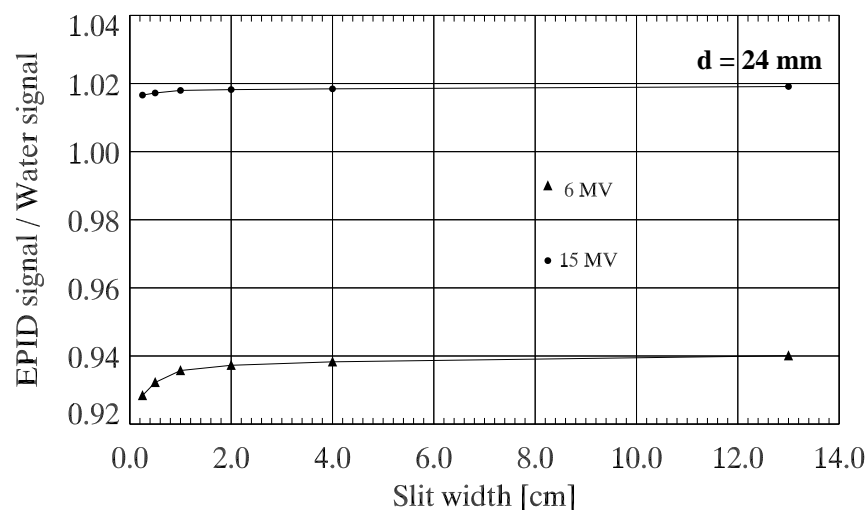


Figure 5.21 Ratio between the EPID and the water signal for the treatment situation ($SDD=140 \text{ cm}$). The spectral changes due to the existence of a phantom in the beam have an impact on the ratio.

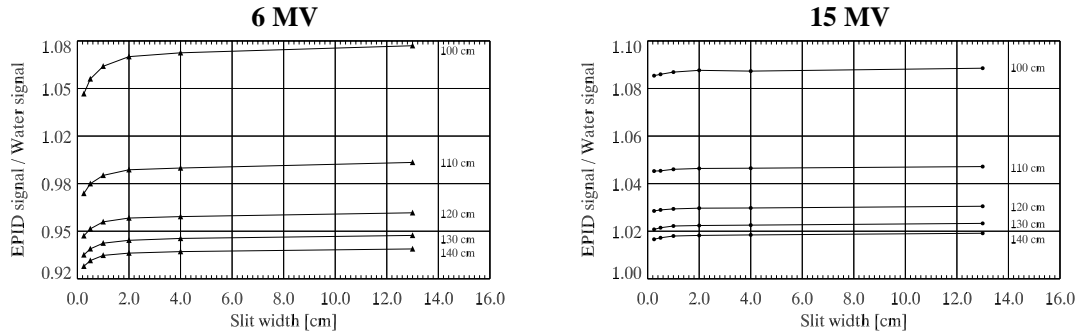


Figure 5.22 Ratios between the EPID and water signal for 6 and 15 MV photon beams. The figure demonstrates that for different SDDs different calibrations are to be applied for portal dosimetry.

is placed in the beam ($SSD=75$ cm). Note that the ratio of the EPID's signal G_{EPID} to the water signal G_{WAT} is normalized to the pre-treatment situation. This is how typically EPIDs are calibrated in clinical routine: For the pre-treatment situation, the EPID's signal is associated with a certain dose value for a reference situation (e.g. a dynamic slit beam delivery with a slit gap width of 1 cm). If now a patient is in the beam, the same calibration is used. However, by doing this, Figure 5.21 reveals errors of up to 8% and 2% for 6 and 15 MV, respectively. These errors are introduced by energy spectrum changes due to the presence of the water phantom. Bearing in mind, that these changes are more severe for 6 MV (cf. Figure 5.18), the higher error for this photon beam energy is not surprising. However, the fact that with the presence of a water phantom, the ratio of the two signals is decreased for 6 and increased for 15 MV, respectively, is a consequence of the combination between the spectral changes and the different energy responses. If for the treatment verification, a separate calibration is performed (e.g. such that the EPID's signal is associated with the water signal for a dynamic slit delivery with a slit gap width of 1 cm), then the corresponding errors are of the order of 1%. Hence spectral changes due to different slit gap widths are not so severe, if a phantom is in the beam.

However, as shown in Figure 5.22, this depends critically on the airgap distance. The larger the airgap distance, the weaker the differences in the spectral changes with varying slit gap widths, which leads to a weaker dependence on the slit gap width for the ratio of the EPID's signal and the water signal. Additionally, the figure demonstrates that if no separate calibration for the treatment situation is applied, the corresponding errors depend on the airgap distance. While for 15 MV, these errors increase with increasing airgap distance, the 6 MV case seems to have an optimum SDD of 110 cm.

As was indicated previously, the predefinition of using 24 mm water depth as a standard for calibration is questionable. The spectral changes have therefore also to be investigated for different calibration parameters (such as the water depth). As before, the ratio between the EPID's signal G_{EPID} to the water signal G_{WAT} is analyzed. This leads to the result that for 6 MV, a water depth of 4-6 mm is suitable, for 15 MV a water depth of 15 mm is appropriate. Note that these results are in full agreement to the results obtained from the experiments presented earlier in this Chapter.

In conclusion, the pixel signal of a-Si:H EPID can be related to a water dose in the buildup region. Water depths of 4-6 mm for 6 MV and 15 mm for 15 MV are suitable for EPID dosimetry.

5.8 PDIS OF CLINICALLY RELEVANT TEST FIELDS

In the following, measured PDIs are presented for the same clinical relevant fields, which were already used in Chapter 4. In order to compare the accuracy and efficacy of the EPID for its application in dosimetric IMRT verification, radiographic film (Kodak X-Omat V) measurements were also performed. For this purpose, the films were calibrated against optical density. As an integrating dosimeter, the film calibration is carried out by exposing films to known doses under reference conditions. After development, the optical density is determined

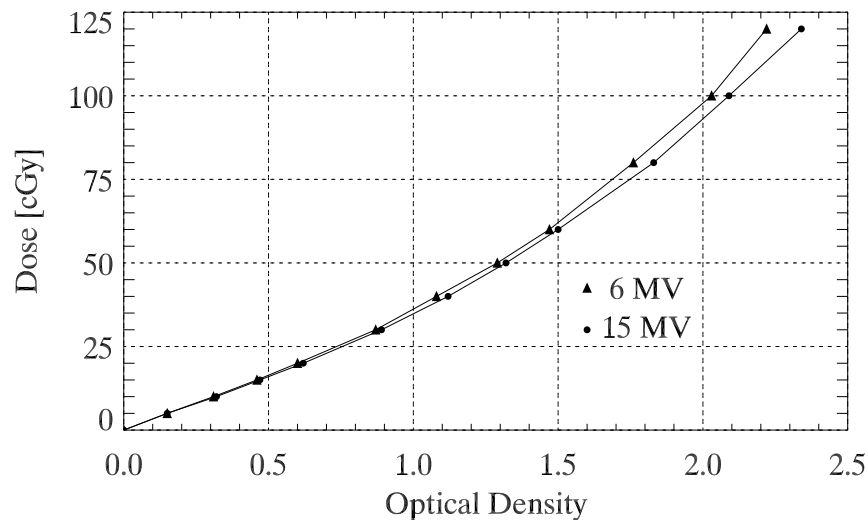


Figure 5.23 The calibration curve of the radiographic films (Kodak X-Omat V). Film measurements were performed to compare the accuracy and efficacy of films and the EPID for portal dosimetry. The figure demonstrates that linearity of the film response is fulfilled only within a limited range of dose.

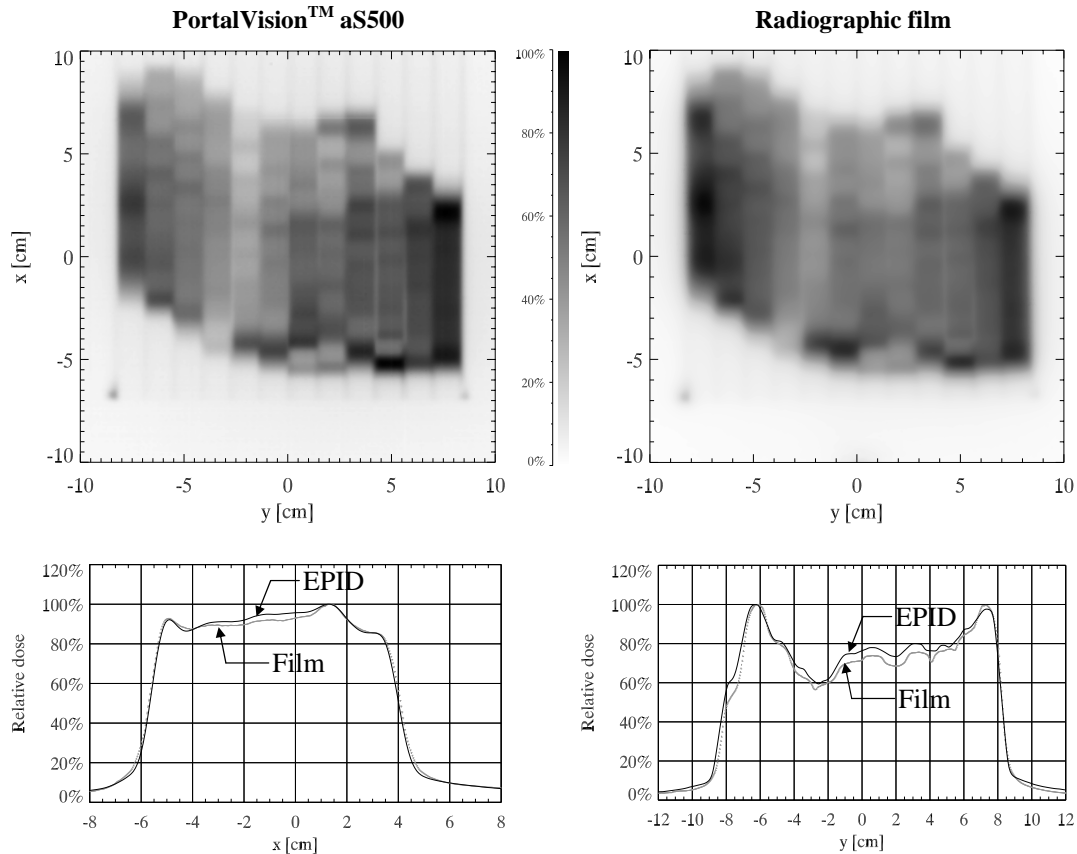


Figure 5.24 Measured portal dose images (PDIs) by the EPID and film dosimetry for one field of a head-and-neck treatment using a 6 MV photon beam. The agreement is of the order of 3-4% and shows the suitability of the EPID to measure PDIs for dynamically applied fields.

by the use of a 16-bit digitizer VXR-16 (Vidar Systems Corporation, Herndon, VA). In order to prevent problems due to variations in the sensitivity, all films belonged to the same batch. Figure 5.23 shows the calibration curve for 6 and 15 MV photon beams. The dose response linearity is given for quite low doses only.

The first intensity modulated field investigated is obtained from an optimized IMRT plan for a realistic head and neck carcinoma. The field considered is a 6 MV photon beam delivered by the sliding-window technique. For the pre-treatment situation, the corresponding PDIs measured by the EPID (left) and by radiographic film (right) are depicted in Figure 5.24. In addition, dose profiles are given along (x) and across (y) the leafmotion direction, respectively. For an SDD of 140 cm, the agreement is about 3-4% and 4 mm. This is also seen from Figure 5.25, where isodose curves are plotted.

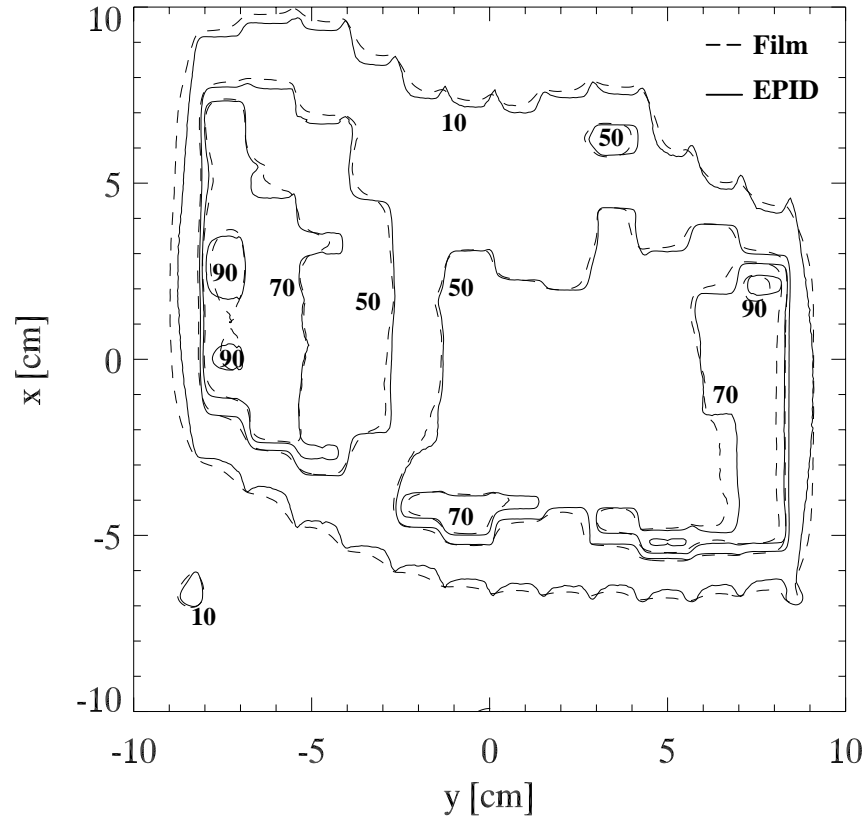


Figure 5.25 Isodose plots for the head-and-neck IMRT treatment field of the EPID (full curves) and film (broken curves) measurements.

With the intention to imitate a real treatment, a phantom consisting of solid water plates and inhomogeneities built from air and bone was placed in the beam (cf. Figure 4.3). As before, PDIs were measured by the EPID and by radiographic film in a plane with a distance of 140 cm from the target. The results are given in Figure 5.26 illustrating the decreased portal dose in the region where the bone material is located. The comparison between the dose profiles results in an agreement of about 3% and 4 mm.

Using 15 MV photon beams, another realistic case (bronchus carcinoma) was investigated. As in the head and neck case, the inhomogeneous phantom was engaged to simulate a patient. The Figure 5.27 shows the PDIs as well as the dose profiles obtained from EPID measurements and film dosimetry. The agreement is in the order of 3% and 4 mm.

The treatment fields considered in this section were obtained from inverse treatment planning using CadPlan (Varian Medical Systems). The sliding-window technique was employed for the delivery of these fields on a Varian

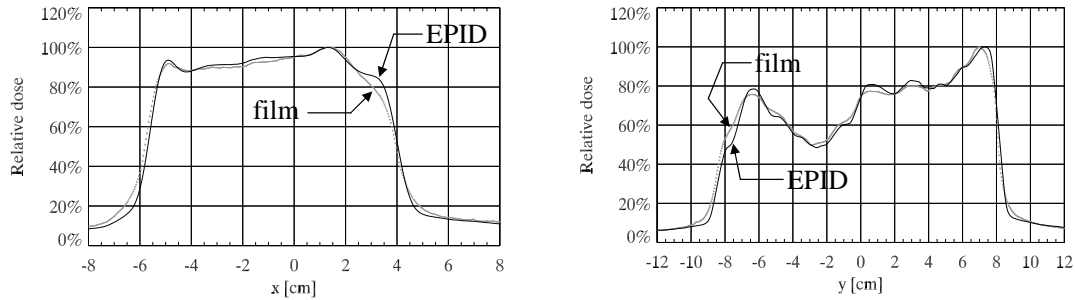


Figure 5.26 Comparison of dose profiles for the treatment verification using an inhomogeneous phantom (cf. Figure 4.3) along the x - and y -direction, respectively. The measurements were performed by the EPID and film, respectively. The agreement is in the order of 3% and 4 mm.

Clinac 2300 C/D. The results demonstrate the suitability of using the EPID's improved acquisition mode to measure portal dose distributions very efficiently. Essential to this improved acquisition mode is the principle of frame averaging which requires that the linearity is fulfilled. As has been shown in Chapter 2, saturation of the pixel signal starts at doses higher than 1.7 cGy in the isocenter plane (cf. Figure 2.6). Using the improved acquisition mode for measuring a PDI (cf. Section 5.4), the highest dose per frame is given by the time needed to acquire a frame (typically 100 ms) and by the extra time of 160 ms needed to move the data in the frame buffer to the image buffer. As a consequence, dose rates exceeding 390 cGy/min in the isocenter plane would lead to saturation effects and would not be appropriate for portal dosimetry.

As indicated previously, saturation is an issue for film dosimetry. The radiographic film is an integrating device and therefore not the dose *rate* but the total dose is responsible for saturation effects. Usually, radiographic films – such as used in this thesis (Kodak X-Omat V) – start to saturate above 100 cGy. However, typical doses per fraction are in the order of 200 cGy, which cause the film to get saturated. That's why usually (at least for the pre-treatment situation) films are irradiated with lower doses than planned. Thus, using films for the measurement of PDIs the real treatment delivery can't be investigated. In IMRT delivered by the sliding-window technique, the leafpairs are forced to move faster due to the reduced dose to be delivered by the linac. Alternatively, or in case of exceeding the maximum possible leaf speed, the dose rate is reduced. By any means, in case of different MU-settings, the delivery differs from the original treatment delivery.

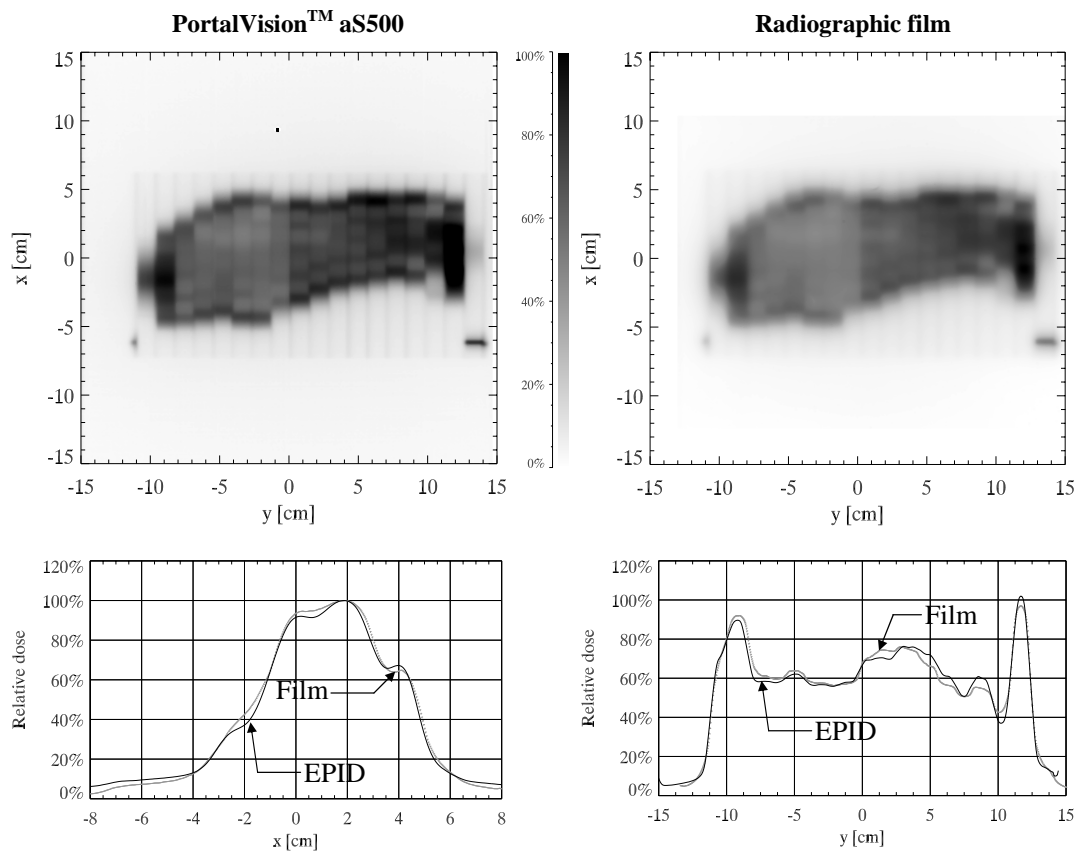


Figure 5.27 Portal dose images for the treatment situation (phantom of Figure 4.3) measured by the EPID and film for the bronchus case. A 15 MV photon field was delivered dynamically using the sliding-window technique. The comparison of the dose profiles provides an agreement in the order of 3% and 4 mm.

6

Verification of IMRT

6.1 OVERVIEW

The actual IMRT verification consists in the comparison of calculated and measured portal dose images (PDI). The calculation of PDIs has been described in Chapter 4, whereas Chapter 5 dealt with the measurement of PDIs using the EPID. However, the comparison between two two-dimensional data sets (such as PDIs) is not straightforward. Of course, one can build the difference between each pixel's dose value, but steep dose gradients will then surely lead to high differences. Therefore, at regions where high dose gradients are prominent, the difference in dose is not a suitable measure for the agreement (or disagreement) between two PDIs. That is why the difference in space is more interesting at regions with high dose gradients. In the following, a procedure is presented which allows to simultaneously quantify the differences in dose and those in space. This so-called gamma-evaluation method has recently been introduced by Low *et al.* (1998) for the comparison of one- and two-dimensional data sets. Finally, the gamma-evaluation method is applied for the dosimetric verification of intensity modulated fields.

6.2 GAMMA-EVALUATION METHOD

As has already been demonstrated in Chapter 4 and 5, the comparison between line profiles is a simple quantitative evaluation for the agreement of two dose distributions. However, PDIs contain two-dimensional information and therefore a two-dimensional quantitative analysis is required for dosimetric IMRT verification.

A quantitative comparison between two two-dimensional data sets needs to be subdivided into regions of high and low dose gradients (Van Dyk *et al.* 1993). In low gradient regions, the dose difference is applied as an acceptance criterion. In high dose regions, van Dyk *et al.* proposed to use the so-called distance-to-

agreement (DTA) quantity, which is defined as the spatial distance between a data point in the first data set and the nearest point in the second data set that reveals the same dose.

Low *et al.* (1998) presented a method (in the following called gamma-evaluation method), which simultaneously quantifies the differences in dose and spatial distance. Suppose a calculated PDI $D_{calc}(\vec{r}_{calc})$ which has to be compared with a measured PDI $D_{meas}(\vec{r}_{meas})$. The basic principle of the gamma-evaluation method is illustrated in Figure 6.1 and is based on two acceptance criteria: ΔD_{tol} denotes the tolerance for the dose difference (e.g. 3% of maximal dose) and Δd_{tol} denotes the tolerance for the DTA (e.g. 2 mm). For a specific point $(D_{meas}, \vec{r}_{meas})$ of the measured PDI, an ellipsoid can be defined by

$$1 = \sqrt{\frac{\Delta r^2}{\Delta d_{tol}^2} + \frac{\Delta D^2}{\Delta D_{tol}^2}}$$

with the distance

$$\Delta r = |\vec{r}_{meas} - \vec{r}_{calc}|$$

between the measured and the calculated data point at \vec{r}_{calc} and the dose difference

$$\Delta D = D_{calc}(\vec{r}_{calc}) - D_{meas}(\vec{r}_{meas}).$$

For the measured data point $(D_{meas}, \vec{r}_{meas})$, this ellipsoid describes the room of acceptance based on the presumed tolerances ΔD_{tol} and Δd_{tol} . The pass-fail criterion developed by Harms *et al.* (1994) is based on this ellipsoid: If at least one point $(D_{calc}, \vec{r}_{calc})$ is lying within this ellipsoid, the measured data point passes the criterion and is said to be matched to the calculated data point. Otherwise, however, this method lacks of really quantifying the degree of disagreement since of its binary nature. That is why Low *et al.* (1998) introduced the gamma value. For this purpose, a set of ellipsoids are calculated for the measured data point $(D_{meas}, \vec{r}_{meas})$ by calculating

$$\Gamma_{\vec{r}_{meas}}(D_{calc}, \vec{r}_{calc}) = \sqrt{\frac{\Delta r^2}{\Delta d_{tol}^2} + \frac{\Delta D^2}{\Delta D_{tol}^2}}$$

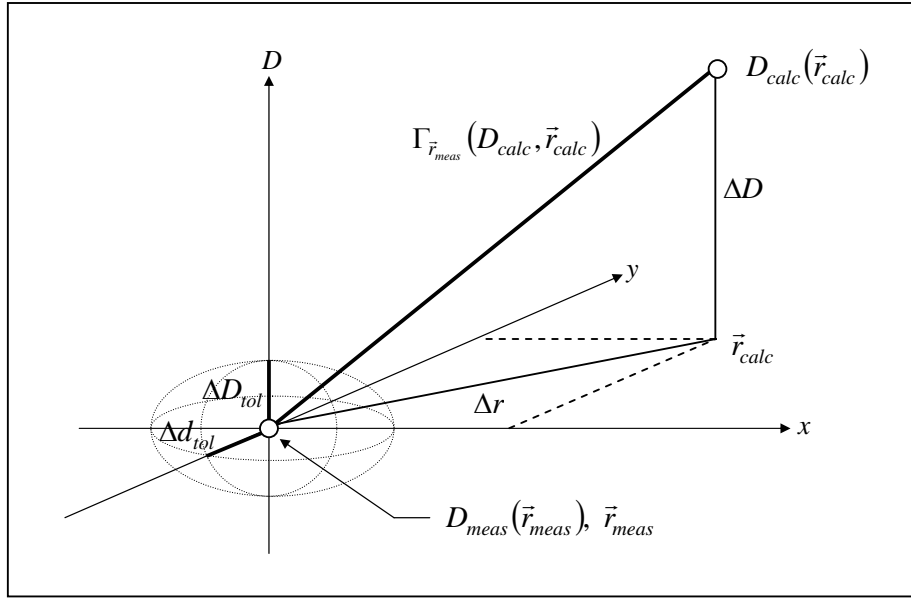


Figure 6.1 Illustration of the basic principle of the gamma-evaluation method with which the differences in dose and space are simultaneously quantified. The method relies on two acceptance criteria (ΔD_{tol} and Δd_{tol}). For a specific point $(D_{meas}, \vec{r}_{meas})$ of the measured PDI, the minimal value of all the distances $\Gamma_{\vec{r}_{meas}}(D_{calc}, \vec{r}_{calc})$ corresponds to the gamma value $\gamma_{\vec{r}_{meas}} = \min_{(D_{calc}, \vec{r}_{calc})} (\Gamma_{\vec{r}_{meas}})$.

for every point $(D_{calc}, \vec{r}_{calc})$ in the calculated PDI. Note that if $\Gamma_{\vec{r}_{meas}}(D_{calc}, \vec{r}_{calc})$ is lower or equal to one, then the acceptance criterion is fulfilled and the two dose distributions match at this point. The minimal value of $\Gamma_{\vec{r}_{meas}}$ is defined as the gamma value

$$\gamma_{\vec{r}_{meas}} = \min_{(D_{calc}, \vec{r}_{calc})} (\Gamma_{\vec{r}_{meas}})$$

and is a quantitative measure of the agreement of the two dose distributions. At regions with low dose gradients, the gamma value is a measure of the dose difference, whereas at regions with high dose gradients, the gamma value measures the spatial disorder. Suppose a dose tolerance ΔD_{tol} of 3% and a distance tolerance Δd_{tol} of 2 mm. Then a gamma value of 1.2 means a deviation of 20% from $\gamma = 1$, corresponding to a 0.6% dose-disagreement or 0.4 mm DTA greater than the tolerance limits.

The gamma-evaluation method works well for continuously defined functions. However, in practice, the validity of this method is limited due to the discretized nature of measured and calculated data sets. Consequently, the two-dimensional

data information needs to be interpolated, as has also been proposed in the literature (Depuydt *et al.* 2002).

6.3 OVERVIEW OF THE CASES STUDIED

In the following, several cases are studied for pre-treatment as well as treatment verification purposes. Some of them have already been introduced in Chapters 4 and 5. Table 6.1 provides an overview of all these cases.

Table 6.1 Overview of the cases studied in this thesis for dosimetric verification. The kind of delivery specifies whether the leaves of the MLC are moved during the delivery or not (see Section 1.4). To calculate portal dose distributions by MC simulations, the leafmotion is discretized into subfields as described in Section 4.3. Finally, different photon energies were considered.

Case name	Kind of delivery	# subfields	Energy
Pyramid	Step-and-shoot	7	15 MV
Head and neck	Sliding-window	196	6 MV
Bronchus	Sliding-window	178	15 MV
First IMRT	Sliding-window	200 (each field)	6 MV

6.4 PYRAMID

The pyramid consists of an arrangement of seven segmental subfields delivered by the step-and-shoot technique (see Chapter 1). A 15 MV photon beam with a field size of $12 \times 12 \text{ cm}^2$ is used for this pyramidal shaped intensity distribution. The MC calculation is run with 200 Mio. histories per subfield and a PDI is calculated without any patient/phantom in the beam (pre-treatment situation). The dose is scored in different depths within a water phantom ($40 \times 40 \times 10 \text{ cm}^3$) as a representation of the EPID. Finally, for each subfield a PDI is measured with the EPID. Subsequently, all these images are summed up leading to the final PDI.

Figure 6.2 shows MC calculated and measured PDIs for the pyramid as well as the resulting gamma image. For the gamma-evaluation method, a dose tolerance ΔD_{tol} of 3% and a distance tolerance Δd_{tol} of 2 mm at the portal plane ($SDD = 140 \text{ cm}$) are applied. The figure demonstrates the very good agreement between the measured and calculated portal dose images. Only 1.4% of the pixels comprise a gamma value greater than one. Although not shown here, the

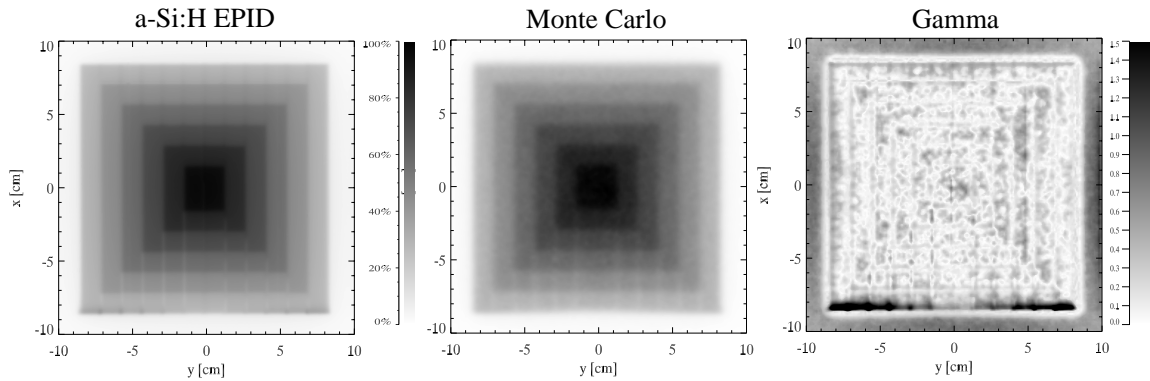


Figure 6.2 Measured and calculated PDI as well as the resulting gamma image for the pyramid in the pre-treatment configuration (without any patient/phantom in the beam). The gamma image demonstrates the very good agreement based on a dose tolerance of 3% and a distance tolerance of 2 mm in the portal plane. Only 1.4% of the pixels comprise a gamma value >1 .

corresponding comparison between a PDI measured by film dosimetry and the MC calculated PDI reveals an agreement in the same order as presented here by the use of the a-Si:H EPID.

Regarding this pyramid case, the results demonstrate the feasibility of the EPID for accurate portal dose measurements for (multiple) static fields. In addition, the MC method turns out to be very powerful for accurate dosimetric verification.

6.5 HEAD AND NECK CARCINOMA

One treatment field of an IMRT plan of a head and neck carcinoma is considered as an example of a realistic DMLC treatment delivery. The 6 MV photon field has already been investigated in Chapters 4 and 5. At this point, we focus on the gamma-evaluation for the pre-treatment verification (without any patient in the beam).

The gamma images are calculated by applying a dose tolerance ΔD_{tol} of 3% and a distance tolerance Δd_{tol} of 2 mm at the portal plane ($SDD = 140$ cm). In Figure 6.3 the gamma image is shown for the pre-treatment verification. Within the treatment field defined by the jaw positions, hardly any gamma values are greater than 1. The discrepancies outside the jaw positions are mainly determined by noise of both the a-Si:H EPID and the MC calculation. In addition, due to benchmark purposes the jaw positions in the MC calculations differ slightly from the ones used in the PDI measurements.

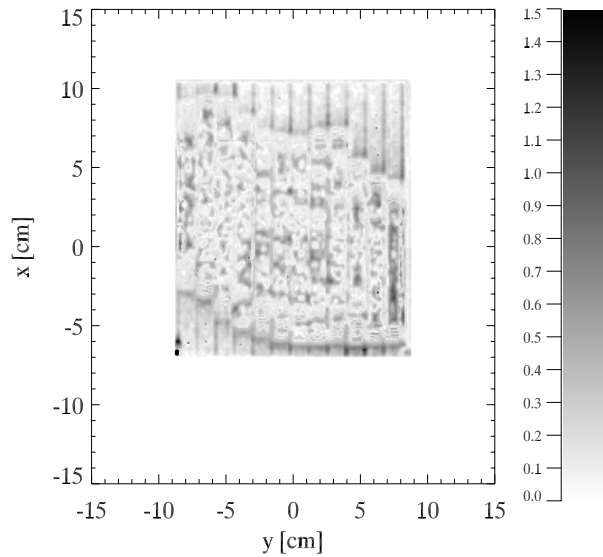


Figure 6.3 Gamma image for the pre-treatment verification of the 6 MV field of the head and neck case. In this gamma evaluation, the MC calculated PDI is compared to the measured PDI by the α -Si:H EPID. The dose limit is set to 3% of maximum dose, whereas the DTA limit is 5 mm in the portal plane ($SDD=140$ cm). Only a small number of pixels show gamma values greater than 1 reflecting the very good agreement between the portal dose distributions.

Although the gamma image reveals a very good impression of the agreement between the measured and calculated PDIs, dose profiles are a standard method to compare dose distributions. Thus, portal dose profiles along the x - and y -direction are plotted in Figure 6.4. Note that for these profiles the same normalization as the one used for the gamma-evaluation was applied.

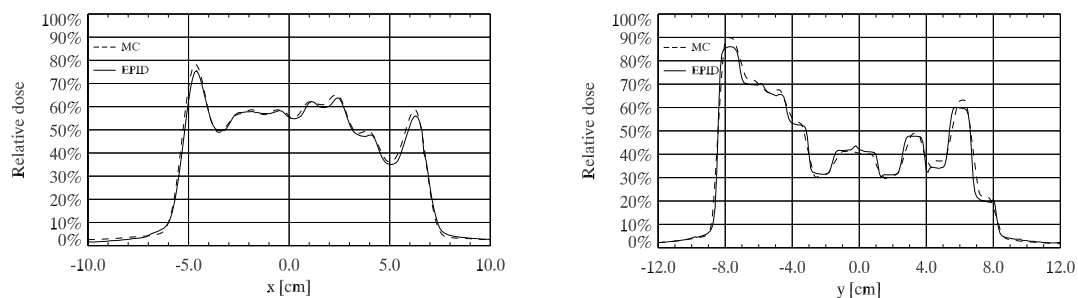


Figure 6.4 Comparison of dose profiles between MC calculations and EPID measurements along the x - and y -direction.

6.6 BRONCHUS CARCINOMA

Another example of an IMRT treatment deals with a bronchus carcinoma. In this case, an intensity modulated photon field with an energy of 15 MV is considered. As before, we focus on the gamma-evaluation for the pre-treatment verification using the same tolerances as in Section 6.5.

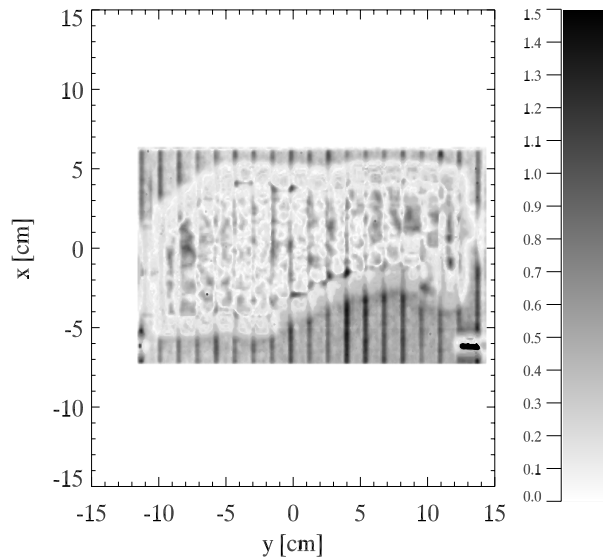


Figure 6.5 Gamma image for the treatment verification of the bronchus carcinoma using a 15 MV photon beam. The dose limit is set to 3% of maximum dose, whereas the DTA limit is 5 mm in the portal plane ($SDD=140$ cm).

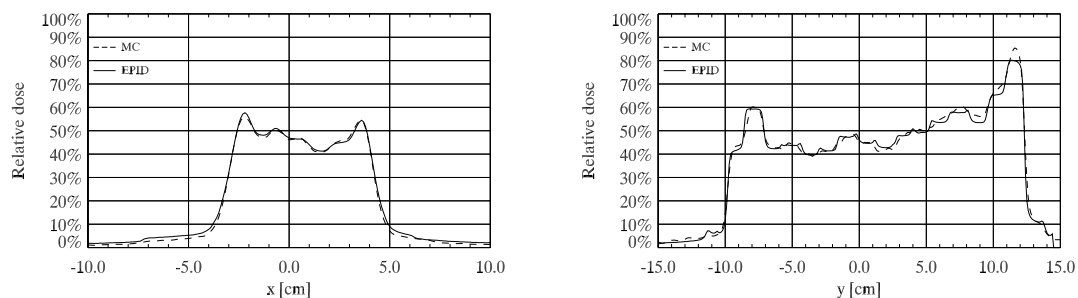


Figure 6.6 Dose profiles along the x - and y -direction for the pre-treatment verification of the bronchus carcinoma.

For the pre-treatment verification, the gamma image is given in Figure 6.5. Within the treatment field only 0.3% of the pixels possess a gamma value greater than 1. This very good agreement between the MC calculated and EPID measured PDIs is also expressed in Figure 6.6, where corresponding dose profiles are shown.

6.7 FIRST IMRT TREATMENT

At the Inselspital Berne, in January 2002, the first patient was treated with IMRT. The patient had a solitaire manifestation of the vertebral column. The treatment planning was performed by CadPlan using the inverse treatment planning algorithm Helios (Varian Medical Systems). As shown in Figure 6.7, five intensity modulated fields were provided using this optimization. More details on the fields is given in Table 6.2. The photon energy used to treat this cancer was 6 MV.

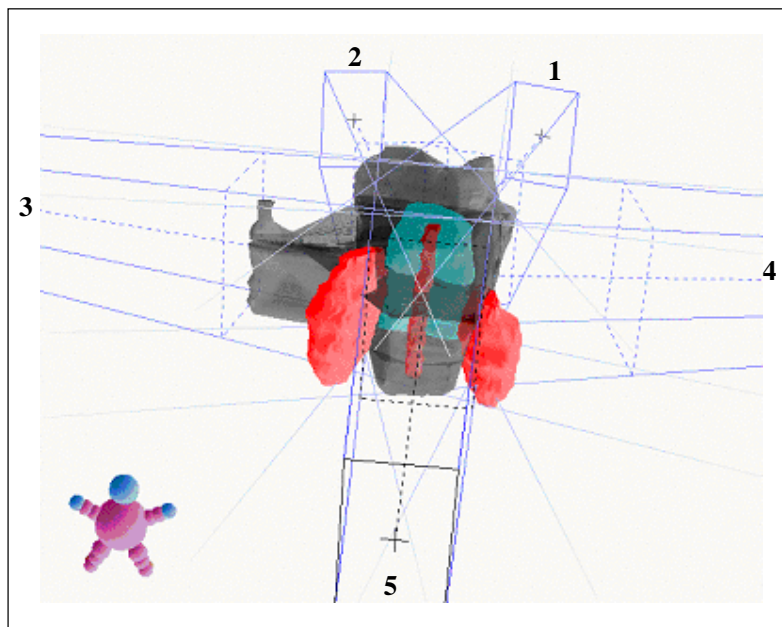


Figure 6.7 Screenshot of the CadPlan (Varian Medical Systems) treatment planning system. The first IMRT patient treated at the Inselspital Berne was a patient with a solitaire manifestation of the vertebral column. A five field plan was obtained by inverse planning using the Helios algorithm (Varian Medical systems). The numbers 1 to 5 denote the consecutive numbering of the fields.

Table 6.2 Summary of the five modulated treatment fields used for the first IMRT treatment. All fields are delivered using a 6 MV photon beam.

Field number	Gantry angle	Recommended jaws [cm×cm]
1	15°	12.4 × 9.0
2	345°	12.4 × 9.0
3	280°	12.4 × 10.6
4	80°	12.4 × 10.0
5	180°	12.4 × 9.2

The validation of the treatment planning as well as the standard quality assurance procedure for the patient treatment plan have been described by Vetterli *et al.* (2002a). Principally, each single field is verified by the measurement of two-dimensional dose distributions in a water phantom using film dosimetry. The measured dose distributions are then compared to corresponding dose distributions calculated by the treatment planning system. For this purpose, the fields were exported to the indicated water phantom. Although very good agreement in the order of 1.5% between dose profiles has been reported, the procedure lacks of being extremely laborious. Moreover, the verification is not fully independent of the original treatment planning system. And finally, the procedure covers only the pre-treatment verification.

In the following, the dosimetric verification method is based on the comparison of pre-calculated and measured PDIs. Therefore, the high efficacy of the a-Si:H EPID as well as the inherent accuracy of MC simulations are exploited. For each single field PDIs were calculated for pre-treatment and treatment verification. Note that employing MC for the pre-calculation of PDIs satisfies the demand on a verification method being fully independent of the original therapy planning system.

Figure 6.8 shows the a-Si:H measured portal dose distributions of all IMRT treatment fields for the pre-treatment situation. For all these treatment fields, the gantry was in its basic position (zero gantry angle) and the delivery of the fields was performed with the corresponding MUs from the treatment planning outcome. The EPID was positioned at an *SDD* of 140 cm and the measurement of the PDIs was performed as described in Chapter 5.

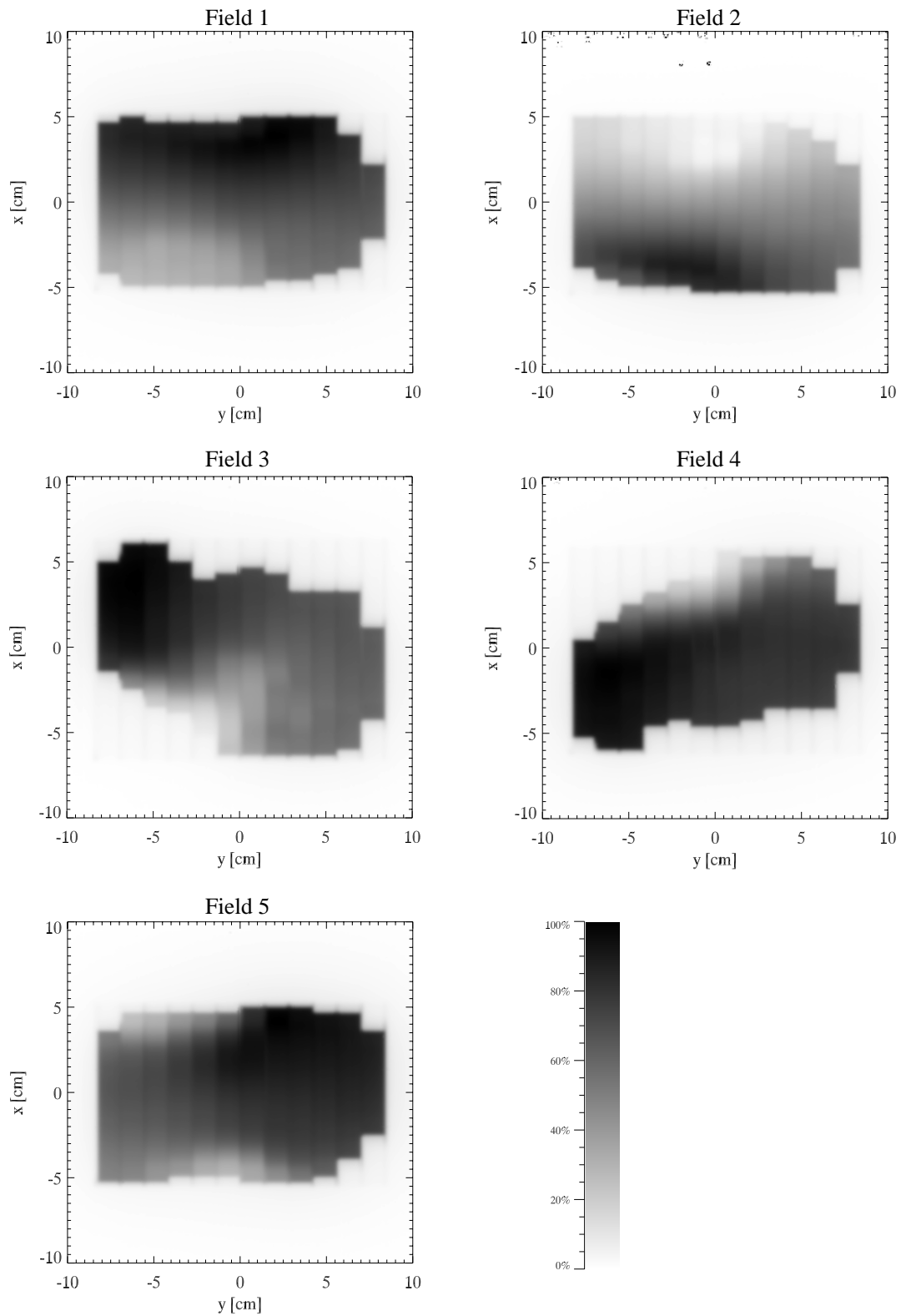


Figure 6.8 EPID measured PDIs for the pre-treatment verification of the first IMRT treated patient. The EPID was positioned at an SDD of 140 cm and the measurement of the PDIs was performed as described in Chapter 5.

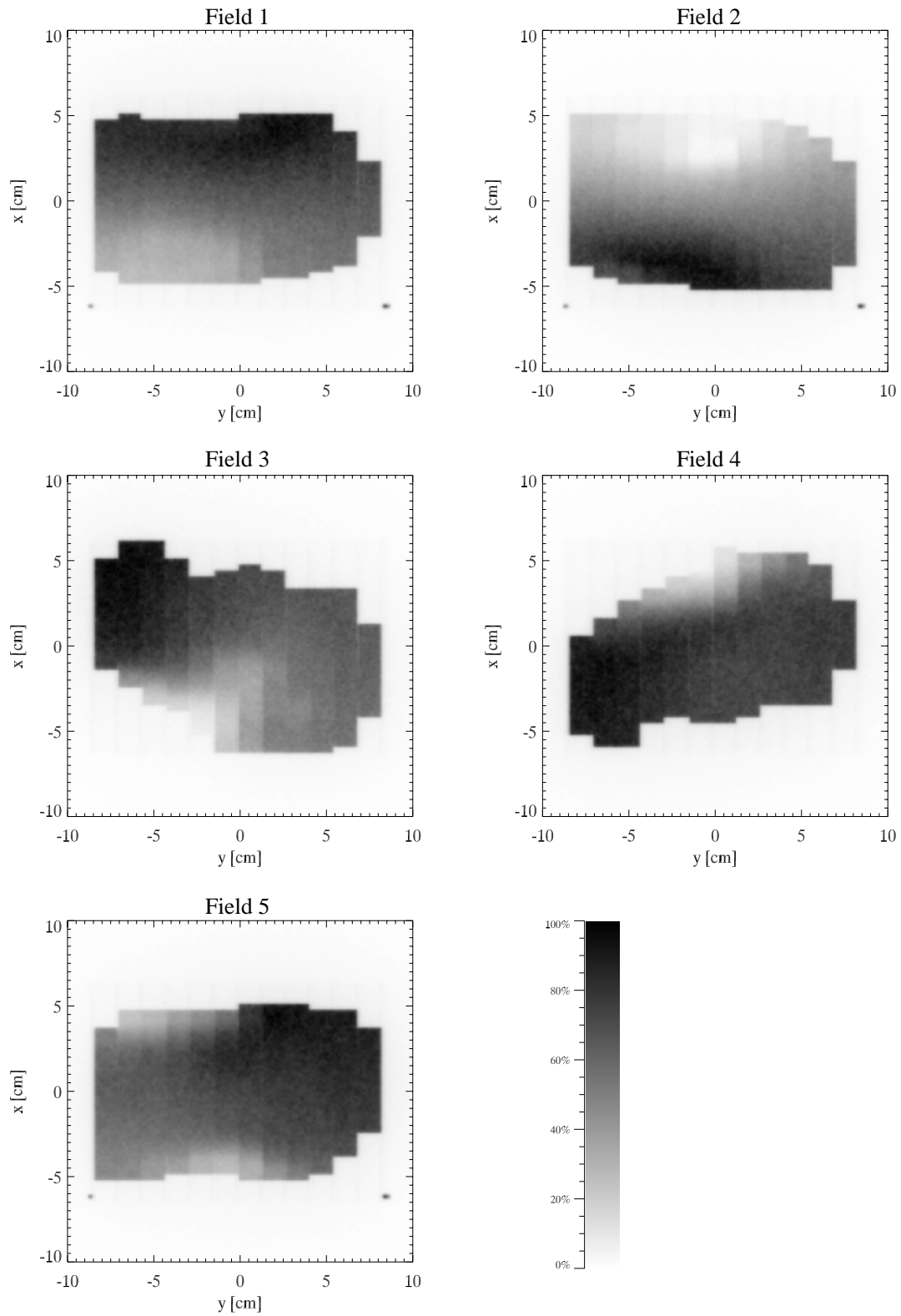


Figure 6.9 MC calculated PDIs for the pre-treatment verification of the first IMRT treated patient.

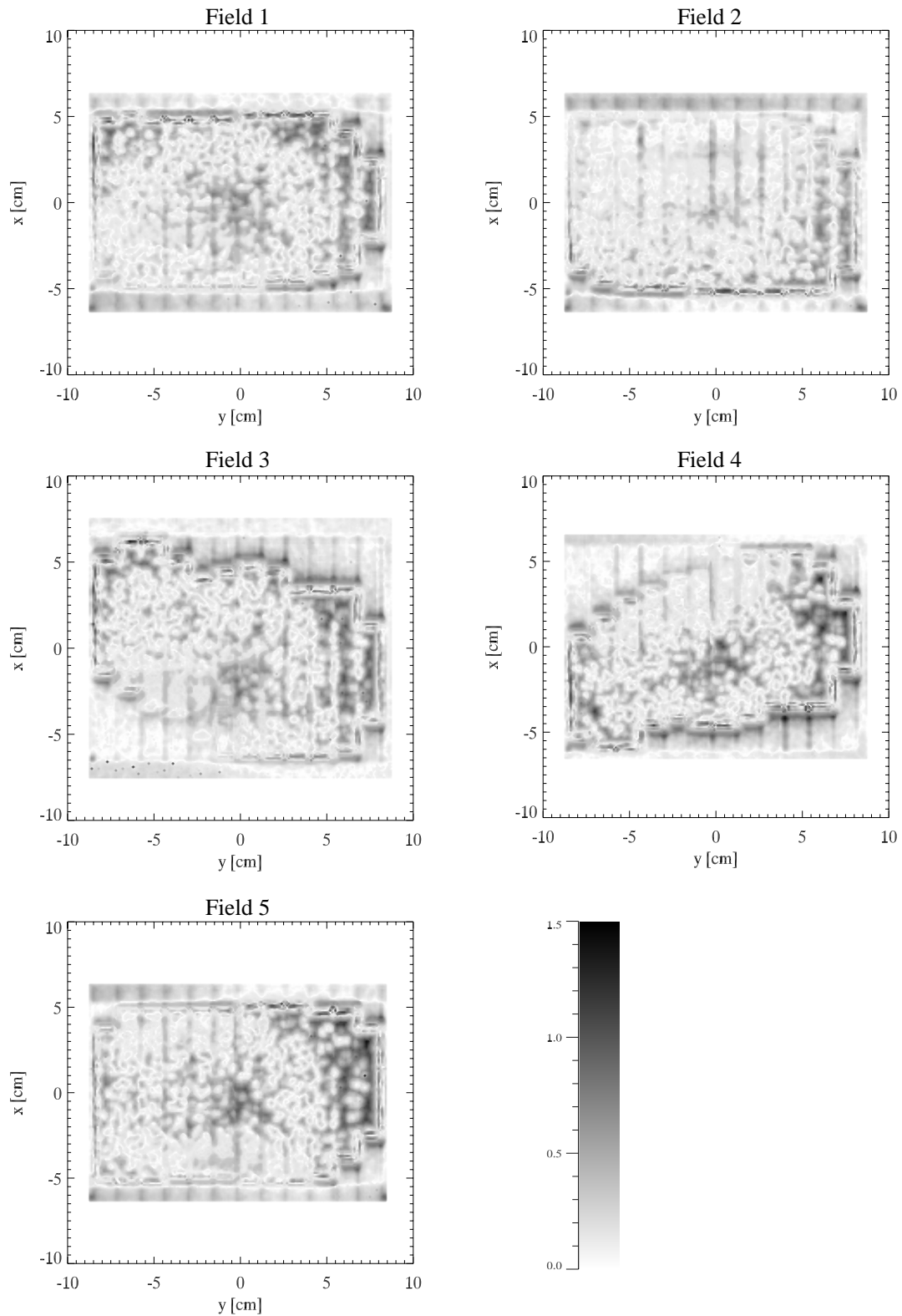


Figure 6.10 Gamma images for all treatment fields used for the first IMRT treatment. The gamma images are obtained by the comparison between EPID measured and MC calculated PDIs. The dose limit is set to 3% of maximum dose, whereas the DTA limit is 5 mm in the portal plane (SDD=140 cm).

The corresponding PDIs were calculated by MC simulations and are shown in Figure 6.9. For this purpose, each treatment field was discretized into 200 subfields and simulated as described in Chapter 4. The visual indicator of a very good agreement between the measured and calculated PDIs is further confirmed by quantitative analysis using the gamma-evaluation method. The results of this comparison are given in Figure 6.10, where gamma images are shown for all PDIs. For all investigations, a dose tolerance ΔD_{tol} of 3% and a distance tolerance Δd_{tol} of 5 mm at the portal plane are applied. The gamma images demonstrate the good agreement between the calculated and measured PDIs for the pre-treatment verification. In Figure 6.11 the dose profiles along the

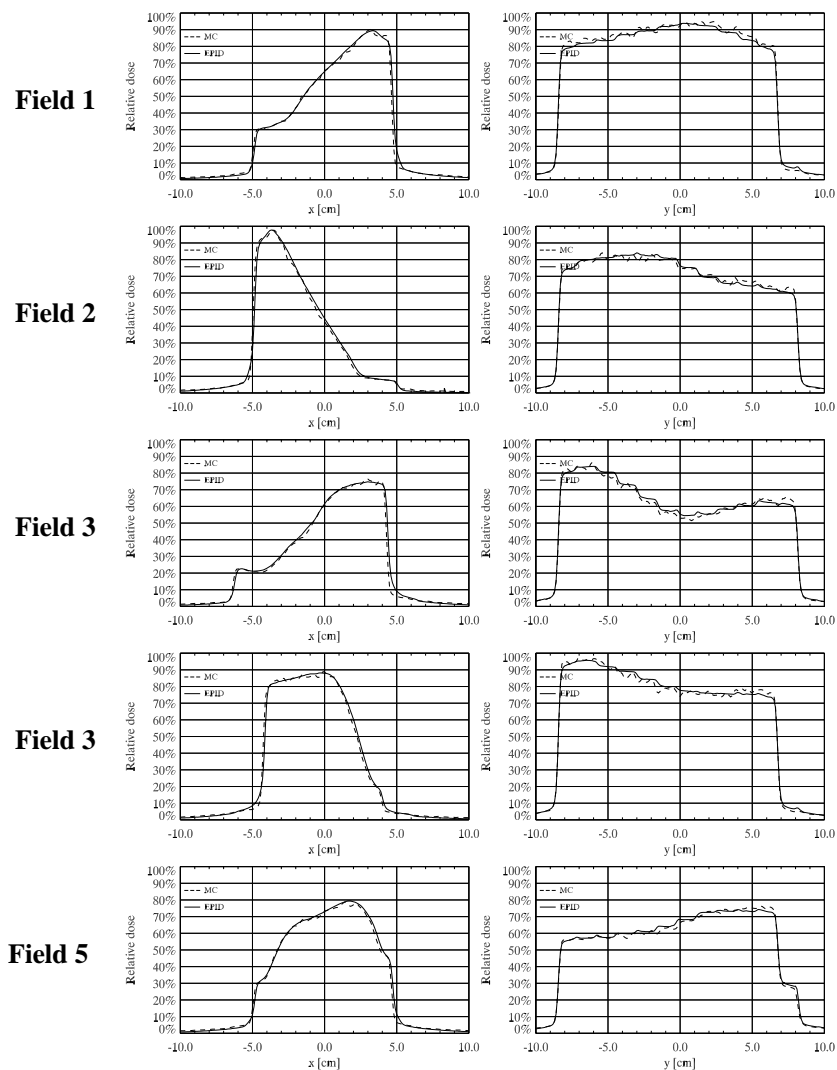


Figure 6.11 Dose profiles along the x - and y -direction for all intensity modulated treatment fields of the first IMRT treatment.

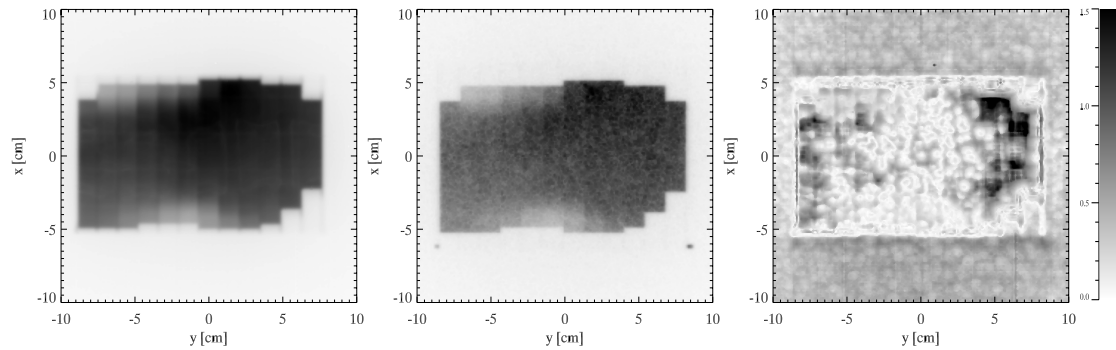


Figure 6.12 Measured (left) and calculated (center) PDIs of field 5 for the treatment situation. From the resulting gamma image (right) isoe discrepancies occur, particularly on the right hand side of the image. These high gamma values are believed to be due to problems of the treatment delivery or the patient positioning.

x - and y -direction are shown. The agreement is of the same order as has been reported by Vetterli *et al.* (2002a) for the comparison between film measurements and the treatment planning system.

As an example, for field 5 the corresponding results for the treatment verification are shown in Figure 6.12 and Figure 6.13. In this case, the agreement is lower compared to the pre-treatment verification case. Particularly on the right hand side of the PDIs deviations of up to 10% in dose (relative to the dose maximum of the image) appear. These deviations are not likely to be caused by

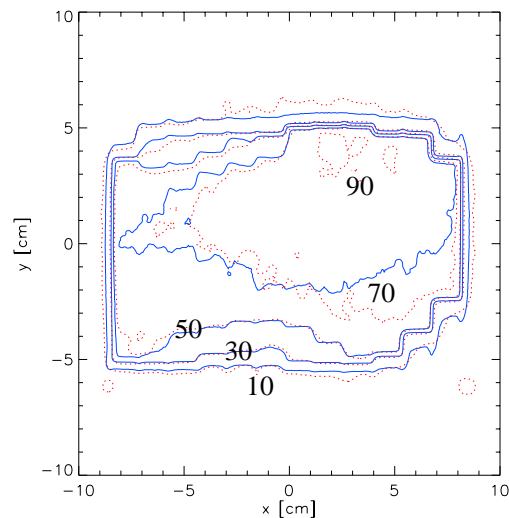


Figure 6.13 Isodose distributions of the measured (full) and calculated (dotted) PDIs for the treatment situation of field 5.

measurement errors or calculation errors. Firstly, the accuracy of the measurement of a PDI is backed from different previous studies (Manser *et al.* 2001). Secondly, the MC calculation is correct due to the fact that MC calculated dose distributions within the patient agree well with the corresponding dose distribution obtained with the treatment planning system (CadPlan). And thirdly, the portal dose image calculated with the CadPlan's exitdose algorithm shows the same results (Manser *et al.* 2003a,b).

In conclusion, the results shown here demonstrate the feasibility of a dosimetric treatment verification of IMRT using an EPID and MC calculations. On a field-by-field basis calculated and measured PDIs are compared using the gamma-evaluation method. The relative agreement between the PDIs is in the order of 3-4% and 3-4 mm in the isocenter plane which is comparable to film dosimetry (Hale *et al.* 1994). However, mainly due to its convenience to use, the EPID based IMRT verification is now getting a 'standard' in clinical routine.

7

Discussion

7.1 IMRT IMPLEMENTATION AND VERIFICATION

The main advantage of using intensity modulated treatment fields is the ability to irradiate the target more conformally than by conventional radiotherapy treatment techniques. As such, IMRT is part of the more general conformal radiotherapy. IMRT provides the possibility of dose escalation resulting in an increase in local tumor control (Zelefsky *et al.* 2002).

In recent years, much effort has been spent to optimize IMRT treatment planning and IMRT delivery. There has been a dramatic increase of the number of IMRT patient treatments all over the world. Alongside this development, there has been a progression in the requirement of efficient verification procedures. The verification process has become the main impediment of the implementation of IMRT into clinical practice (Carol 1997, Webb 1997). Currently, pre-treatment verification is carried out mainly by the use of radiographic films. However, both the accuracy and the efficiency of film dosimetry are not suitable for routine quality assurance purposes.

As presented in this work, the PortalVision™ aS500 is a versatile EPID and has proven to be suitable for measuring portal dose images of dynamically applied fields (Manser *et al.* 2001, Manser *et al.* 2003a-b). From the results, it can be concluded that the cumbersome film is replaceable by the a-Si:H EPID. Bearing in mind the advantages (see next Section) of using an EPID for dosimetric verification, this thesis supports the implementation of IMRT in the clinical routine.

7.2 DOSIMETRIC IMRT VERIFICATION USING AN A-SI:H EPID

The presented work focuses on the dosimetric verification of dynamically applied IMRT deliveries by using an a-Si:H based electronic portal imaging device. As has been shown in this thesis, the use of an a-Si:H EPID supersedes standard

verification techniques such as film dosimetry or point measuring devices (TLD, diode, ionization chamber) in different ways: First, EPIDs are fast compared to the time-consuming film handling (positioning, developing, digitization process, calibration for every batch); second, the a-Si:H EPID shows a highly linear dose response relationship in an appropriate dosimetric range (Manser *et al.* 2000), the use of an a-Si:H EPID for pre-treatment verification purposes therefore does not require to modify the beam-on-time by adjusting the total dose delivered; third, EPIDs generally can be positioned accurately resulting in a reduction of misleading interpretations compared to point measuring devices; fourth, due to the excessive stable signal (long- and short-term) of the EPID there is no need to calibrate the EPID's pixel signal each time it is used; fifth, as incorporating a flat panel array, the EPID measures the portal dose distribution in two dimensions which makes the verification process very efficient compared to point measuring devices. In addition, the a-Si:H based EPID exceeds the scanning liquid ionization chamber EPID and the video-based EPID due to improved imaging performance, as is expressed by the $DQE(f)$. For the verification of dynamically applied fields, the a-Si:H based EPID surpasses the SLIC EPID due to improved temporal behavior. As has been shown in this thesis, based on an improved acquisition mode, the PortalVisionTM aS500 is capable of detecting the entire portal dose during a DMLC delivery.

7.3 SIGNAL FORMATION STUDY USING MONTE CARLO SIMULATIONS

With the intention to investigate the signal forming processes as well as the dosimetric calibration of the EPID, MC simulations were performed. The QAD analysis has shown that the signal formation can be characterized by dividing it into eight stages. Using the MC code GEANT, the energy deposition within the phosphor layer has been studied for several situations. With this, the influence of different detector components to the energy deposition in the phosphor layer has been investigated. Depending on the energy of the incident photons, either the photo-electric effect, or Compton scattering, or pair production is responsible primarily for the energy deposition. For the PortalVisionTM aS500 – composed of a 1 mm Copper plate and 0.5 mm thick Gd₂O₂S:Tb – the MC study demonstrated that for clinical photons (polyenergetic) the energy deposition is governed by the Compton scattering and by electrons released from the copper plate. With the intention of investigating the lateral spread of the signal, a model of the transport of the optical photons has been developed. From the results of this investigation it can be concluded, that the absorption of optical photons within the phosphor

layer is important – demonstrated by the escape probability of about 40% - but not the lateral spread – represented by a corresponding MTF (Manser *et al.* 2002a).

7.4 ENERGY RESPONSE STUDY USING MONTE CARLO SIMULATIONS

The energy response of the EPID has been compared to the response of a water reference system. The results show that the EPID reveals a crucial energy response due to the detector's composition of high-Z materials (mainly Gd₂O₂S:Tb) leading to an overestimation of low-energy particles. As a consequence, energy spectra changes caused by DMLC deliveries have an impact on the EPID dosimetry (Manser *et al.* 2002c). However, by taking an appropriate water depth for the calibration, these impacts are diminutive. Note that film dosimetry reveals also overestimation to low-energy photons (Hale *et al.* 1994) and therefore the same impacts are to be expected for film dosimetry.

7.5 MONTE CARLO SIMULATIONS FOR PORTAL DOSE CALCULATIONS

Alongside the investigation on the signal formation steps, MC simulations were performed for portal dose prediction purposes. For beam modeling, a multiple source model of 6 and 15 MV photon beams of a Varian Clinac 2300 C/D was developed (Fix *et al.* 2001a). The supplemented MLC (40 leaf pairs) permits the simulation of the radiation transport for dynamically applied fields. Portal dose images were calculated for the pre-treatment as well as for the treatment verification. Based on this PDI calculation method, an accuracy of 2-3% is obtained for relative dose distributions (Manser *et al.* 2003a). Even though not addressed in this thesis, the absolute dose prescription by MC calculations is principally feasible by the calibration of the number of histories to dose (Figini *et al.* 2003, Born *et al.* 2003a).

The use of MC simulations for the calculation of PDIs satisfies the requirement of a verification procedure, which is fully independent of the treatment planning system. As a consequence, the presented verification procedure detects not only errors due to incorrect dose delivery but is also a benchmark test for the treatment planning system. However, the MC method suffers from the need for long computing times to generate a PDI with acceptable statistical uncertainty. For pre-treatment verification, typical CPU times of a 6 MV IMRT field are in the order of 7 minutes per subfield on an Alpha XP 1000

workstation for 1 million primary particles per subfield. Due to a decreased statistical uncertainty, the number of histories is reduced by a factor of 1.5 for 15 MV photons beams. On the other hand, the CPU time increases by about a factor of 1.5 due to more interaction processes resulting in the same order of CPU times. Several measures can help to reduce these long computing times. Most efficient are variance reduction methods. Furthermore, several simplifications of the multiple source model would provide additional time savings.

The Swiss Monte Carlo Plan (SMCP) is a collaborative work between several institutes in Switzerland and aims to make MC based photon treatment planning available. (Born *et al.* 2003a,b). For this purpose, optimizations are made concerning beam modeling, beam modifiers and dose calculation engine. Although preliminary, the results suggest that clinical MC treatment planning for photon beams is realizable in the near future. In addition, work is in progress to implement SMCP in a commercial treatment planning system.

The impact of the project SMCP on the dosimetric verification of IMRT is obvious: With SMCP highly accurate absolute dose distributions can be calculated in the patient as well as in the portal imager. As a consequence the verification of IMRT using the a-Si:H EPID is not only restricted to relative dosimetry.

In recent years, several algorithms were developed to enable portal dose prediction. One algorithm has been presented by Pasma *et al.* (1999, 2002). In the meantime, this algorithm is implemented in Varian's treatment planning systems (CadPlan and Eclipse). Basically, this algorithm could also be used for the verification method described in this thesis. However, based on its inherent accuracy (mainly given by statistics) and due to its independence of the treatment planning system, the MC method is seen to be more powerful for IMRT verification purposes.

7.6 THE GAMMA-EVALUATION METHOD

In order to compare the predicted PDI with the measured PDI, the gamma-evaluation method by Low *et al.* (1998) has been applied. With this metric, the dose and spatial distances are quantified simultaneously for each pixel of the PDI leading to a two-dimensional gamma image. However, the interpretation of the gamma image is still a challenge. The gamma image is strongly influenced by the initial settings of the dose difference and difference-to-agreement tolerances. Hence, for interpretation purposes (such as the search of possible errors found by

the verification process), the gamma images have always to be interpreted with respect to the initial tolerances. Furthermore, a PDI is neither calculated nor measured in a plane at isocenter distance but in a portal plane located further away from the radiation source. Hence, either DTA-limits need to be given in this specific portal plane or the spatial distances in the PDI have to be transformed correspondingly to a plane located at the isocenter. As has been shown in Chapter 6, data interpolation is required for accurate gamma image calculation, which makes this method inefficient. As a consequence, the use of the gamma-evaluation method for quantitative evaluation of two PDIs is currently rarely used in clinical routine. Nowadays, most comparison techniques are relying on much simpler techniques such as superimposing isodose distributions or building solely the dose difference.

7.7 VERIFICATION OF IMRT IN CLINICAL ROUTINE

Efforts have been made to transfer the knowledge obtained from the fundamental results of this thesis to clinical routine. An example is given in Section 6.7. At the Inselspital Berne, the use of the PortalVision™ aS500 has become a ‘standard’ for pre-treatment as well as treatment verification for several reasons: The basic advantages of using an EPID instead of any other dosimetric device are obvious and have already been stated above. Alongside the implementation of IMRT in clinical routine, it was experienced that the use of an EPID for portal dosimetry is much more convenient than using film dosimetry. Not only that the films are very time consuming but it was also seen (as by many other groups) that highly accurate film dosimetry is very difficult to achieve and sometimes even not reproducible. In contrast to film, using the EPID to take portal images for patient setup purposes has proven that the high quality of the images keep on after years of operation. In addition, as described by Vetterli *et al.* (2002b), the EPID is capable of taking portal images with less than 1 MU. This enabled to introduce a new on-line setup protocol for all IMRT patients, where orthogonal setup fields are taken before each fraction.

In clinical routine, the calculation of PDIs is not yet carried out with MC simulations. Although the MC method is commonly seen as the most accurate way to calculate dose distributions, it is still too time consuming. However, recent developments – like the SMCP – aim to provide MC based treatment planning for photon beams in clinical routine. And with this, PDIs are to be calculated using the MC method with acceptable extent.

7.8 FUTURE DETECTOR DESIGN FOR HIGH-PRECISION DOSIMETRY

The aim of this study was to investigate the potential of the *original* PortalVision™ aS500 for its application in dosimetric verification of IMRT. As has been pointed out in Chapter 5, the energy response of the a-Si:H EPID differs from the response of a water reference system. The main reason for that is the overresponse to low-energy particles caused by materials with high-Z. In this thesis, numerous investigations were performed to overcome this problem by placing some buildup (polystyrene) plates on top of the EPID. The results show that the use of such PS plates changes the energy response severely at energies above 5 MeV (cf. Figure 5.10), whereas the response for low-energies is hardly affected. It has to be noted, however, that the PS plates had been placed on top of the EPID's cover which is not ideal. In the future, further work has to be done to investigate possible improvements of the EPID.

7.9 FUTURE: ESTIMATION OF DOSE DELIVERED TO THE PATIENT

In this thesis, the two-dimensional portal dose distribution (the portal dose image) is used as a measure of the quality of the treatment. However, as indicated previously, the ultimate aim of *in vivo* dosimetry is the estimation of the dose delivered to the patient. In the literature, several methods have been suggested to perform three-dimensional dose reconstruction from a measured portal dose image for static fields (McNutt *et al.* 1996, 1997, Hansen *et al.* 1996). Just recently, Partridge *et al.* (2002) demonstrated a proof-of-principle study of performing three-dimensional *in vivo* dosimetry for IMRT treatments.

Principally, the primary photon fluence at the portal plane is extracted from the EPID's portal dose image. This is accomplished by subtracting the contribution of patient scatter to the portal image from the PDI. Afterwards, the primary fluence is backprojected through the patient. At this step, the need for a current representation of the patient's anatomy is obvious and is best fulfilled by the acquisition of a CT data set at the treatment time (REF). Finally, the primary fluence above the patient is used to calculate the dose distribution in the patient.

Thus, in future, the portal dose imaging with an EPID will have to be to enable three-dimensional dose reconstructions. This includes the development of quantitative comparison procedures. They can be realized with the gamma-evaluation method presented in this work.

References

AAPM 2001 Basic applications of multileaf collimators: report of the AAPM radiation therapy committee Task Group No 50 *AAPM Report No 72*, Madison, WI: American Institute of Physics by Medical Physics Publishing

Ahnesjö A, Saxner M, and Trepp A A 1992 Pencil beam model for photon dose calculation *Med. Phys.* **19** 263-273

Amaldi U 1999 Cancer therapy with particle accelerators *Nuclear Physics A*654 375c-399c

Andreo P 1991 Monte Carlo techniques in medical radiation physics *Phys. Med. Biol.* **36** 861-920

Antonuk L E, Boudry J, Huang W, McShan D L, Morton E J, Yorkston J, Longo M J, and Street R A 1992 Demonstration of megavoltage and diagnostic x-ray imaging with hydrogenated amorphous silicon arrays *Med. Phys.* **19** 1455-1466

Antonuk L E, El-Morhi Y, Siewerdsen J H, Yorkston J, Huang W, and Scarpine V E 1997 Empirical investigation of the signal performance of a high-resolution, indirect detection, active matrix flat-panel iamger (AMFPI) for fluoroscopic and radioagraphic operation *Med. Phys.* **24** 51-70

Antonuk L E, El-Mohri Y, and Jee K-W 1998 *Imaging in Radiation Therapy* (Madison, WI: Medical Physics Publishing, Editors: Hazle J D and Boyle A L)

Antonuk L E 2002, Electronic portal imaging devices: a review and historical perspective of contemporary technologies and research *Phys. Med. Biol.* **47** R31-R65

Arnfield M, Siebers J, Kim J, Wu Q, Keall P, and Mohan R 2000 A method for determining multileaf collimator transmission and scatter for dynamic intensity modulated radiotherapy *Med. Phys.* **27** 2231-2241

Barish R J, Fleischman R C, and Pipman Y M 1987 Teletherapy beam characteristics: the first second *Med. Phys.* **14** 657-661

Bissonette J P, Cunningham I A, Jaffray D A, Fenster A, and Munro P 1997 A quantum accounting and detective efficiency analysis for video-based portal imaging *Med. Phys.* **24** 815-826

Boellaard R, van Herk M, and Mijnheer B J 1996 The dose-response relationship of a liquid-filled electronic portal imaging device *Med. Phys.* **23** 1601-1611

- Boellaard R, van Herk M, Uiterwaal H, and Mijnheer B J 1998 First clinical tests using a liquid-filled electronic portal imaging device and a convolution model for the verification of the midplane dose *Radiother. Oncol.* **47** 303-312
- Born E J, Fix M K, Gamper U, Manser P, Figini S P, Cris C, Frei D, Pfeiffer R, Neuenschwander H, Volken W, Niederer P, and Mini R 2003a Towards clinical Monte Carlo treatment planning for photon beams: first results *Joint meeting of SASRO and SGSMP 2003* Geneva, Switzerland
- Born E J, Fix M K, Figini S P, Manser P, Frei D, Volken W, Neuenschwander H, Niederer P, and Mini R 2003b Towards clinical Monte Carlo treatment planning for photon beams: first results from Swiss Monte Carlo Plan *World Congress on Medical Physics and Biomedical Engineering 2003* Sidney, Australia
- Bortfeld T R, Kahler D L, Waldron T J, and Boyer A L 1994 X-ray field compensation with multileaf collimators *Int. J. Radiat. Oncol. Biol. Phys.* **28** 723-730
- Boyer A L 1982 Compensating filters for high energy x rays *Med. Phys.* **9** 429-433
- Boyer A L and Mok E 1985 A photon dose distribution model employing convolution calculations *Med. Phys.* **12** 169-177
- Boyer A L, Antonuk L, Fenster A, Meertens H, Munro P, Reinstein L E and Wong J 1992 A review of electronic portal imaging devices (EPIDs) *Med. Phys.* **19** 1-16
- Burman C, Chui C S, Kutcher G, Leibel S, Zelefsky M, LoSasso T, Spirou S, Wu Q, Yang J, Stein J, Mohan R, Fuks Z, and Ling C C 1997 Planning, delivery, and quality assurance of intensity-modulated radiotherapy using dynamic multileaf collimator: A strategy for large-scale implementation for the treatment of carcinoma of the prostate *Int. J. Rad. Oncol. Biol. Phys.* **39** 863-873
- Carol M P 1997 IMRT: Where we are today *The Theory & Practice of Intensity Modulated Radiation Therapy* (ed. by E S Sternick, Madison: Advanced Medical Publishing)
- CERN Application Software Group Computing and Network Division 1995a GEANT-detector description and simulation tool *CERN Program Library Long Writeup W5013* Geneva, Switzerland
- CERN 1995 Application Software Group Computing and Network Division *GEANT – detector description and simulation tool* (Geneva, Switzerland: CERN Program Library Long Writeup)

- CERN 1996 *Heilen mit Hadronen – Physik in der Medizin und Biologie* – ed Kienzle W and Pascolini A (CERN, Geneva, Switzerland)
- Chang J, Mageras G S, Chus C S, Ling C C, and Lutz W 2000 Relative profile and dose verification of intensity-modulated radiation therapy *Int. J. Rad. Oncol. Biol. Phys.* **47** 231-240
- Cheng C-W and Das I J 2002 Comparison of beam characteristics in intensity modulated radiation therapy (IMRT) and those under normal treatment condition *Med. Phys.* **29** 226-230
- Chui C S, Spiridon S, and LoSasso T 1996 Testing of dynamic multileaf collimation *Med. Phys.* **23** 635-641
- Chui C S, Chan M F, Yorke E, Spirou S, and Ling C C 2001 Delivery of intensity-modulated radiation therapy with a conventional multileaf collimator: comparison of dynamic and segmental methods *Med. Phys.* **28** 2441-2449
- Convery D J and Rosenbloom M E 1992 The generation of intensity-modulated fields for conformal radiotherapy by dynamic collimation *Phys. Med. Biol.* **37** 1359-1374
- Cormack A M 1987 A problem in rotation therapy with x-rays *Int. J. Rad. Oncol. Biol. Phys.* **13** 623-630
- Cunningham I A, Westmore M S, and Fenster A 1994 A spatial-frequency dependent quantum accounting diagram and detective quantum efficiency model of signal and noise propagation in cascaded imaging systems *Med. Phys.* **21** 417-427
- Cunningham I A and Shaw R 1999 Signal-to-noise optimization of medical imaging systems *J. Opt. Soc. Am. A* **16** 621-632
- Curtin-Savard A J, and Podgorsak E B 1999 Verification of segmented beam delivery using a commercial electronic portal imaging device *Med. Phys.* **26** 737-742
- Depuydt T, Van Esch A, and Huyskens D 2002 A quantitative evaluation of IMRT dose distributions: refinement and clinical assessment of the gamma evaluation *Radiother. Oncol.* **62** 309-319
- Eilertsen K Automatic detection of single MLC leaf positions with correction for penumbral effects and portal imaged dose rate characteristics *Phys. Med. Biol.* **42** 313-334

- Eisbruch A 2002, Intensity-modulated radiotherapy of head-and-neck cancer: encouraging early results *Int. J. Rad. Oncol. Biol. Phys.* **53** 1-3
- El-Mohri Y, Antonuk L E, Yorkston J, Jee K-W, Maolinbay M, Lam K L, and Siewerdsen J H 1999 Relative dosimetry using active matrix flat-panel imager (AMFPI) technology *Med. Phys.* **26** 1530-1541
- Essers M, Lanson J H, Leunens G, Schnabel T, and Mijnheer B J 1995, The accuracy of CT-based inhomogeneity corrections and in vivo dosimetry for the treatment of lung cancer *Radiother. Oncol.* **37** 199-208
- Essers M, Hoogervorst B R, van Herk M, Lanson H, and Mijnheer B J 1995 Dosimetric characteristics of a liquid-filled electronic portal imaging device *Int. J. Radiat. Oncol. Biol. Phys.* **33** 1265-1272
- Figini S P, Fix M K, Manser P, Born E J, Frei D, Volken W, Neuenschwander H, Niederer P, and Mini R 2003 Monte Carlo treatment planning for photon beams: Swiss Monte Carlo Plan *Med. Phys.* **30** 1516 (abstract)
- Fix M K, Stampanoni M, Manser P, Born E J, Mini R, and Rügsegger P 2001a A multiple source model for 6 MV photon beam dose calculations using Monte Carlo *Phys. Med. Biol.* **46** 1407-1427
- Fix M K, Manser P, Born E J, Mini R, and Rügsegger P 2001b Monte Carlo simulation of a dynamic MLC based on a multiple source model *Phys. Med. Biol.* **46** 3241-3257
- Fix M K, Manser P, Born E J, Vetterli D, Mini R, and Rügsegger P 2001c Monte Carlo simulation of a dynamic MLC: Implementation and applications *Z. Med. Phys.* **11** 163-170
- Galvin J M, Smith A R, and Lally B 1993 Characterization of a multi-leaf collimator system *Int. J. Radiat. Oncol. Biol. Phys.* **25** 181-192
- Hale J I, Kerr A T, and Shragge P C 1994 Calibration of film for accurate megavoltage photon dosimetry *Medical Dosimetry* **19** 43-46
- Hansen V N, Evans P M, and Swindell W 1996 The application of transit dosimetry to precision radiotherapy *Med. Phys.* **23** 713-721
- Hansen V N, Evans P M, Budgell G J, Mott J H, Williams P C, Brugman M J, Wittkamper F W, Mijnheer B J, and Brown K 1998 Quality assurance of the dose delivered by small radiation segments *Phys. Med. Biol.* **43** 2665-2675
- Huq M S, Das I J, Steinberg T, and Galvin J M 2002 A dosimetric comparison of various multileaf collimators *Phys. Med. Biol.* **47** N159-N170

- IMRT CWG 2001 Intensity-modulated radiotherapy: current status and issues of interest *Int. J. Rad. Oncol. Biol. Phys.* **51** 880-914
- Jaffray D A, Battista J J, Fenster A, and Munro P 1995 Monte Carlo studies of x-ray energy absorption quantum noise in megavoltage transmission radiography *Med. Phys.* **22** 1077-1088
- James H V, Atherton S, Budgell G J, Kirby M C, and Williams P C 2000 Verification of dynamic multileaf collimation using an electronic portal imaging device *Phys. Med. Biol.* **45** 495-509
- Jerai R, Keall P J, and Siebers J V 2002 The effect of dose calculation accuracy on inverse treatment planning *Phys. Med. Biol.* **47** 391-407
- Johns H E and Cunningham J R 1983 *The Physics of Radiology (4th Edition)* (Charles C Thomas, Springfield, Illinois, USA)
- Kausch C, Schreiber B, Kreuder F, Schmidt R, and Dössel D 1999 Monte Carlo simulations of the imaging performance of metal plate/phosphor screens used in radiotherapy *Med. Phys.* **26** 2113-2124
- Keller H, Fix M K, Liistro L, and Rügsegger P 2000 Theoretical considerations to the verification of dynamic multileaf collimated fields with a SLIC-type portal image detector *Phys. Med. Biol.* **45** 2531-2545
- Kirby M C and Williams P C 1993 Measurement possibilities using an electronic portal imaging device *Radiother. Oncol.* **29** 237-243
- Kirby M C and Williams P C 1995 The use of an electronic portal imaging device for exit dosimetry and quality control measurements *Int. J. Radiat. Oncol. Biol. Phys.* **31** 593-603
- Kohlbrener A 2000 Stacked fan-beam scanning for fast high-resolution computed tomography *Thesis ETH Zurich*
- Korevaar E W and Davis J B 2002 Implementation of IMRT treatment: verification of dosimetric and geometric accuracy *6th Annual SASRO Meeting*, Zurich, Switzerland
- Kroonwijk M, Pasma K L, Quint S, Koper P C M, Visser A G, and Heijmen B J M 1998 In vivo dosimetry for prostate cancer patients using an electronic portal imaging device (EPID); demonstration of internal organ motion *Radiother. Oncol.* **49** 125-132
- Langmack K A 2001 Portal imaging *British Journal of Radiology* **74** 789-804

- Lee N, Xia P, Quivey J, Sultanem K, Poon I, Akazawa C, Akazawa P, Weinberg V, and Fu K 2002 Intensity-modulated radiotherapy in the treatment of nasopharyngeal carcinoma: an update of the UCSF experience *Int. J. Rad. Oncol. Biol. Phys.* **53** 12-22
- Leo W R (ed) 1994 *Techniques for Nuclear and Particle Physics Experiments (Second Revised Edition)* (New York: Springer)
- Levi F, Raymond L, Schüler G, Fisch T, Bouchardy Ch, Alleman J, Joris T, and Torhorst J 1998 *Krebs in der Schweiz, Fakten, Kommentare* ed Schweizerische Krebsliga (Berne, Switzerland)
- Ling C C, Burman C, Chui C S, Kutcher j, Leibel S A, LoSasso T, Mohan R, Bortfeld T, Reinstein L, Spirou S, Wang X H, Wu Q, Zelefsky m, and Fuks Z 1996 Conformal radiation treatment of prostate cancer using inversely-planned intensity-modulated photon beams produced with dynamic multileaf collimation *Int. J. Radiat. Oncol. Biol. Phys.* **35** 721-730
- LoSasso T, Chui C S, and Ling C 1998 Physical and dosimetric aspects of a multileaf collimation system used in the dynamic mode for implementing intensity modulated radiotherapy *Med. Phys.* **25** 1919-1927
- Low D A, Harms W B, Mutic S, and Purdy J A 1998 A technique for the quantitative evaluation of dose distributions *Med. Phys.* **25** 656-661
- Mackie T R, Scrimger J W, and Battista J J 1985 A convolution method for calculating dose for 15-MV x rays *Med. Phys.* **12** 188-196
- Madan A and Shaw P 1988 *The physics and applications of amorphous semiconductors* (London: Academic Press, Inc. (London) Ltd.)
- Mageras G S, Mohan R, Burman C, Barest D, and Kutches G J 1991 Compensators for three-dimensional treatment planning *Med. Phys.* **18** 133-140
- Maidment A D A and Yaffe M J 1995 Analysis of signal propagation in optically coupled detectors for digital mammography: I. Phosphor screens *Phys. Med. Biol.* **40** 877-889
- Manser P, Fix M K, Vetterli D, Born E J, Mini R, and Rügsegger P 2000 Dose response of the PortalVisionTM aS500 *SGSMP annual meeting report* (Ed. Roth J, Nemeč H W, Roser H W, Schnekenburger B, Basel, Switzerland) 109-114
- Manser P, Bühlmann R, Fix M K, Vetterli D, Mini R, and Rügsegger P 2001 Calculations and measurements of portal dose images in IMRT *Med. Phys.* **28** 1267 (Abstract)

- Manser P, Fix M K, Figini S, Barengo R, Born E J, Mini R, and Rügsegger P 2002a *Monte Carlo investigations on portal dose measurements with an a-Si:H EPID*, *Med. Phys.* **29** 1316 (Abstract)
- Manser P, Treier R, Riem H, Fix M K, Vetterli D, Mini R, and Rügsegger P 2002b Dose response of an a-Si:H EPID on static and dynamic photon beams *Med. Phys.* **29** 1269 (Abstract)
- Manser P, Fix M K, Born E J, Mini R, and Rügsegger P 2002c Dynamic MLC and its impact on EPID dosimetry using Monte Carlo *Radiotherapy and Oncology* **64**(S1)
- Manser P, Fix M K, Born E J, Vetterli D, Mini R, and Rügsegger P 2003a Dosimetric treatment verification of IMRT using an a-Si:H EPID and Monte Carlo simulations *Joint meeting of SASRO and SGSMP 2003* Geneva, Switzerland
- Manser P, Fix M K, Born E J, Vetterli D, and Mini R 2003b Treatment verification of IMRT by an a-Si:H EPID and Monte Carlo *World Congress on Medical Physics and Biomedical Engineering 2003* Sidney, Australia
- Mayer R, Williams A, Frankel T, Cong Y, Simons S, Yang N, and Timmermann R 1997 Two-dimensional film dosimetry application in heterogeneous materials exposed to megavoltage photon beams *Med. Phys.* **24** 455-460
- McCurdy B M and Pistorius S 2000 A two-step algorithm for predicting portal dose images in arbitrary detectors *Med. Phys.* **27** 2109-2116
- McCurdy B M C, Luchka K, and Pistorius S 2001 Dosimetric investigation and portal dose image prediction using an amorphous silicon electronic portal imaging device *Med. Phys.* **28** 911-924
- McNutt T R, Mackie T R, Reckwerdt P, Papanikolaou N, and Paliwal B R 1996 Calculation of portal dose using the convolution/superposition method *Med. Phys.* **23** 527-535
- McNutt T R, Mackie T R, and Paliwal B R 1997 Analysis and convergence of the iterative convolution/superposition dose reconstruction technique for multiple treatment beams and tomotherapy *Med. Phys.* **24** 1465-1476
- Mohan R and Chui C 1985 Energy and angular distributions of photons from medical linear accelerators *Med. Phys.* **12** 592-597
- Mohan R, Chui C, and Lidofsky L 1986 Differential pencil beam dose computation model for photons *Med. Phys.* **13** 63-73

- Mohan R 1997 Why Monte Carlo? *XII Int. Conf. on the Use of Computers in Radiation Therapy (Salt Lake City, Utah, May 1997)* pp 16-18
- Mohan R, Arnfield M, Tong S, Wu Q, and Siebers J 2000 The impact of fluctuations in intensity patterns on the number of monitor units and the quality and accuracy of intensity modulated radiotherapy *Med. Phys.* **27** 1226-1237
- Mosleh-Shirazi M A, Evans P M, Swindell W, Symonds-Taylor J R N, Webb S, and Partridge M 1998 Rapid portal imaging with a high-efficiency, large field-of-view detector *Med. Phys.* **25** 2333-2346
- Munro P 1995 Portal imaging technology: past, present, and future. *Semin. Radiat. Oncol.* **5** 115-133
- Munro P and Bouius D C 1998 X-ray quantum limited portal imaging using amorphous silicon flat-panel arrays *Med. Phys.* **25** 689-702
- Nutting C, Dearnaley D P, and Webb S 2000 Intensity modulated radiation therapy: a clinical review *Br. J. Radiol.* **73** 459-469
- Partridge M, Evans P M, Mosleh-Shirazi A, and Convery D 1998 Independent verification using portal imaging of intensity-modulated beam delivery by the dynamic MLC technique *Med. Phys.* **25** 1872-1879
- Partridge M, Symonds-Taylor J R N, and Evans P M 1999 A large-area ionization chamber for portal image calibration *Phys. Med. Biol.* **44** 271-279
- Partridge M, Evans P M, van Herk M, Ploeger L S, Budgell G J, and James H V 2000 Leaf position verification during dynamic beam delivery: A comparison of three applications using electronic portal imaging *Med. Phys.* **27** 1601-1609
- Partridge M, Ebert M, and Hesse B-M 2002 IMRT verification by three-dimensional dose reconstruction from portal beam measurements *Med. Phys.* **29** 1847-1858
- Pasma K L, Heijmen B J M, Kroonwijk M, and Visser A G 1998 Portal dose image (PDI) prediction for dosimetric treatment verification in radiotherapy. I. An algorithm for open beams *Med. Phys.* **25** 830-840
- Pasma K L, Dirkx M L P, Kroonwijk M, Visser A G, and Heijmen B J M 1999 Dosimetric verification of intensity modulated beams produced with dynamic multileaf collimation using an electronic portal imaging device *Med. Phys.* **26** 2373-2378
- Pasma K L 1999 Dosimetry with a fluoroscopic electronic portal imaging device *Thesis*, Rotterdam, The Netherlands

- Pasma K L, Vieira S C, and Heijmen B J M 2002 Portal dose image prediction for dosimetric treatment verification in radiotherapy. II. An algorithm for wedged beams *Med. Phys.* **29** 925-931
- Perez C A, Brady L W, and Roti J L 1998 Overview Principles and Practice of Radiation Oncology ed Perez C A and Brady L W (Philadelphia, PA: Lippincott-Raven) pp 1-78
- Radcliffe T, Barnea G, Wowk B, Rajapakshe R, and Shalev S 1993 Monte Carlo optimization of metal/phosphor screens at megavoltage energies *Med. Phys.* **20** 1161-1169
- Saleh B E A and Teich M C 1991 *Fundamentals of Photonics* (John Wiley & Sons, Inc., New York)
- Spirou S V and Chui C S 1994 Generation of arbitrary intensity profiles by dynamic jaws or multileaf collimators *Med. Phys.* **21** 1031-1041
- Stein J, Bortfeld T, Dörschel B, and Schlegel W 1994 Dynamic x-ray compensation for conformal radiotherapy by means of multi-leaf collimation *Radiother. Oncol.* **32** 163-173
- Stein J 1997 Investigations on intensity-modulated treatment techniques in conformal radiotherapy *Thesis*, Heidelberg, Germany
- Street R A (ed) 2000 *Technology and Applications of Amorphous Silicon* (*Springer Series in Materials Science*) vol 37 (Berlin: Springer)
- Van Dyk J, Barnett R B, Cygler J E, and Shragge P C 1993 Commissioning and quality assurance of treatment planning computers *Int. J. Radiat. Oncol. Biol. Phys.* **26** 261-273
- Van Dyk J 1999 Introduction *The Modern Technology of Radiation Oncology* ed J van Dyk (Madison, WI: Medical Physics Publishing) pp 1-17
- van Esch A, Vanstraelen B, Verstraete J, Kutcher G, and Huyskens D 2001 Pre-treatment dosimetric verification by means of a liquid-filled electronic portal imaging device during dynamic delivery of intensity modulated treatment fields *Radiother. Oncol.* **60** 181-190
- Vetterli D, Born E J, Cossmann P H, Mini R, and von Briel Ch 2002a Introduction of IMRT at the Inselspital in Bern *6th Annual SASRO Meeting*, Zurich, Switzerland

- Vetterli D, Riem H, Manser P, Born E J, Mini R, and Rügsegger P 2002b Gated portal imaging: a new acquisition mode for PortalVision aS500 *Radiotherapy and Oncology* **64**(S1)
- Vieira S C, Dirkx M L P, Pasma K L, and Heijmen B J M 2002 Fast and accurate leaf verification for dynamic multileaf collimation using an electronic portal imaging device *Med. Phys.* **29** 2034-2040
- Walters B R B and Rogers D W O 2002 DOSXYZnrc Users Manual, NRCC Report PIRS-794
- Wang X, Mohan R, Jackson A, Leibel S, Fuks Z, Ling C C 1996a Optimization of intensity modulated 3D conformal treatment plans based on biological indices *Radiother. Oncol.* **37** 140-152
- Wang X, Spirou S, LoSasso T, Stein J, Chui C S, and Mohan R 1996b Dosimetric verification of intensity-modulated fields *Med. Phys.* **23** 317-327
- Webb S 1993 *The Physics of Three-Dimensional Radiation Therapy* (Bristol: Institute of Physics Publishing)
- Webb S 1997 *The Physics of Conformal Radiotherapy – Advances in Technology* (Bristol: Institute of Physics Publishing)
- Wong J W, Slessinger E D, Hermes R E, Offutt C J, Roy T, and Vannier M W 1990 Portal dose images I: Quantitative treatment plan verification, *Int. J. Radiat. Oncol. Biol. Phys.* **18** 1455-1463
- Xia P, Chuang C F, and Verhey L J 2002 Communication and sampling rate limitations in IMRT delivery with a dynamic multileaf collimator system *Med. Phys.* **29** 412-423
- Yaffe M J and Rowlands J A 1997 X-ray detectors for digital radiography *Phys. Med. Biol.* **42** 1-39
- Zelefsky M J, Fuks Z, Hunt M, Yamada Y, Marion C, Ling C C, Amols H, Venkatraman E S, and Leibel S A 2002 High-dose intensity modulated radiation therapy for prostate cancer: early toxicity and biochemical outcome in 772 patients *Int. J. Rad. Oncol. Biol. Phys.* **53** 1111-1116

Acknowledgements

This work would not have been done without the help of many people.

First, I would like to thank Prof. Dr. Peter Rügsegger for luring me to the field of Medical Physics and for his interest in my Ph.D. project. Furthermore, I am grateful to Prof. Dr. Peter Niederer for supervising this project and for his serious support and advice of my work. Many thanks go to Dr. Roberto Mini for his support and giving me the opportunity to do collaborative work with the Inselspital Berne.

Special thanks go to Dr. Michael Fix for his tremendous support, stimulating discussions and unlimited advice. Michael encouraged me for this Ph.D. project and taught me how to perform Monte Carlo simulations. Also, many thanks to Dr. Daniel Vetterli from the Inselspital Berne for his continuous support and all the exciting discussions we had on various topics in Medical Physics.

Heinrich Riem of Varian Medical Systems deserves my sincere gratitude for his kind help regarding all my questions about the PortalVisionTM aS500. I am indebted to Martin Kamber for expert advice and for having access to a ‘research detector’. Many thanks go to Patrick Sommer and Dr. Wolfgang Kaissl for generous support and their interest.

I want to thank my former students for their scientific support as well as for all the inspiring debates we had. Thus, many thanks to: Raphael Barengo, who built the fundamental concepts for Monte Carlo simulations of the a-Si:H EPID; Rolf Bühlmann for supportive investigations on calculations and measurements of portal dose images; Simon Figini, who refined the Monte Carlo simulations and provided a number of helpful tools; Reto Treier for numerous measurements and evaluations of dynamically applied fields.

I wish to express my gratitude to all the colleagues from the Inselspital in Berne, especially to Dr. Ernst Born for his encouraging suggestions.

Many thanks go to Stefanie Oestreicher for perfect administrative work with the VMS cluster and Marco Stampanoni for interesting discussions about physical matters. Also, many thanks to Walter Pistoia for being a motivating co-worker. I would like to thank the following persons for helping me in different ways: Dr. Adrian Kohlbrenner, Dr. Harald Keller, Bruno Willi, Dr. Bruno Koller, Dr. Andres Laib, Dr. Stefan Hämmerle, Emmi Rügsegger, Paul Lüthi.

And last but not least, I would like to thank my wife Eveline for magnificent support during the last years.

Curriculum Vitae

Peter Manser

Born September 28, 1971

Citizen of Appenzell, Switzerland

- 1978-1983 Primary School in Merenschwand, Switzerland
- 1983-1988 Secondary School in Muri, Switzerland
- 1988-1992 High School (Matura Type C) in Wohlen, Switzerland
- 1992-1998 Physics studies at Swiss Federal Institute of Technology ETH Zurich, Switzerland with graduation *with honor* in Experimental Physics as Dipl. Phys. ETH
- 1998-2000 Post-graduate studies in Medical Physics at Swiss Federal Institute of Technology ETH Zurich, Switzerland with graduation as Dipl. NDS ETHZ in Medical Physics
- 1998-2003 Ph.D. student and scientific researcher at the Institute for Biomedical Engineering, Swiss Federal Institute of Technology ETH and University of Zurich, Switzerland